

POLITECNICO DI TORINO

Dipartimento di Ingegneria Strutturale, Edile e Geotecnica

Corso di Laurea Magistrale in Ingegneria Civile

a.a. 2018/2019

TESI DI LAUREA MAGISTRALE

ACCOUNTING FOR SOIL-STRUCTURE INTERACTION IN THE
CALIBRATION OF MONITORED BUILDINGS



APRILE 2019

Relatore:
Dott. Ing. Rosario Ceravolo
Co-relatore
Ing. Gaetano Miraglia

Candidato:
Luca Parodi

Summary

Index of Figures	5
Index of Table	7
1. Introduction.....	9
2. Site characterization.....	12
2.1. Geographic framework.....	12
2.2. Geological framework	14
2.3. Tectonic Elements	15
2.4. Historical seismicity and today's seismicity.....	17
2.5. Response Spectra	21
2.6. Seismic base Hazard of Visso.....	22
2.7. Reference Legislation	23
3. Characterization of the structure	25
3.1. Vertical structures	26
3.1.1. Types of Masonry	26
3.1.2. Wall Bands.....	26
3.2. Horizontal and Cover.....	27
3.2.1. Intermediate slab	27
3.2.2. Cover	28
3.3. Connections.....	28
3.4. Monitoring systems.....	29
4. Damage reported on the structure	32
4.1. Damage reported at 24-08-2016.....	32
4.2. Damage reported at 26-10-2016.....	33
5. Nonlinear identification.....	39
5.1. State of the art	39
5.1.1. Masing model.....	40
5.1.2. Ramberg-Osgood-Masing model.....	41
5.1.3. Ishihara	41
5.1.4. Models used	42
5.2. Acquisition of experimental data	42
5.2.1. Notes on seismic refraction.....	43
5.2.2. Notes on the MASW tests	43
5.2.3. Notes on Down-Hole tests	44

5.2.4. Notes on passive tests.....	45
5.2.5. HVSR Method	45
5.2.6. Case study.....	46
5.3. Dealing with soil structure-interaction.....	49
5.4. Ground motion deconvolution.....	49
5.4.1. Fundamental features	49
5.4.2. Mechanical soil Behavior.....	51
5.4.3. Equivalent linear Method.....	52
5.4.4. Time series Method.....	56
5.5. Formulations	57
5.5.1. Nonlinear Identification with Time-Frequency distribution	57
5.5.2. Modified Davidenkov	60
5.5.3. Numerical model validation	63
5.5.4. The 3 DoFs black-box model	66
5.6. Final model	75
6. Application.....	76
6.1. Calibration of the soil-mass.....	76
6.1.1. Sensitivity analysis.....	76
6.1.2. Geometry of the model.....	79
6.1.3. Results after calibration	82
6.1.4. Depth validation in third layer correspondence	85
6.2. Ground motion deconvolution.....	87
6.2.1. “General setting”	87
6.2.2. Soil types	88
6.2.3. Soil discretization	92
6.2.4. Results after deconvolution	94
6.2.4. Data filtering.....	94
6.3. Resolution of equations	95
6.3.1. Determination of masses refers to 2-nd and 3-rd Degree of Freedom	95
6.3.2. Parameter determination, model updating.....	98
6.3.3. Postprocessing.....	104
7. Conclusion	114
8. Attachments	116
8.1. Non-linear identification	116

8.2. Optimization with TFD.....	124
9. Bibliography.....	126

Index of Figures

Figure 2.1: Administrative Limits of the Commune of Visso [14]	13
Figure 2.2: 3D Restitution of the geological and geomorphological structure of the area [14].....	13
Figure 2.3: Main tectonic structures affecting the territory [14].....	16
Figure 2.4: Historical Seismicity of the Commune of Visso [14].....	18
Figure 2.5: Today's Seismicity of the events of August-October 2016 [14].	18
Figure 2.6: Map of earthquake shaking of October 30, 2016 with M_w of 6.5 [14].....	19
Figure 2.7: Seismic Sequence in central Italy at October 26, 2016 [14].....	20
Figure 2.8: Seismic Sequence in central Italy at October 30, 2016 [14].....	20
Figure 2.9: Number of events per day with any magnitude [14].	21
Figure 2.10: Comparison of regulatory spectra of NTC 08 to SLV and SLV with recorded spectra.....	22
Figure 2.11: Seismic hazard Map with parameter a_g with 10% in 50 years [14].....	23
Figure 3.1: Plan of the raised floor of the school "Pietro Capuzi" in Visso [15].	25
Figure 3.2: Architrave of the raised floor [15].	27
Figure 3.3: Minor sub-horizontal lesions to the interface with the internal masonry on the first floor [15].	29
Figure 3.4: Sensor arrangement inside the structure.	30
Figure 3.5: Accelerogram recorded by channel 21 in x direction.	31
Figure 3.6: Accelerogram recorded by channel 21 in y direction.	31
Figure 3.7: Accelerogram recorded by Channel 21 in z direction.	31
Figure 4.1: State of damage within the structure following the event of 24 August [16].	32
Figure 4.2: State of damage outside the structure following the event of 24 August [16].	33
Figure 4.3: Damage Status on external prospects [16].	34
Figure 4.4: Legend of the damage [16].	35
Figure 4.5: The damage related to the ground floor plan [16].	35
Figure 4.6: Shear injuries for diagonal cracking in the males of the body A oriented Y-direction [16].	36
Figure 4.7: Shear-sliding Lesions in the Northwest wing at the cantonal male [16].....	36
Figure 4.8: Internal vision with severe pseudo-vertical lesions in the North-west wing [16].....	37
Figure 4.9: Picture of the damage reported to the plan on the first floor [16].	37
Figure 4.10: Expulsion of the North cantonal body B [16].	38
Figure 4.11: Extended Collapse of the attic floor [16].	38
Figure 5.1: Secant shear modulus G_{sec} and tangentshear modulus G_{tan} in a hysteresis loop [19]; (b) Variation of the secant shear modulus with the number increase (1, 2, 3..n) of cyclic loading in an equivalent linear model [19].	39
Figure 5.2: Hyperbolic nonlinear soil model with extended Masing model to define loading and unloading behavior [19].	40
Figure 5.3: Backbone curve and associated hysteretic curve [20].	41
Figure 5.4: Plain view of the school and location of the surveys [17].	46
Figure 5.5: Soil profile and V_s profiles measured through DH and MASW technique [17].	47

Figure 5.6: Estimation of fundamental soil frequency by HVSR method [17].	48
Figure 5.7: (a) Definition of the secant module of the initial tangent module (small deformation Module G_0) (b) Definition of the decay curve of the shear module [23].	51
Figure 5.8: Dependence of the decay curves of the shear module and of the damping ratio from the plasticity index [23].	52
Figure 5.9: Explanation of the equivalent linear method [28].	53
Figure 5.10: Modified Davidenkov model with hardening behavior ($B < 0$) [33].	62
Figure 5.11: Modified Davidenkov model with softening behavior ($B > 0$) [33].	63
Figure 5.12: Results parameters of the numerical model [33].	65
Figure 5.13: The final Model used in the analysis.	75
Figure 6.1: Sensitivity analysis: variation of the first frequency with the parameters.	78
Figure 6.2: Sensitivity analysis: percentage of the total variability of the first natural frequency carried by each model parameter.	78
Figure 6.3: Plan geometry of the soil.	80
Figure 6.4: Solid model for soil calibration.	81
Figure 6.5: FE model of the soil.	82
Figure 6.6: First modal shape after calibration of the soil-mass.	84
Figure 6.7: Second modal shape after calibration of the soil-mass.	84
Figure 6.8: Third modal shape after calibration of the soil-mass.	85
Figure 6.9: a) interlayer contrast of impedance; b) bedrock contrast of impedance	86
Figure 6.10: Trend of G/G_{max} and D to varying deformative level for Vucetic & Dobry formulation.	89
Figure 6.11: Trend of G/G_{max} and D to varying deformative level for Seed & Idriss formulation.	90
Figure 6.12: Trend of G/G_{max} and D to varying deformative level for Rollins formulation.	91
Figure 6.13: Seismic input for the building or output for the soil-structure system at chanel 21 (a), seismic input for the soil structure system (b).	94
Figure 6.14: Modeling a "Shell" element within the FE software.	96
Figure 6.15: Modeling of a "Combin" element within the FE software.	96
Figure 6.16: Modelling of the building using FEM software.	97
Figure 6.17: a) Building front; b) Ddisposition of the masses.	98
Figure 6.18: Trend of numerical and experimental Restoring force for first DoF.	101
Figure 6.19: Trend of numerical and experimental Restoring force for second DoF.	102
Figure 6.20: Trend of numerical and experimental Restoring force for first DoF.	102
Figure 6.21: Variation of Force on time about 1 st DoF.	103
Figure 6.22: Variation of Force on time about 2 nd DoF.	104
Figure 6.23: Variation of Force on time about 3 rd DoF.	104
Figure 6.24: Variation of Frequency on time.	105
Figure 6.25: Variation of Stiffness on time.	106
Figure 6.26: Identified modal quantity, pre- and post- main shock: percentage of participation mass.	107
Figure 6.27: Identified modal quantity, pre- and post- main shock: percentage of participation mass.	108
Figure 6.28: Identified modal shape, pre- and post- main shock: 1 st mode.	108
Figure 6.29: Identified modal shape, pre- and post- main shock: 2 nd mode.	109
Figure 6.30: Identified modal shape, pre- and post- main shock: 3 rd mode.	110
Figure 6.31: Proposed Soil-Structure Interaction index, pre- and post- shock: $SSII_h$.	111

Figure 6.32: Proposed Soil-Structure Interaction index, pre- and post- shock: SSII. 112

Index of Table

Table 5.1: Experimental soil parameters [17].	48
Table 5.2: Updated parameters of the numerical model [33].	65
Table 5.3: Time dependent parameters ${}^3n_n(t)$ and non Time dependent (3d_n) for 3 rd DoF.	69
Table 5.4: Parametri che dipendono dal tempo ${}^2n_n(t)$ e quelli non (2d_n) per il secondo DoF.	71
Table 5.5: Time-dependent parameters ${}^1n_n(t)$ and non 1d_n for the first DoF.	74
Table 6.1: Initial coordinates of plan geometry before sensitivity analysis.	76
Table 6.2: Coordinates of the geometry in the plant with which the sensitivity analysis was carried out.	77
Table 6.3: Mechanical and geometric parameters that are introduced in FE model.	82
Table 6.4: Initial and updated value of Z, f_1 , f_2 and f_3 .	83
Table 6.5: Values of impedance contrast in relation to each layer and bedrock.	86
Table 6.6: Discretization of stratigraphic model.	93
Table 6.7: Mass of the system, values in [Kg].	97
Table 6.8: Update parameters for the third DoF: $K_{0,jr}$ e D_{jr} .	99
Table 6.9: Update parameters for the second DoF: $K_{0,jr}$ e D_{jr} .	99
Table 6.10: Update parameters for the first DoF: $K_{0,jr}$ e D_{jr} .	99
Table 6.11: Update non linear parameters for the third DoF: B_j , C_j , N_j .	100
Table 6.12: Update non linear parameters for the second DoF: B_j , C_j , N_j .	100
Table 6.13: Update parameters for the first DoF: B_j , C_j , N_j , E_1 .	100

Abstract

This thesis reports a first study for the nonlinear identification of a monitored masonry building (School Pietro Capuzzi located in Visso, province of Macerata), considering the soil-structure interaction phenomena. A short geographical and geological introduction is reported in order to understand which were the factors that influenced the seismic motion, with brief hints on the ancient and modern seismicity of the area.

In order to decipher the damage suffered by the structure following the seismic events that have affected central Italy in 2016, will be described the structure in its various components and it will bring back the state of damage.

All the formulations and methods used for the interaction analysis will be described. In order to estimate the evolution of the model parameters in time, a *Time-Frequency Distribution* computed with *Short Fourier Transform* of the signals is used for the identification. The fundamental frequency of the ground is available by seismic test at single station HVSR in free field conditions, with which it was possible to reconstruct the stratigraphic profile of the ground until reaching the bedrock at 40 m. Then, the instantaneous frequencies of a plane soil-structure system are identified.

For the dynamic behavior, two types of mechanical laws are mixed to produce a black-box model of the system: a rate-independent Bouc-Wen type oscillator for the building and a modified, rate-dependent, Davidenkov type oscillator for the soil. For the process of deconvolution and the search for the seismic input signal, models by literature have been adopted for the stratigraphy. Finite element (FE) models are used to estimate the masses of the structure and for calibration of the mass of the soil.

Keywords: Soil-structure interaction, Time-Frequency Distribution, Nonlinear analysis, Masonry building, Central Italy earthquake.

1. Introduction

Being the Italian peninsula subject to numerous seismic events, the study inherent in seismic hazard is of paramount importance for the safeguarding of people and structures.

However, in spite of the seismic design and the research are in continuous development, because of the antiquity of the majority of the real estate present on the Italian soil (Most buildings falls in a time period in which the knowledge of structures, materials and actions was very limited and Simultaneously Supported by Regulatory bases that are not sufficiently adequate both from a technical and institutional point of view), the phenomena of medium-high intensity are often destructive and catastrophic.

The demand for greater prevention and prediction, coupled with a growing scientific evolution, allowed to design structures able to meet the required limit states: through the transposition at regulatory level of appropriate technical specifications and through the coordination between policies and the various bodies prepared (*Protezione Civile* and entities like the *Osservatorio Sismico delle Strutture*) has come to a level of adequate knowledge.

In this direction, the monitoring systems are a fundamental tool able to evaluate, even in real time, the forces that act on the structure and the consequent displacements. The OSS allows, in fact, to evaluate the damage caused by an earthquake on a monitored structure, allowing an extension of the evaluation to similar structures that fall within the same affected area. This is extremely important for the design and planning of new works, as well as for the management of emergencies through the sharing of original data. They also allow to modify, where possible, the behaviour of particular components.

The structure object of study of the thesis is the School "*Peter Capuzi*" Located in Visso, province of Macerata, being located in an area known as seismic risk as Central Italy, is subject to monitoring by the "*Department of Civil Protection*", thanks to which it was possible to obtain valuable information for the study, in this particular case, of the ground-structure interaction, though, however, monitoring systems are typically not designed for considering soil-structure interaction.

In the second chapter we will introduce the geographical and geological conformation in which the structure is located, which is strongly conditioned by the orography, with reliefs also of high height, and by the hydrography, with the presence of numerous waterways; Precisely the presence of these courses, with particular reference to the Nera River and its tributaries, has operated a strong erosive action, determining a particular mountainous conformation characterised by deep valleys and steep flanks.

Even The geological structure is decisive for the understanding of the variation of the seismic motion, this is especially true in the presence of hedging soils mainly made up of materials with fine granulometry of anthropic origin, and a geological substrate consisting predominantly of marl and clays.

It Is therefore possible to affirm that the interaction between topographical and hydrographical composition and geological structure is symptomatic of a territory subject to tectonic evolution still underway. In this regard, theA geotechnical characterization is a key

element for the study of the local seismic response and for the risk assessment associated with earthquake-induced instability phenomena. The study of the seismic response is nowadays required in recent national and international regulations for the evaluation of the seismic response reference to be used for the design and verification of geotechnical and structural systems.

Site response is known to play an important role in modifying the amplitude, frequency, and duration of earthquake shaking. For nonliquefiable sites, studies showed that site response frequently amplifies the low-frequency components of weak-to-medium intensity motions and introduces complex patterns of amplification and deamplification for higher intensity motions associated with extensive soil yielding.

In the course of the third chapter, however, the structure will be described in its various parts, then the analysis will proceed with the study of the damage following the seismic events that occurred in August and October 2016 respectively.

In particular, the phenomenon of soil-structure interaction has been studied, thanks to which it has been possible to identify an estimate of the mass that participated actively with the structure during the seismic event of 26 October 2016. To do this, in the paper a reduced 2 Degree of Freedoms (DoFs) model of a masonry building is analyzed to assess the dynamic behavior of the structure in presence of soil-structure interaction. This is accounted for by including in the reduced model an additional DoF, representing the portion of the building below the raised ground floor of the structure. The resulting system is a 3 DoFs black-box model composed by both Bouc-Wen type [1], [2], [3], and modified, rate-dependent, Davidenkov type [4], oscillators; during the course of the treatment will be explained for what reasons Davidenkov's formulation has been modified. It will also explain the equivalent spring-mass schematization that has been used for the constituent models used.

To understand the behaviour of structures considering the soil-structure interaction (SSI), it is desirable to investigate the behaviour of single-degree-of-freedom (SDOF) system which in turn can be used to approximately represent multi-degree-of-freedom systems.

The scope is to estimate the modal quantities of the reduced system in presence of soil-structure interaction during earthquakes. To estimate the modal quantities, a nonlinear identification of the model parameters is pursued following a quasi-direct approach. The identification methods for non-linear systems are usually classified in two families: (i) parametric, [5], [6], [7], and (ii) non-parametric methods, [8], [9], [10]. Another important classification of the identification methods for nonlinear systems is based on the domain in which the identification is performed: frequency, time, or joint time-frequency domain, e.g. [11], [12]. Using a joint time-frequency domain can be also useful to perform instantaneous estimates of the parameters value, whose stability over time is symptom of consistency of a given model, [13]. In this relations, a time-frequency method is considered for the nonlinear identification of the system.

In Section 5, the joint time-frequency domain method is discussed and the basic theory for the assumed nonlinear models is briefly described. Always in this section, the proposed law, used to model the soil/raised ground floor dynamics (i.e. the modified Davidenkov model), is

validated numerically with a 1 DoF system subjected to a synthetic earthquake of Loma Prieta and fictitious damage. Following the calibration of the mass of the soil, determined by the FE modelling of the subsoil being aware of the fundamental frequency of the ground, the soil-structure interaction problem is analyzed for the masonry building. It was also necessary to carry out a sensitivity analysis, in order to study the variability of the various parameters, both geometric and mechanical, of the soil at the variation of the first numerical frequency. So, in Section 6, the nonlinear identification is applied to the School of Visso and then, in order to achieve the evolution of the time of the restoring force, the stiffness and the frequencies, a self-analysis was carried out. It was thus possible to analyse how the numerical values fit with those of experimental nature, validating in this way the reliability of the models constituted used and the assumptions adopted. You will evaluate, specifically, both in the case pre-and for the post case, the frequency variation and the participant mass contribution for three structure vibration modes. As a final result, the SSII factor will be identified, always for the pre-and post-case, identification of the real interaction between the building and the mass of soil.

2. Site characterization

2.1. Geographic framework

The Commune of Visso is located in the province of Macerata (Region Marche), and it is an area entirely Mountainous with reliefs that exceed 1,000 m (M. Fema 1.575 m s.l.m.; M. Careschio 1.366m s.l.m.); the area lies on the western side of Monti Sibillini, in the southern sector of the Umbrian-Marche Apennines.

Due to the vast presence of rivers, the reliefs are deeply engraved, determining a considerably indented territory conformation: in particular the R. Fema and its tributaries which, by draining towards the F. Tevere, determine the inclusion of great part of the municipal territory. The northernmost part of the territory of the commune of Visso, bounded from Tirreno – Adriatic watershed, falls instead in the basin of the R. Chienti, directed instead towards the Adriatic Sea [14].

This conformation It is symptomatic of a territory subject to tectonic evolution, still underway, in which morphogenetic actions fail to compensate for its dynamism.

The Black F. With its tributaries has operated a strong erosive action, so the valleys are very deep and with steep sides. The acclivity of the slopes favours So The onset of gravitational phenomena sometimes very extensive, both ancient and quiescent, more rarely active (Western slope of M. Fema, which is associated with a deep gravitational deformation of the slope); In the situations of subvertical rocky walls (Valnerina Gorges, Valleys of the T. Ussita and F. Nera near Visso) can be In addition Phenomena of collapse and tipping in rock which, in higher risk situations, have been mitigated with Protection and Consolidation works [14].

In the following Figure 0.1 The geographical framework of the Commune of Visso and its administrative limits is reported: it can be seen that the municipal territory borders southwards and towards the west with Umbria, while in red circles there are the areas that have been the subject of a Seismic microzonation of level III following the seismic events occurring in 2016.

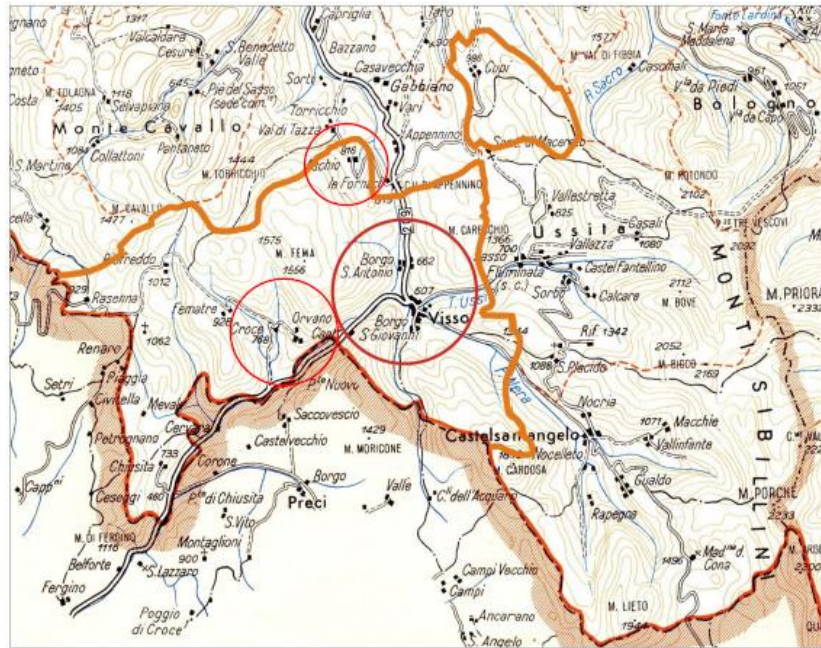


Figure 0.1: Administrative Limits of the Commune of Visso [14].

In Figure 0.2 Instead, there is a 3D Restitution of the geomorphological structure of the Visso area, which shows the position of the commune, developed on the bottom of the river Nera and its tributaries, on alluvial deposits that can reach considerable thicknesses [14]. The slopes at the edge of the valleys are characterised both by deposits of alluvial origin, with fine granulometry, and by detritic deposits with predominantly coarse granulometry.

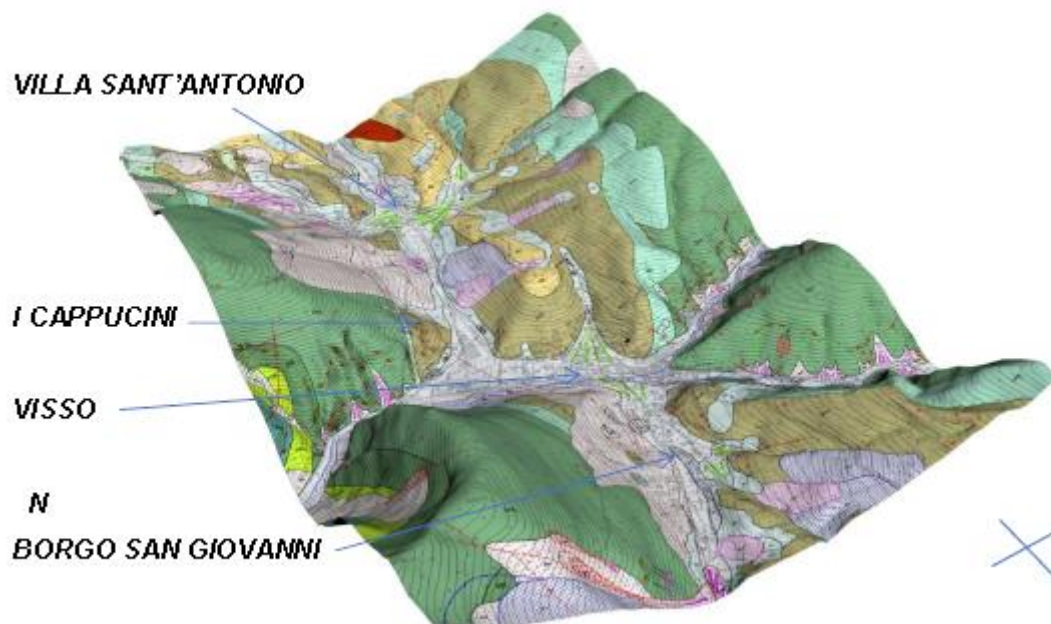


Figure 0.2: 3D Restitution of the geological and geomorphological structure of the area [14].

Due to the orographic and hydrographical conformation, in case of strong dynamic stresses, the criticalities are represented by **Amplification effects** seismic stratigraphic in the areas of valley floor e from earthquake induced landslides, mostly falling boulders in the valleys with the steepest slopes that can interfere with the inhabited centre or with road infrastructures [14].

Due to the summation of all these factors that cause an amplification of the seismic motion, with the consequent burden of the actions affecting the structures, ad following the earthquakes occurring in particular on 26 and 30 October 2016, Visso was severely damaged in many buildings present, with numerous collapses that have involved many strategic buildings and that interrupted the economic activities of many local businesses.

2.2. Geological framework

The municipal territory falls in the southern Umbrian-marches Apennines, whose conformation consists of a chain with folds and overflows with axial directions from N-S to NNO-SSE, formed by several active structures responsible for the seismic motion of the area [14]. Moreover, it is possible to make some small hints on the stratigraphy of the area, placing the accent on the **covering soils** which, although they are less extensive than the **geological substrate** (portions of rock that remains unchanged), are the most important parts regarding the local seismic response and interaction with buildings: in fact, on such hedging grounds, it insists most of the built of Visso town hall and other neighboring hamlet.

It is possible to provide a diagram on the typologies of covering soils constituting the territory, with reference to the relative characteristics:

- Anthropic Deposit: Material constituted mostly from land of excavations or material of construction scrap, whereby dissolved or moderately thickened with variable granulometry;
- Active landslide Deposit: material placed in place by landslides with a hint of evolution, in rock (with possible tipping) or debris (with the possibility of casting);
- Quiescent landslide Deposit: heterometric material of franous origin without clues of evolution;
- Inactive landslide Depot: heterometric materials put in place for landslides triggered and evolved in morphodynamic conditions different from the present ones, in rock;
- Groundwater Debris: gravitative slope material with a predominantly coarse variable particle size characterised by high permeability;
- Alluvial Deposits: of present origin following the recent river dynamics and morphological conformation; Variable granulometry and different permeability according to the presence of Sandy gravels and gravels, Sands and Limose Sands, Limited and Clayey Limited;

As far as the geological substrate is concerned [14], it was possible to divide it into:

- Marne with Cerroigna;

- Bisciario: alternating layers of calcareous-siltosis with marly layers of thickness between 15-20 cm; presence of black flint with layers of about 10 cm of thickness;
- Scaglia Cinerea: clayey marl and marl with limestone presence;
- Scaglia Variegata: alternating marly limestone layers with clayey marne and marl;
- Scaglia Rossa e Bianca: presence of limestones alternated with very thin pelvic interlayers. Presence of flint layers with limestone intercalations also of considerable thickness.
- Maiolica: layers of limestone with flint and clay.

Summarizing, these soils are mostly constituted by deposits of active, quiescent and inactive landslide of chaotic and heterometric nature, and debris of groundwater of gravitative origin with predominantly coarse granulometry.

The main constituents of the soil of roofing and of the geological substrate have thus been introduced, which will play an important role especially for the variation that will undergo the seismic signal to the passage in the deposit of soil.

2.3. Tectonic Elements

From the tectonic point of view, the area of interest is crossed by important structures both plicative (consisting of inverse faults and overflows) and calming (consisting of direct faults). It is therefore important to analyze the seismogenic potential of the area, so that the behaviour and the dynamics of the soil can be predicted: in this regard it is reported in the following Figure 0.3 the dislocation of the plicative structures, displaced by successive faults predominantly direct, and distensive [14]. Specifically, in red and orange are indicated the compressive structures and represent:

1. overslip of M. Cavallo;
2. sinclinal of Rioffredo;
3. anticlinal of M. Fema;
4. overslip of M. Fema;
5. sinclinale of Visso;

Always in the picture, the distensive faults with prevalent direct component are indicated in blue and include:

- Fault M. Pennino-M. Tolagna (Colfiorito system activated in 1997);
- Fault Norcia-Preci (System activated in 1979);
- Fault M. Vettore-M. Bove activated during the sequence of the 2016-2017 and currently accoured.

Visso, in particular, is located east of the overflow of M. Fema, in the Synclines di Visso – Camerino.

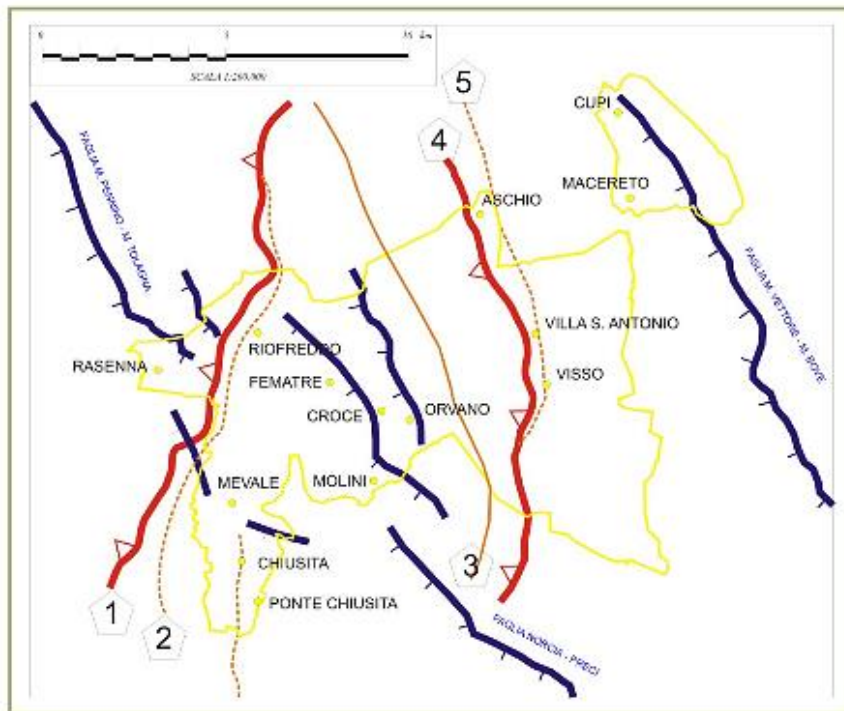


Figure 0.3: Main tectonic structures affecting the territory [14].

The connection between the M. Pennino – M. Tolagna system and the Norcia system – Preci, both seismically active, is carried out through a series of directly embryonic, coaxial (apennine direction) faults, such as the fault that dislocates the western slope of M. Fema.

In this area, where the potential for activating direct faults is very high, the majority of the fractions of the Commune of Visso are located, including Groce and Orvano [14].

The areas are located from a geological point of view within a synclinal whose nucleus surfacing marly terms of Scaglia Cinerea, Bisciario, Marne with Cerrogna; to the west, the Synclinal joins, through the overflow of M. Fema (*Blindthrust*) to the anticlinal M. Fema; bent reversed layers of the red scaglia of the western flank of the synclinal emerge in spectacular subvertical walls at the entrance of the Valnerina gorges; the plicative deformation becomes pervasive proceeding to the terms of the Variegated Scaglia And Scaglia Cinerea, affected by shear areas that hide the original stratification (road for The Capuchin, Convent of the Capuchin).

As a testimony to this, the two strong earthquakes that occurred on 26 October 2016 are referable to movements of the system of direct faults which, by immersing westward, affect the underground of Visso to the critical depths in which the major events develop in this apennine sector, or between 8 and 12 km of depth, with a maximum distribution of the hypocenters around 10 km.

2.4. Historical seismicity and today's seismicity

In order to obtain appropriate instruments for seismic prevention and to equip the Municipalities with instruments to be used for planning and executive design in the areas most affected by the earthquake, a Level 3 microzonation study is necessary by defining the basic dangerousness and the reference events, which testify to the fact that the commune of Visso is characterised by a high seismicity since ancient times [14].

Going to extract from the INGV the earthquakes that have produced in the history ascertained damage, one can notice the frequency of the strong earthquakes affecting the commune. In particular, it is possible to highlight the high frequency of earthquakes with magnitude between 6-7 from the early years of 900, as shown in the following Figure 0.4.

In the following figure, I_s represents the local MCS intensity of the Municipality, mentre I_{max} is the maximum epicentral intensity.

Seismichistory of Visso				
[42.930, 13.088]				
Total number of earthquakes: 62				
Effects	Earthquake occurred:			
I_s	DATA	LOCALITA EPICENTRALE	I_{max}	Mw
6	1916 07 04 05:07	MONTI SIBILLINI	6-7	5.02 $\hat{A}\pm 0.22$
5	1916 11 16 06:35	REATINO	8	5.53 $\hat{A}\pm 0.22$
NF	1919 06 29 15:06:12	Mugello	10	6.29 $\hat{A}\pm 0.09$
4-5	1922 06 08 07:47	CALDAROLA	6	4.89 $\hat{A}\pm 0.19$
2	1924 01 02 08:55:08	Medio Adriatico	7-8	5.36 $\hat{A}\pm 0.16$
5-6	1927 08 16 00:53	CASTEL SANT'ANGELO	6	4.56 $\hat{A}\pm 0.27$
2-3	1930 07 23 00:08:43	Irpinia	10	6.62 $\hat{A}\pm 0.09$
4-5	1936 12 09 07:34	CALDAROLA	6-7	4.79 $\hat{A}\pm 0.22$
5	1950 09 05 04:08	GRAN SASSO	8	5.68 $\hat{A}\pm 0.07$
7	1951 09 01 06:56:04	SARNANO	7	5.34 $\hat{A}\pm 0.20$
3	1958 06 24 06:07:04	L'Aquila	7-8	5.21 $\hat{A}\pm 0.11$
4	1974 12 02 01:55:16	Valnerina	7-8	4.76 $\hat{A}\pm 0.17$
7	1979 09 19 21:35:37	Valnerina	8-9	5.86 $\hat{A}\pm 0.09$

4-5	1984 04 29 05:02:60	GUBBIO/VALFABBRICA	7	5.65 $\hat{A}\pm 0.09$
NF	1984 05 07 17:49:43	Appennino abruzzese	8	5.89 $\hat{A}\pm 0.09$
NF	1984 05 11 10:41:50	Appennino abruzzese		5.50 $\hat{A}\pm 0.09$
4-5	1986 10 13 05:10:01	Appennino umbro-marchigiano	5-6	4.65 $\hat{A}\pm 0.09$
3-4	1993 06 04 21:36:51	Nocera Umbra	5-6	4.50 $\hat{A}\pm 0.13$
3-4	1993 06 05 19:16:17	GUALDO TADINO	6	4.74 $\hat{A}\pm 0.09$
NF	1997 07 15 08:51	Appennino umbro-marchigiano	4-5	3.69 $\hat{A}\pm 0.21$
5	1997 09 03 22:07:30	Appennino umbro-marchigiano	5-6	4.56 $\hat{A}\pm 0.09$
3-4	1997 09 07 23:28:06	Appennino umbro-marchigiano	5-6	4.38 $\hat{A}\pm 0.15$
3	1997 09 09 16:54	Appennino umbro-marchigiano	5-6	4.07 $\hat{A}\pm 0.18$
3-4	1997 09 10 06:46:51	Appennino umbro-marchigiano	5	4.16 $\hat{A}\pm 0.18$
6-7	1997 09 26 00:33:13	Appennino umbro-marchigiano		5.70 $\hat{A}\pm 0.09$
6-7	1997 09 26 09:40:27	Appennino umbro-marchigiano	8-9	6.01 $\hat{A}\pm 0.09$
5-6	1997 10 03 08:55:22	Appennino umbro-marchigiano		5.25 $\hat{A}\pm 0.09$
6-7	1997 10 06 23:24:53	Appennino umbro-marchigiano		5.46 $\hat{A}\pm 0.09$
6-7	1997 10 14 15:23:11	Appennino umbro-marchigiano	7-8	5.65 $\hat{A}\pm 0.09$
4-5	1997 10 23 08:58:44	Appennino umbro-marchigiano		4.31 $\hat{A}\pm 0.25$
4-5	1997 11 09 19:07:33	Appennino umbro-marchigiano	5-6	4.90 $\hat{A}\pm 0.09$
5	1998 02 07 00:59:45	Appennino umbro-marchigiano	5-6	4.43 $\hat{A}\pm 0.09$
4-5	1998 02 16 13:45:45	Appennino umbro-marchigiano	5	4.03 $\hat{A}\pm 0.19$
5	1998 03 21 16:45:09	Appennino umbro-marchigiano	6	5.03 $\hat{A}\pm 0.09$
5	1998 03 26 16:26:17	Appennino umbro-marchigiano	6	5.29 $\hat{A}\pm 0.09$
4-5	1998 04 05 15:52:21	Appennino umbro-marchigiano	6	4.81 $\hat{A}\pm 0.09$

Figure 0.4: Historical Seismicity of the Commune of Visso [14].

As far as today's seismicity is concerned, the strong earthquakes that occurred in the sequence started on 24 August 2016 caused numerous collapses and lesions, producing also landslides and debris flows in the Valnerina gorges (valleys between Visso and Ussita and between Visso and Castelsantangelo sul Nera) and injuries to the ground.

Are reported in the following Figure 0.5 the values of the parameters recorded at the time of the seismic shocks that caused the most serious damage, referring to the events of 24-08, 26-10 and 30-10 2016 [14].

Tempo origine	Dist (Km)	PGA _x (g)	PGA _y (g)	PGA _z (g)	PSA _x (g)	PSA _y (g)
24/08/2016 01:36:32	28	0.3265	0.3172	0.1347	1.0521	0.8044
24/08/2016 01:56:00	39	0.0042	0.0049	0.0025	0.0109	0.0143
24/08/2016 02:33:29	16	0.0701	0.0686	0.0699	0.3469	0.4039
24/08/2016 02:59:35	16	0.0134	0.0122	0.0116	0.0473	0.0532
24/08/2016 03:08:10	39	0.0015	0.0022	0.0017	0.0066	0.0090
24/08/2016 03:40:11	37	0.0050	0.0061	0.0041	0.0179	0.0212
24/08/2016 04:06:50	18	0.0136	0.0120	0.0107	0.0467	0.0566
24/08/2016 11:50:30	13	0.0994	0.1018	0.0749	0.3186	0.3524
24/08/2016 17:46:09	32	0.0113	0.0118	0.0071	0.0386	0.0412
26/10/2016 17:10:36	7	0.2950	0.2145	0.4067	1.2613	0.7769
26/10/2016 19:16:57	8	0.3626	0.4751	0.3044	1.4019	1.3341
26/10/2016 19:18:05	4	0.3626	0.4751	0.3044	1.4019	1.3341
26/10/2016 21:42:01	9	0.0897	0.1039	0.0588	0.2260	0.2644
30/10/2016 06:40:17	10	0.2913	0.3012	0.3302	1.3862	1.4727

Figure 0.5: Today's Seismicity of the events of August-October 2016 [14].

In which *Dist* represents the epicentral distance from Common Visso, *Pga* the maximum acceleration at the base of the building, *Psa* the maximum acceleration on the structure. The strongest recent earthquake is that of October 30, 2016, with a magnitude of 6.5 and an estimate of intensity equal to the eighth or ninth degree of the MCS scale (Mercalli Cancani Sieberg). The following is reported in Figure 0.6 The shaking map following the events of 30, with an increasing intensity from yellow to red.

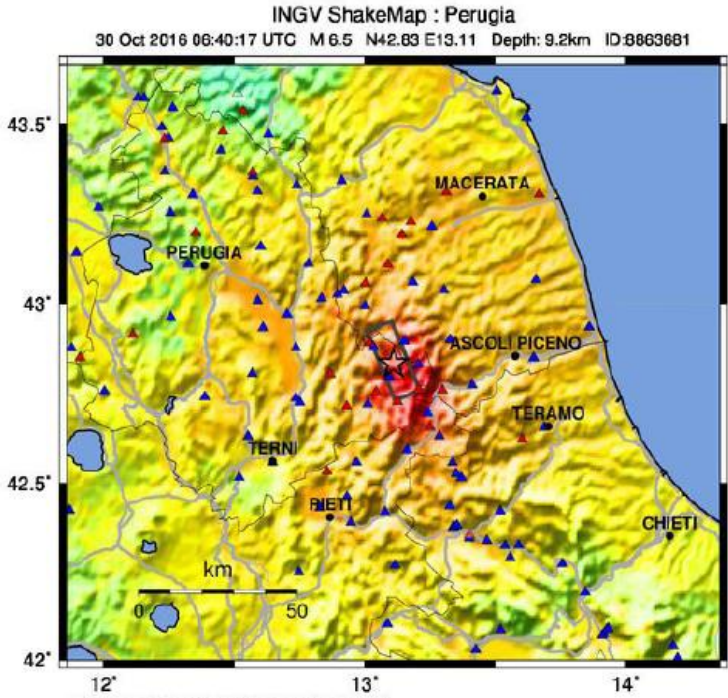


Figure 0.6: Map of earthquake shaking of October 30, 2016 with M_w of 6.5 [14].

This earthquake was preceded by two other events which occurred on 26 October having a magnitude of 5.4 and 5.9 with epicenters in the neighbouring areas of Visso (Valle del Tronto, Monti Sibillini, Monti della Laga and the Monti Dell'alto Aterno). The following Figure 0.7 and Figure 0.8 present the sequences for the events of 26 and the 30 October respectively [14].

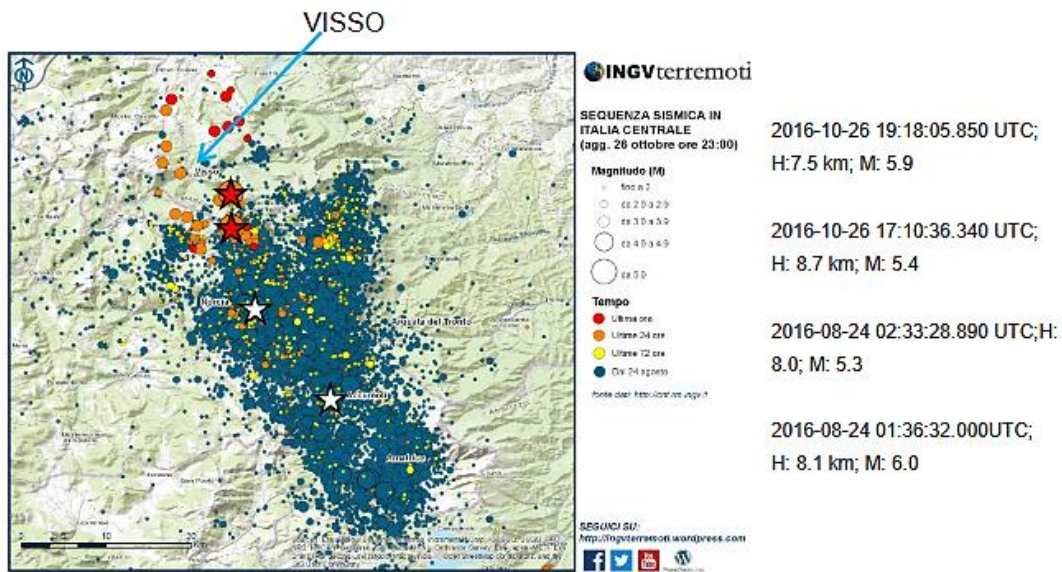


Figure 0.7: Seismic Sequence in central Italy at October 26, 2016 [14].

From the previous Figure 0.7 you can see how the epicenters of the earthquakes of October 26 (red stars in the box) are close to the comune of Visso, while in the Figure 0.8 is reported the seismic sequence, always with the epicenter mark with a red star, for the 30-10 event [14].

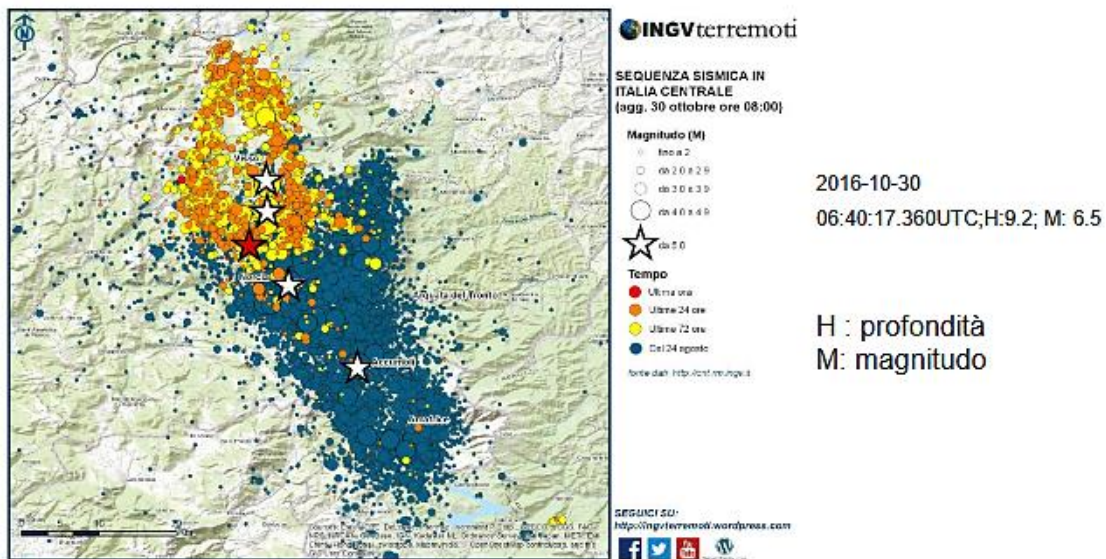


Figure 0.8: Seismic Sequence in central Italy at October 30, 2016 [14].

It is reported in the following Figure 0.9 the seismic swarm that affected the neighbouring areas of Visso from August 2016 until December 2017: in ordinate, the number of events with any magnitude is specified [14].

It shows how the data show a slow and progressive exhaustion of the swarm, with an average decrease in the number of events per day.

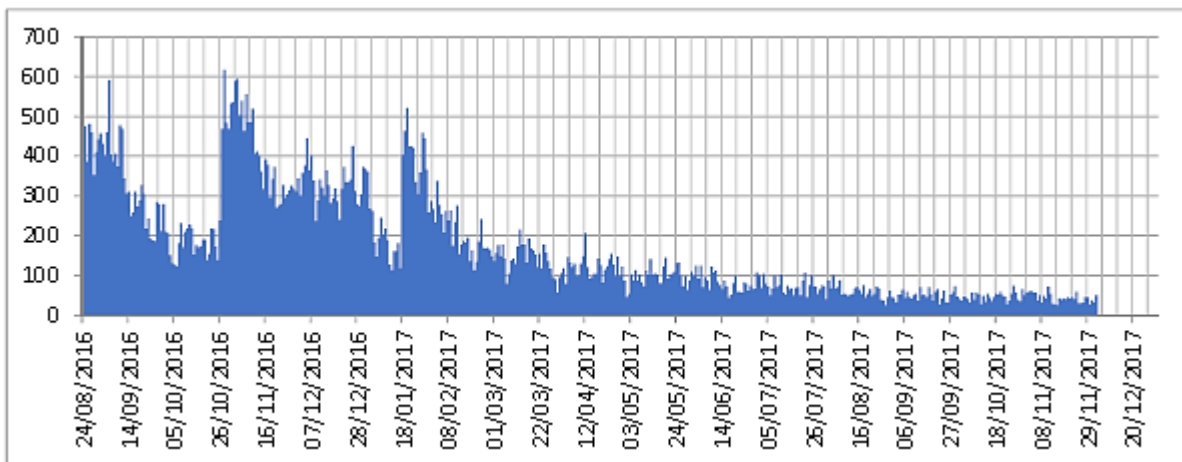


Figure 0.9: Number of events per day with any magnitude [14].

2.5. Response Spectra

In this paragraph we want to bring back the response spectra, for the most significant events, comparing them with those of legislation in such a way as to emphasize the intensity and severity of these phenomena. In particular, the structure has reported significant damage since the event of August 24 and, subsequently, that of 30 has contributed to the final demolition of the building. So, initially, in order to understand the evolution of the damage On the structure, have been reported in Figure 0.10 The reported response spectra at recordings of a station of the ITHACA network of Norcia (Accelerograms database of the Institute of Geophysics and Volcanology) in an area near the commune of Visso.

Specifically, the events considered refer to 24-08 that of the 01:36 hours, the 30-10 that of the 06:40 and the 26-10 the two events at 17:10 and 19:18.

However, The NTC Spectra 2008 of the regulations were obtained by means of the public Works calculation sheet following the insertion of the geographical coordinates of the site, of the nominal life (equal to 50 years) and of the Class of Use (classe IV, "costruzioni il cui uso preveda affollamenti significativi") and a damping of 5%.

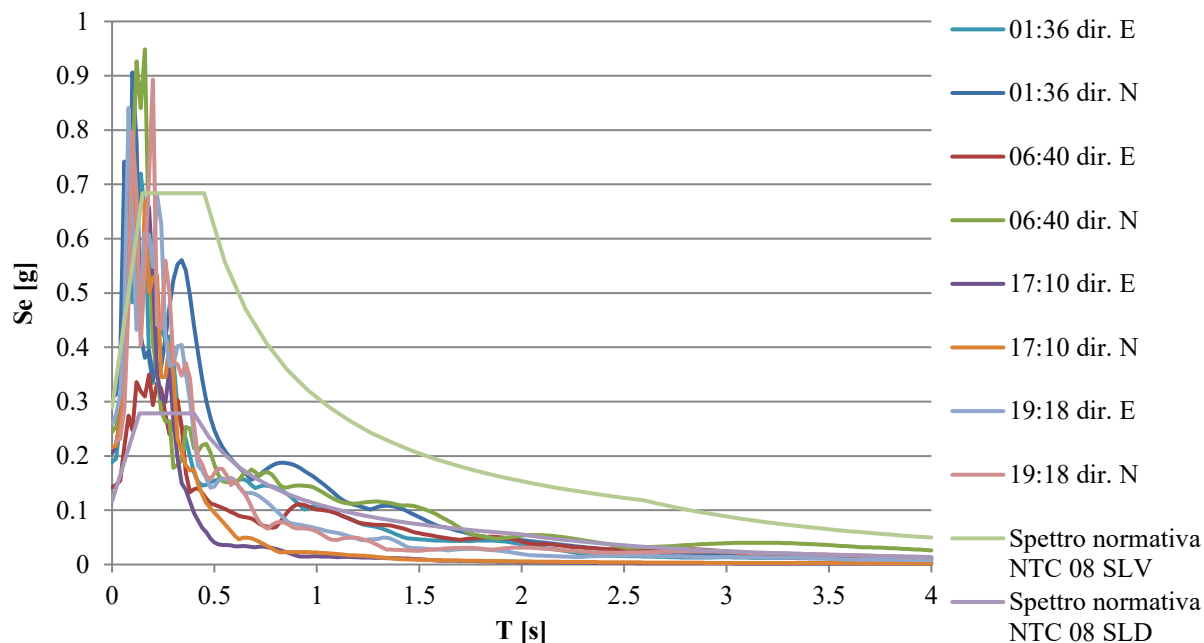


Figure 0.10: Comparison of regulatory spectra of NTC 08 to SLV and SLV with recorded spectra.

It is possible to notice how the spectra of legislation are exceeded especially for the events of August 24 and October 30, which caused the most significant damage to the structure.

2.6. Seismic base Hazard of Visso

In this subsection the basic seismic hazard of Visso municipality is analysed in brief. Specifically, it is defined as the expected shaking in terms of maximum horizontal acceleration a_g under free field conditions on flat rigid outcrop with subsurface category "A".

Using probabilistic approach, which identifies the probability that a certain shaking parameter exceeds a certain threshold in function of magnitude and duration, is in addition possible to report the seismic hazard a fixed probability of surplus P_{Vr} in a reference period V_R [14].

Thanks to the National Institute of Geophysics and Volcanology (INGV), which provides the map of the national territory by dividing it with a regular grid of points with a pitch of 0.5° , the seismic hazard map is reported below for a probability of 10% surplus in 50 years. This probability of exceedance is referred to the Ultimate Limit State for the safeguard of human life, and corresponds to a return period of 475 years.

You notice, in Figure 0.11, as for the commune of Visso you have a PGA with values between 0.225 g and 0.250 g.

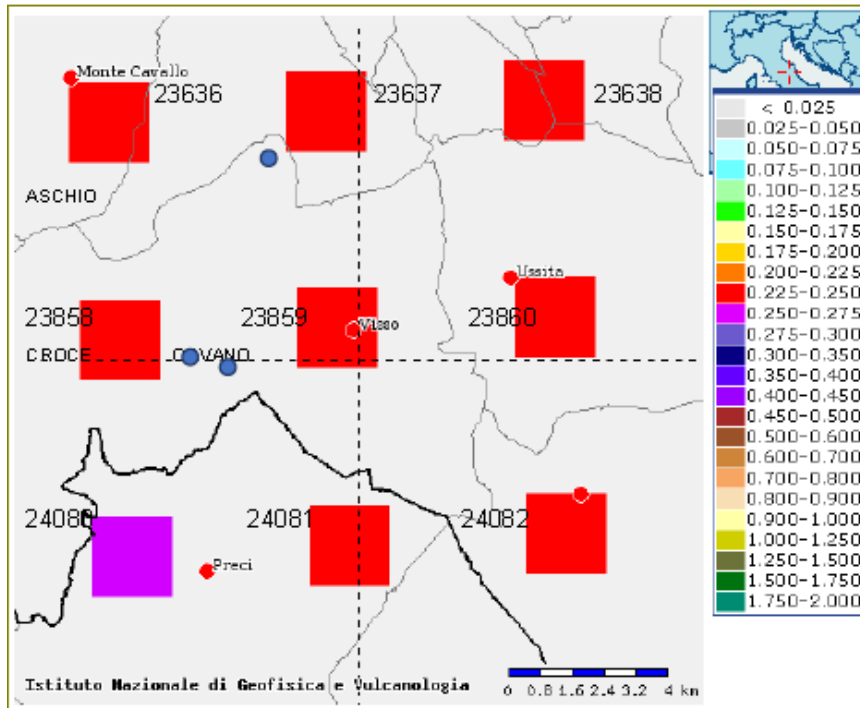


Figure 0.11: Seismic hazard Map with parameter a_g with 10% in 50 years [14].

2.7. Reference Legislation

During the following sub-chapter we want to report a history of the transposition into the Italian legislation of seismic actions. The first Italian legislative measures in terms of seismic prevention were then taken after the devastating earthquake that destroyed Reggio Calabria and Messina in 1908. Thus in 1909, about four months after the catastrophic event, the Royal Decree N ° 193 was enacted, containing mandatory technical norms and for repairs and for the new construction of buildings valid for the territories present in the list of seismic Municipalities. The list, which initially included only several municipalities of Southern Italy, was updated from time to time following the occurrence of further seismic events, through appropriate Laws, of which are reported below the main:

- Legislative Decree 1526: Quantifies the seismic forces and their distribution along the height of the building;
- Royal Decree n°2089: it establishes that the horizontal and vertical seismic forces do not act at the same time, and requires that the design be carried out by an Engineer or an Architect;
- Royal Decree n°431: introduces two categories of different hazards that, to which different prescriptions are competing, corresponds to a application of different seismic forces;
- Royal Decree n°640: enactment of specific technical directives and obligation of the municipalities to draw up their own building regulations.

In 1974 it was promulgated the “Nuova Normativa Sismica Nazionale” establishing the new framework for technical regulation, containing both the seismic classification (list of municipalities in which the norms were to be applied) and the criteria of seismic construction.

Subsequently, following the earthquakes of 1976 (Friuli) and 1980 (Irpinia), seismological studies allowed the formulation of a proposal of seismic regulation based on investigations of the probabilistic type of Italian seismicity, which was then the starting point of the current estimate of the national seismic risk. Thus between 1980 and 1984, following the proposal of the National Research Centre (CNR), and in particular the finalized "Geodynamic" project of the 1979 which made the national territory's shakability cards, the Ministry of Public Works issued a Series of decrees: the first of these (Ministerial Decree 1981) introduces the third Category A minor seismicity and coefficients lower than the first two already classified in the Ministerial Decree of 197.

Following the Last Seismic Events that have interested the center Italy, it was approved on D.L. 17 October 2016, No. 189-"urgent Interventions in favour of the populations affected by the seismic events of 2016, converted into Law The 15 December 2016.

Regarding the regulations in force in Italy in the year 2019, or ministerial decree 14/01/2008; The chapters referenced are:

- cap. 7 "Progettazione per azioni sismiche";
- cap. 8 "costruzioni esistenti";
- cap. 11.2 "materiali per uso strutturale: muratura".

3. Characterization of the structure

In the following chapter we will describe the architectural characteristics of the Elementary and Maternal School "Pietro Capuzi" in Visso. In particular, the building which is spread over four levels of which three above ground (piano rialzato a 70 cm rispetto al piano campagna, primo piano e sottotetto), having a total volume of 4800 m³ and a plan area of about 600 m² [15]. It possesses a form comparable to an inverted T formed by a rectangular part extending in the NO-SE direction and one in the orthogonal direction to it of smaller dimensions. The school, as you will see in the following, is subject to monitoring by the OSS and studies by the project ReLUIS (Rete dei Laboratori Universitari Di Ingegneria Sismica; (<http://www.reluis.com>)).

The artifact dates back to the '30 and was subject to some improvement interventions started in the years '90. Below is the plan of the building (Figure 0.1):

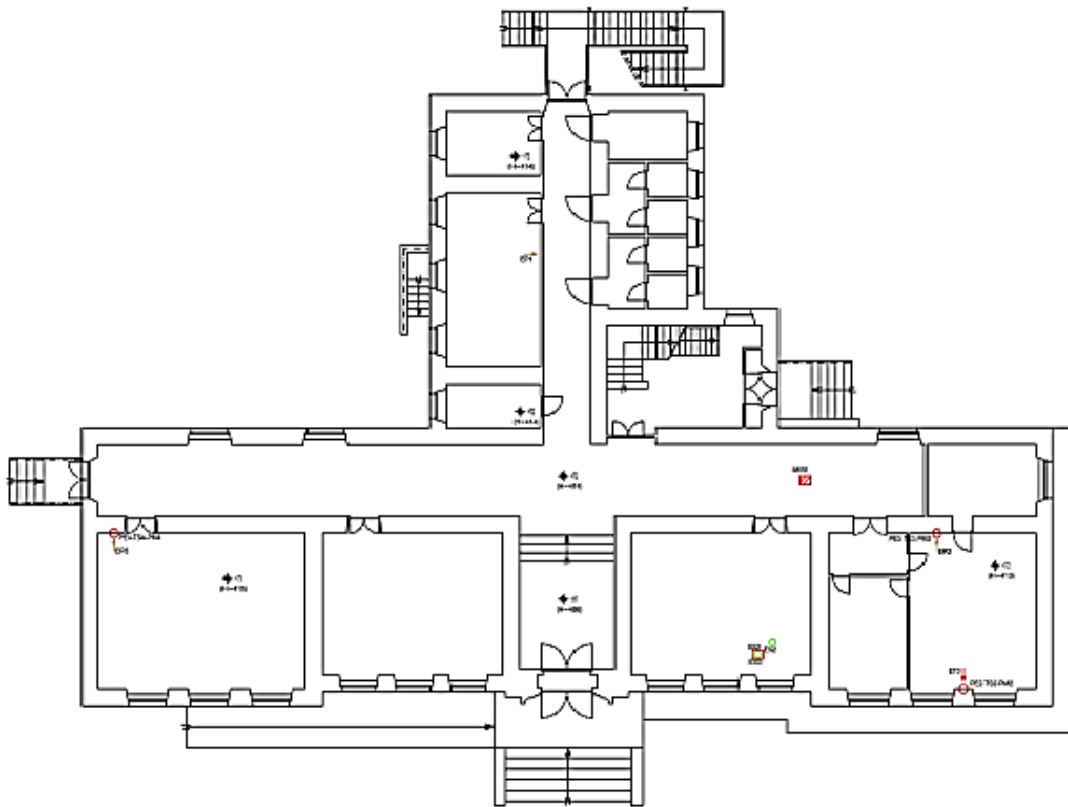


Figure 0.1: Plan of the raised floor of the school "Pietro Capuzi" in Visso [15].

Having technical reports available following the analyses and the inspection on December 2016 ([16], [17]), it was possible to define the following:

3.1. Vertical structures

3.1.1. Types of Masonry

Specifically, the building develops in a regular way and consists of two types of masonry [15]:

- the first typology present in an extended way in the building is formed by a masonry in split stone blocks with injections of mortar for the purposes of consolidation. It is necessary to keep in mind that some walls constituted with this typology have undergone interventions of consolidation with insertions of mortar or the insertion of pillars in solid bricks [15];
- the second consists of a brick masonry full in the form of walls or masonry pillars (This type is present in more sporadic ways within the structure).

Following the survey carried out by the University of Genova on date 8-12-2016, it was possible to notice in some ground floor plug walls the presence of brick rows not arranged in a conformal manner. Moreover, the basic masonry has appeared sufficiently regular, with dimensions of the 30 x 15 cm ashlar and good quality of the mortar, which denotes a certain compactness and resistance to the punching [15].

The murar males, continued from the foundations to the roof, have a thickness varying from 67 to 85 cm at the first level, from 66 to 87 cm at the second level and from 50 to 78 cm at the third level. In addition, following surveys on the structure's geometrical and mechanical properties, it was possible to identify the three planes [15]:

- Basement:
 - Masonry in unedged stone blocks of thickness equal to 83 cm;
- Mezzanine:
 - Brick masonry full of thickness varying between 8 and 67 cm;
 - Masonry in unedged stone blocks;
- First Floor:
 - Masonry in unedged stone blocks of thickness 68 cm
 - Regular appeals of semi-solid bricks.

3.1.2. Wall Bands

As a result of visual surveys and the investigations with the thermal imaging camera following the survey performed in date 8-12-2016, the following typologies of lintel were highlighted:

- the first consisting of the overlap of two bricks filled with plate on the external side and a brick pierced knife on the inner side for a total thickness of 30 cm; in Figure 0.2 the architrave on the raised top is reported [15].



Figure 0.2: Architrave of the raised floor [15].

- Second formed of knife bricks of the type with lowered arch formed by two or three courses of knife bricks, this type can be referred to the entire building excluding the wall at the main entrance of the school [15].

Following consolidation intervention on lintels, in order to improve the behaviour of the masonry belts, partial circling of the openings was carried out on the first floor, by inserting superior steel traverse connected by steel uprights to circle the masonry pillars between the adjacent openings. It is therefore now possible to summarize briefly the interventions of consolidation which have enabled structural improvements to be achieved; these interventions were initiated in the Nineties following the seismic event that took place in 1997 and which affected the Umbria and Marche Regions. In particular, the structure underwent [15]:

- Remediation of the most significant lesions through the "sew-scuci" technique;
- Injection with lime mortar in correspondence of some pillars;
- Execution of a brick masonry curtain full of some pillars in the area where the stairwell is stressed;
- Insertion to the quota of attic floors of UPN profiles nailed to the masonry in order to increase the flexural stiffness off the plane;
- Partial circling of the openings on the first floor of the main façade, made by inserting a superior steel traverse connected to steel uprights, to circle the masonry pillars between the adjacent openings. There is no lower crosspiece to close the circle;
- Insertion of chains with the installation of tensor sleeves.

3.2. Horizontal and Cover

In the following section is introduced the horizontal elements constituting the structure, with particular reference to the specific characteristics of the intermediate floors and the cover.

3.2.1. Intermediate slab

The horizontal components of the structure can be classified in three different typologies [15]:

- floors that unload directly on the ground formed by an armed slab in concrete resting directly on the ground, e presenta uno spessore totale pari a 6 cm;
- Wooden slab in Latero-double-edged cement formed by joist (8x17 cm) with 1 or 2 rows $\phi = 8/10$ mm, perforated bricks (32x17 cm), concrete insole, 5 cm high, 2.5 cm background and top finishes of 2.5 cm and 2 cm lower for a total thickness of 35 cm Rca. The Interaxis of the rafets, as emerged from the surveys with pacometer is about 40 cm.
- Slab in double-edged concrete; attic floor in a lateness section 8 cm and wheelbase 100 cm and perforated brick with addition of inert filling material.

The pavement is in grit in the corridors and tiles in the classrooms, considered on average of thickness equal to 2.5 cm.

3.2.2. Cover

The roof cover has in a non-regular manner two/three courses of purlins resting on pillars of backbone and, in correspondence of the compluvia and displuvi, of wooden struts are pushing on the cantonal at the height of the concrete curb perimeter reinforced. The second warp of strips sustain a mantle in tavelle on which the copps rest [15].

As consolidation interventions It is possible to note the substitution of some bays of the fallen wood cover and which had static problems: three central roof flaps and facing the façade were replaced with laminated timber elements [15].

3.3. Connections

Always following the survey carried out in date 08-12-2016, wall-wall and wall-horizontal connections are of good quality in relation to the damage observed, as a testimony to the effective cushioning between the various components. There were no significant pseudo-vertical lesions between the internal and external walls or tipping off the plane, and there was also a prevailing activation of a global response in the plane of the walls [15].

Wall-Horizontal Connection System

In general, the observed damage has shown an effective connection between walls and horizontal. In the floors were found slight lesions to the attack of the walls that however appear justified above all considering the level of total severity of the damage suffered by the artifact.

In the following Figure 0.3 it is possible to notice minor sub-horizontal lesions to the interface with the internal masonry on the first floor, this testifies to the effective collaboration between the walls and the horizontal [15].



Figure 0.3: Minor sub-horizontal lesions to the interface with the internal masonry on the first floor [15].

To ensure effective collaboration, a reinforced concrete curb at the height of the cover tax and a circle with UPN profiles are presented; it is also observed the presence of thick kerbs also in correspondence of the scaffolding between the raised top and the first floor.

As will be brought back in the next chapter concerning the damage, following the earthquake, the only obvious problem occurred in the building due to a lack of cooperation between vertical and horizontal wall is the activation of a local mechanism that affected the cantonal in correspondence of the top floor in the extreme north wall and the wall adjacent to it. One of the vulnerability elements identified as potential cause of the activation of that response off the plane consists in the pushing action of the corner strut of the cover.

3.4. Monitoring systems

Initially, it is important to emphasize that the school of Visso is part of the network of strategic buildings monitored by the *Osservatorio Sismico delle Strutture* (OSS) (<http://www.protezionecivile.gov.it/attivita-rischi/rischio-sismico/attivita/osservatorio-sismico-strutture>). The OSS is a nationwide network founded by the Italian *Dipartimento della Protezione Civile* (DPC) in the 1990s with the aim is to monitor several strategic Italian buildings, such as bridges, schools, hospitals and city halls [18].

In particular, the OSS allows to evaluate the damage caused by an earthquake to the monitored structures, extendable to similar ones that fall into the affected area, thus providing useful information to the civil protection activity immediately after an earthquake. The OSS allows, on the one hand, to keep under control strategic structures for the management of a seismic emergency and to evaluate its state of damage, on the other, it makes available to the technical-scientific community original data which serve to understand the response of structures to an earthquake.

When a construction of the OSS is hit by a significant earthquake, the monitoring system records the movement of the terrain and that of the structure; Following the transposition of the data, the server processes the recordings, producing a relationship with the maximum

values and some descriptive parameters, which allow to evaluate both the incoming earthquake and the induced vibrations of the structure and the relative state of damage.

As regards the monitoring system, it is generally composed of sensors distributed on all the floors of the building and on the ground, in order to adequately reconstruct the vibrations on the structure and to estimate the damage in qualitative/quantitative manner.

In the specific case of the school of Visso, there are 10 biaxial accelerograms installed on the various decks, and one triaxial positioned at the base of the building: the first measure the response of the structure while the seconds record the acceleration of the ground and consequently the input to which the structure is subject during the seismic event.

The sensors are arranged inside the structure following the following diagrams present in (Figure 0.4):

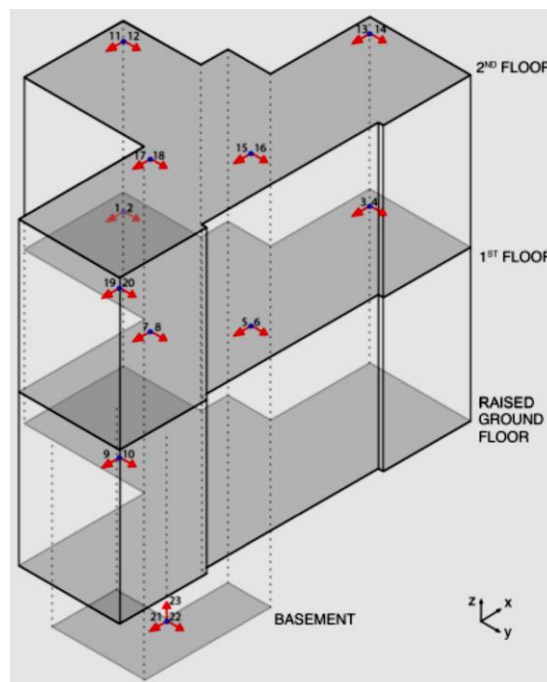


Figure 0.4: Sensor arrangement inside the structure.

The acceleration values, both those recorded at the corresponding planes and those recorded at the base, will be used as known terms within the equation of the motion in order to carry out the analysis using the black box model.

The seismic event used for the identification was the lower quake available among the main shocks occurred during the events of August/October 2016, i.e. the quake occurred on October, 26th (05:10 pm), in X direction.

The raw acceleration signals of channels 21, 5 and 15 were filtered with a bandpass Butterworth filter of order 4, with cutoff frequencies of 0.5 and 20 Hz.

For the SFFT of the signals, a 1060 points periodic hamming window has been assumed. The signals were later sampled to a frequency of 250 Hz, whereby with a time of 0.004 s. During the seismic events of October 26, 2016, these sensors recorded the following series of accelerograms expressed in g:

Sequence of 26 October, 5:10 pm

Following accelerograms were recorded by channel 21 at the basement of the building, respectively in the direction of X, Y and Z.

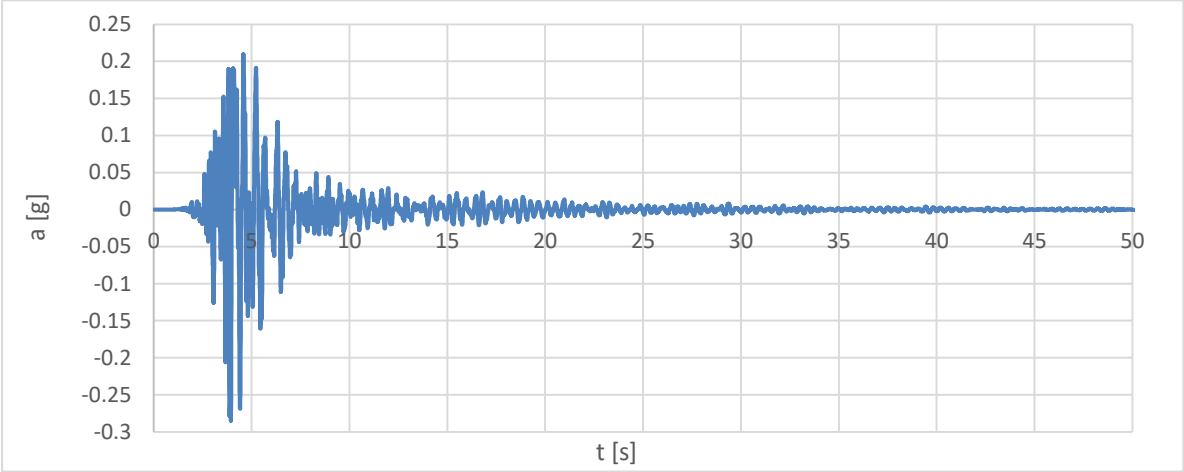


Figure 0.5: Accelerogram recorded by channel 21 in x direction.

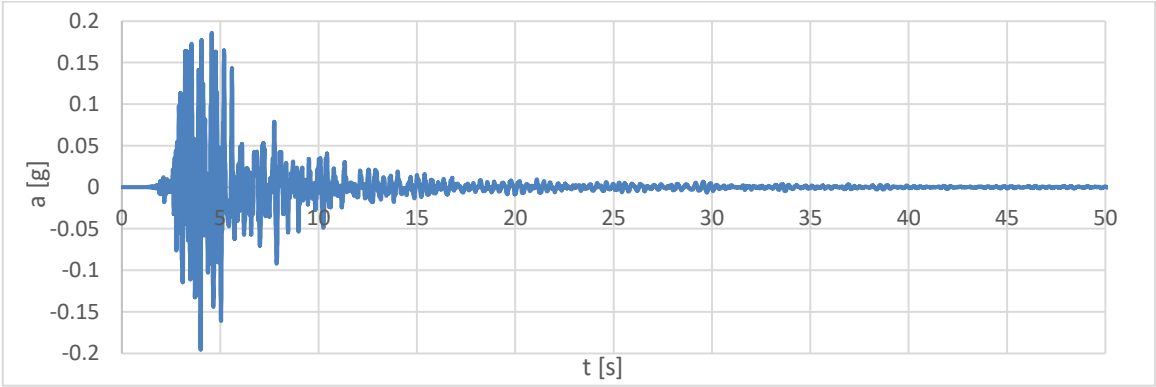


Figure 0.6: Accelerogram recorded by channel 21 in y direction.

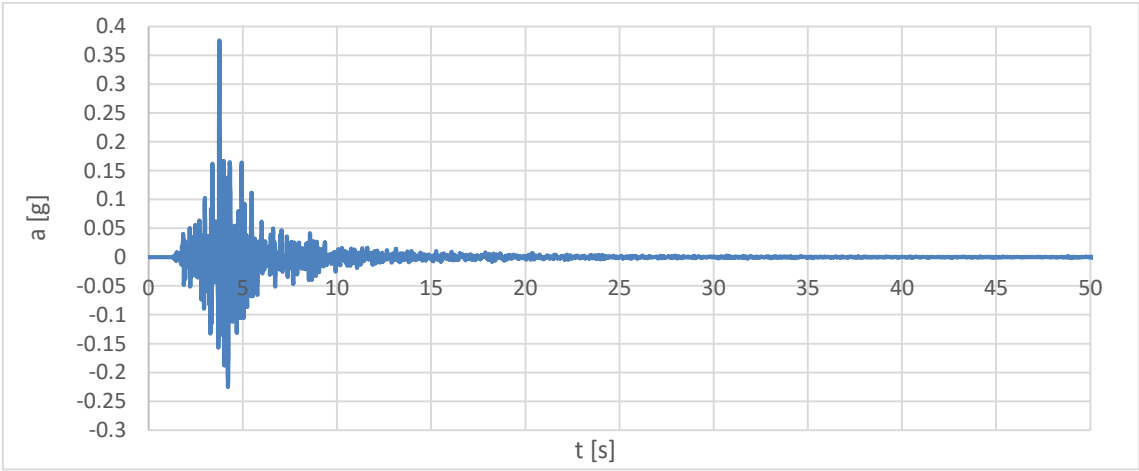


Figure 0.7: Accelerogram recorded by Channel 21 in z direction.

4. Damage reported on the structure

It is possible to report in this discussion the state of damage suffered to the structure following the events occurred on 24-08-2016 and 26-10-2016 thanks to the documentation provided by Ing. Giulio Rosi following the survey occurred in date 08-12-2016 [16].

In order to understand the evolution of the damage, it was considered in chapter 2.5 that the acceleration response spectra of the recordings taken at the basement were considered in relation to the NTC spectra of legislation: it was already a result that the shock of 24-08 was significant for Visso.

4.1. Damage reported at 24-08-2016

As a result of that event and visual investigations, there was a level of damage by the small vertical structures, whereas for the floors and stairwells there were larger entities [16].



Figure 0.1: State of damage within the structure following the event of 24 August [16].

In Figure 0.1 the extent of the damage is represented as a result of the event within the building, in which a minor damage is evident with a principle of the diagonal cracking mechanism. In Figure 0.2 it is reported instead the state of damage outside the structure, in which the damage caused by the earthquake is not significant and is still not activated any mechanism of tipping off plane [16].



Figure 0.2: State of damage outside the structure following the event of 24 August [16].

4.2. Damage reported at 26-10-2016

From photographic documentation is evident an aggravation of the damage following the event of 26-10, with consequent activation of the local mechanisms off the plane [16].

Following the images obtained during the 08-12-2016, it is possible to highlight the considerable damage to the structural elements, extended both to the first and to the second floor, and mainly localized in the male walls in the Y direction.

It is also possible to observe extended collapses that involve part of the perimeter walls of the first floor and the slab of attic consequent to the activation of a mechanism of tilting off plan. This is shown initially in the following figures, in which the overall picture of localized damage on external front is highlighted (Figure 0.3), and then we clarify the location of the damage in the plant for both the ground floor and the first floor [16].



Figure 0.3: Damage Status on external prospects [16].

It is therefore necessary to report the location of the damage in the plant distinguishing the following typologies, with legend in (Figure 0.4) [16]:

- a) mode of damage in the plane of walls (vertical carriers);
- b) mode of damage in the plane of the walls (portions of masonry including vertically aligned openings);
- c) pseudo-vertical lesions on contact between Orthal Masonry, which testify to a potential poor quality of the cushioning;
- d) Horizontal lesions in floors;
- e) Collapses of masonry portions resulting from the activation of mechanisms off the plane;
- f) collapses located in the slab.

In Figure 0.5 and in Figure 0.9 the number of inclined strokes indicates the severity in increasing order of the damage, while the letter P indicates the simultaneous lesion of the vestments.

-  a) Danno nel piano maschi
-  b) Danno nel piano fasce
-  c) Lesioni pseudo-verticali
-  d) Lesioni orizzontali
-  e) Crollo muratura
-  f) Crollo solaio

Figure 0.4: Legend of the damage [16].

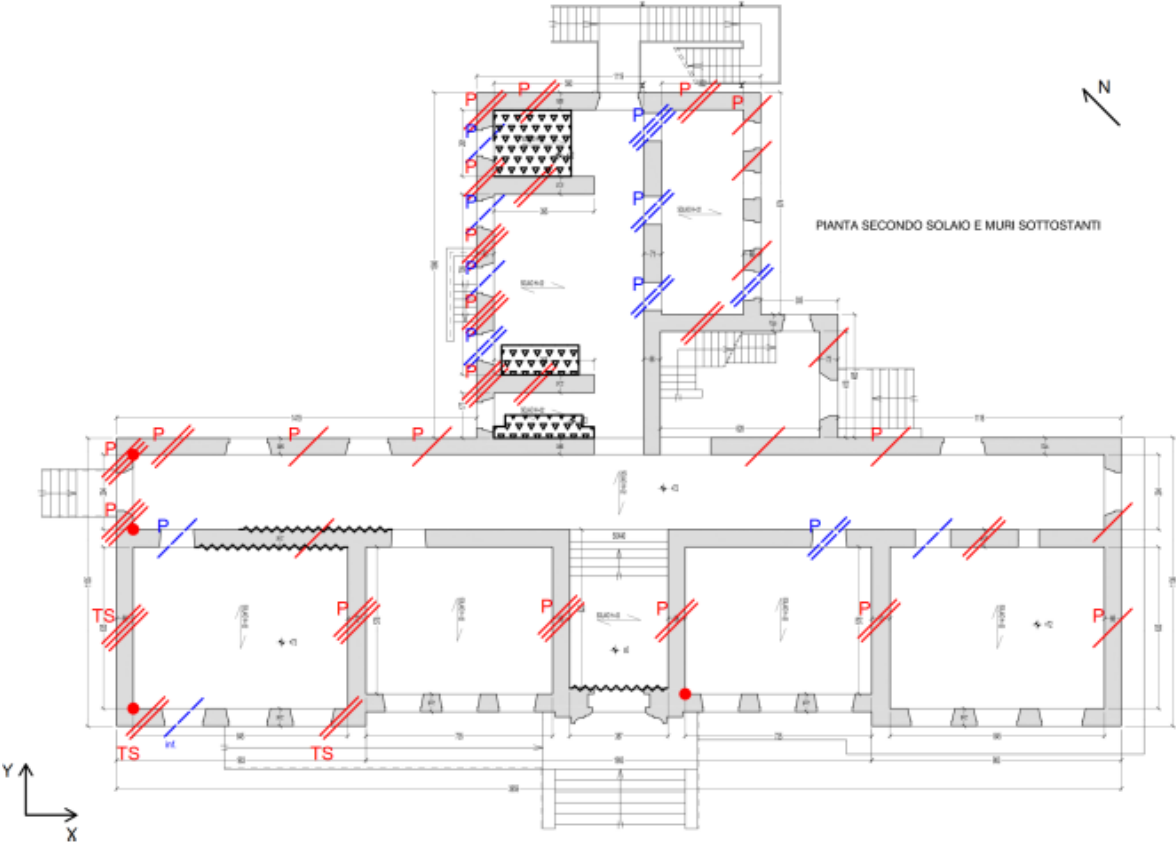


Figure 0.5: The damage related to the ground floor plan [16].

Regarding the plant referred to the **Ground floor plan** (Figure 0.5), the totality of the murar males is damaged both in X and Y direction, with diagonal cracks of considerable amplitude (especially in the Y direction) that show a prevailing response to shear; the bands, however, appear to be damaged sporadically in part A of the structure, while in part B in a serious way. It is specified that a is the horizontal rectangular portion of the T upside down, while B is the vertical part orthetal.

In the following Figure 0.6 it is reported the cut injuries for diagonal cracking occurred on the ground floor in the male walls of the body A oriented towards Y [16].



Figure 0.6: Shear injuries for diagonal cracking in the males of the body A oriented Y-direction [16].



Figure 0.7: Shear-sliding Lesions in the Northwest wing at the cantonal male [16].

Similarly in Figure 0.7 we can highlight the very serious shear-sliding lesions in the North-West wing of the structure at the male cantonal [16].

In Figure 0.8, instead, two photos of the inside of the structure are shown, showing serious pseudo-vertical lesions always in the Northwest wing of the body A [16].



Figure 0.8: Internal vision with severe pseudo-vertical lesions in the North-west wing [16].

Contextually, in Figure 0.9 it shows the state of damage and cracking of the **Foreground**, with severely damaged wall males in body A in the Y direction and with only a few of them manifesting severe damage in X-direction [16].

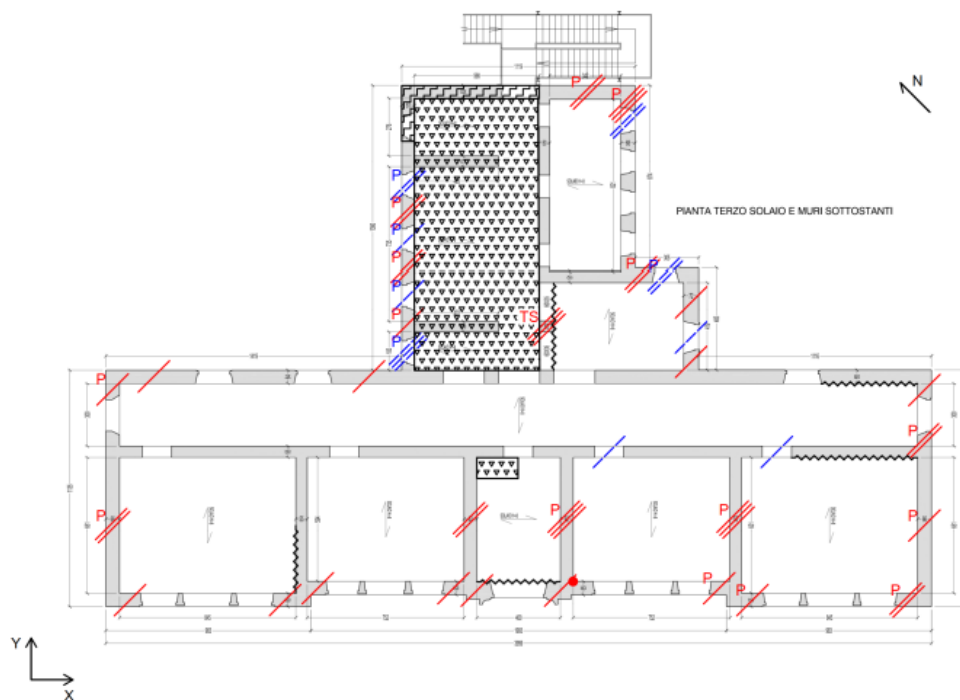


Figure 0.9: Picture of the damage reported to the plan on the first floor [16].

The males on the first floor are severely damaged in the body A in the Y direction, while in the X direction only a reduced number has significant damage. Is emphasized the presence of diagonal cut lesions in males of body B concentrated on the North-West and Southeast sides;

in correspondence with the cantonal, there was also the extensive collapse of the bearing masonry and the reinforced concrete curb (Figure 0.10) [16].

The masonry bands are damaged in a way contained on the body A, but in a serious way and extended on the body B, while on the floor of tread are evident two extended collapses, one in the compartment at the top of the stairs, and one in correspondence of the cantonal North of the body B. In Figure 0.11 it is shown instead the upper loft of attic in which it shows the presence of a collapse inside the central hall of the body A.



Figure 0.10: Expulsion of the North cantonal body B [16].



Figure 0.11: Extended Collapse of the attic floor [16].

It is therefore very serious the level of damage on the first floor, because of the collapses that have affected horizontal and vertical structures [16].

5. Nonlinear identification

5.1. State of the art

In this section we will introduce methods by which it has been possible to acquire skills related to the hysteresis in the soils, the degradation and the reduction of the stiffness.

For soils a certain level below the ground surface and far from adjacent structures, under symmetric cyclic loadings, the shear stress–strain relationship exhibits a hysteresis loop, as shown in Figure 0.1 (a). The hysteresis loop of a typical soil can be described by the path of the loop itself or by parameters that describe its shape. These parameters are the inclination and the breadth of the hysteresis loop, shear modulus, and damping [19].

Figure 0.1 (b), instead, shows a hysteretic loop describing variations of secant stiffness with the number increase in cyclic loading, which is used to describe the secant stiffness degradation of the soils in an equivalent linear model. It can be seen that the openness of the hysteretic loop increases with strain amplitude, which is actually an effect of the immediate past history of the soil [19].

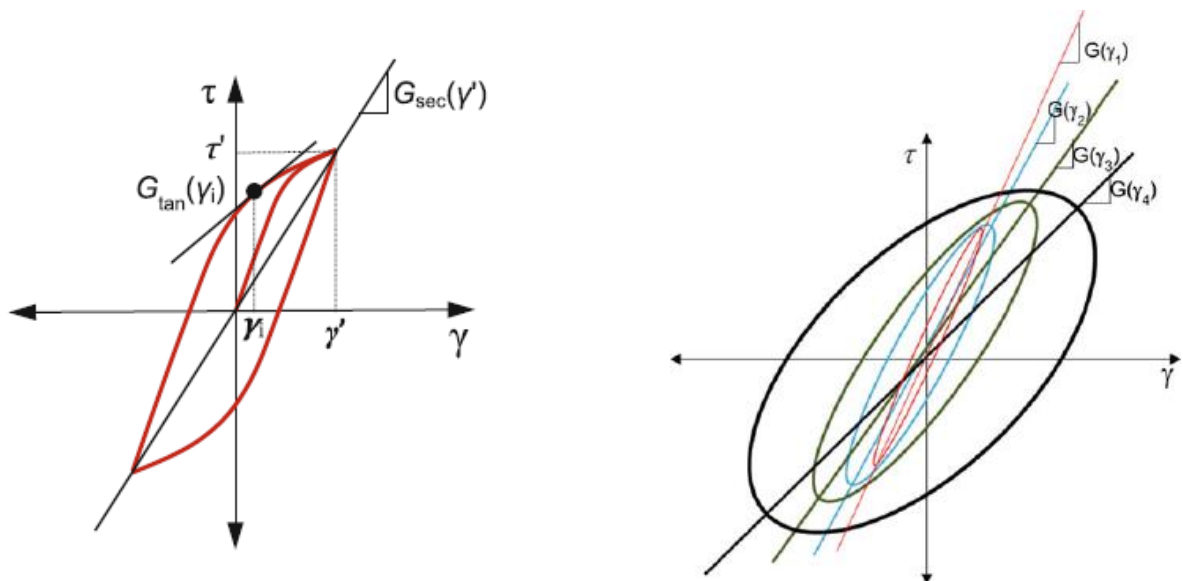


Figure 0.1: Secant shear modulus G_{sec} and tangent shear modulus G_{tan} in a hysteresis loop [19]; (b) Variation of the secant shear modulus with the number increase (1, 2, 3..n) of cyclic loading in an equivalent linear model [19].

5.1.1. Masing model

Originally developed to describe the plasticity of metal, Masing's rule assumes that both the backbone curve and cyclic response are stable. However, this may not be the case. In practice, it may be feasible to incorporate a gradual change to the backbone curve as cyclic loading effects accumulate [19]. Furthermore, the damping at large strain that results from the use of Masing's rule or the extended Masing's rule tends to be over-estimated relative to laboratory measurements [19]. On the other hand, when adopting Masing's rule and the extended Masing's rule, zero damping is implemented at small strain level, where the modulus reduction curve is linear. Even if this is theoretically true, it contradicts laboratory test observations, as at small soil strain conditions, energy dissipation does occur.

To solve this problem, one may add a viscous damping in the form of dashpots embedded within the material elements or introduce a numerical scheme that can produce nonzero damping at small strains even though the soil damping is actually neither perfectly viscous nor hysteretic.

In this Figure 0.2, at the initial loading stage, the stress–strain relationship follows a backbone curve. The shape of the stress–strain curve remains unchanged during the unloading and reloading stage, but with the origin shifted to the loading reversal point and a scaling of values of curves, which is often referred to as Masing behavior [19].

It is important to say that many nonlinear soil models to describe the hysteretic behaviour for unloading and reloading follow Masing's rule and extended Masing's rule, which are adopted in conjunction with the backbone curve to describe unloading, reloading, and cyclic degradation behaviour of soil.

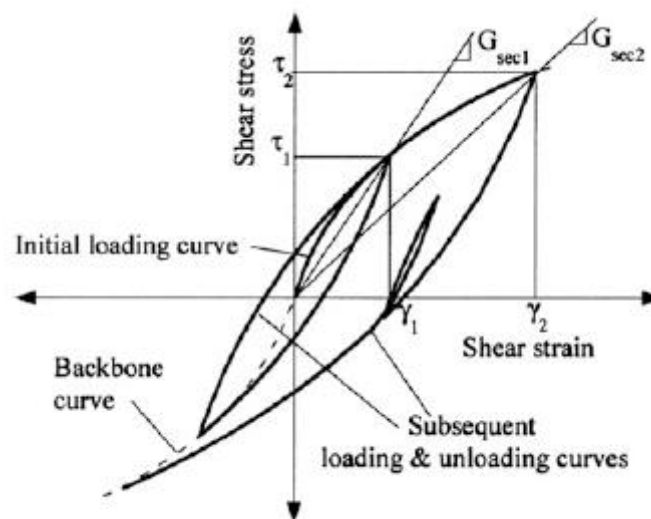


Figure 0.2: Hyperbolic nonlinear soil model with extended Masing model to define loading and unloading behavior [19].

5.1.2. Ramberg-Osgood-Masing model

To refer to what was said before, always starting from Masing law, it is possible to introduce Ramberg-Osgood-Masing model, in which it is identified an idealized stress-strain loop obtained for a soil specimen subjected to a simmetrical cyclic shearing stresses [20]. In Figure 0.3 the curve ACODB, corresponding to the locus of the tips of all possible hysteresis loops, is defined as the backbone curve for the soil specimen [20].

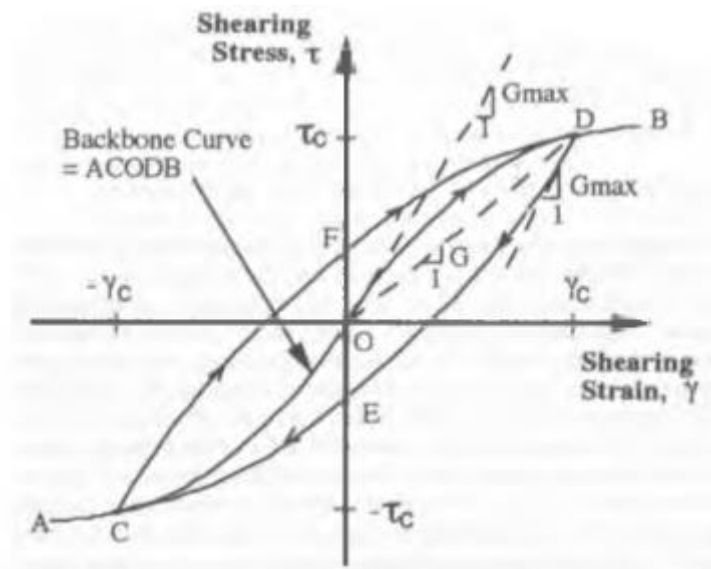


Figure 0.3: Backbone curve and associated hysteretic curve [20].

The portion of the backbone curve which is determined with the torsional shear test is shown by ODB in Figure 0.3.

5.1.3. Ishihara

Soils that are subjected to strains larger than about $10e2$ tend to exhibit changes in their properties not only with increasing shear strain but also with repeated application of loading cycles (Ishihara, 1996).

Ishihara (1996) states that the change verified in shear modulus and damping ratio between cycles depends on the effective confining stress during loading.

In these strain ranges, shear strains are not enough to describe the soil behaviour, since volumetric strains start to become an important part of soil behaviour. For repeated loading cycles, volumetric deformations start to accumulate, and the hysteresis loops start to become more inclined and with a smaller area (Chitas, 2008).

Similarly to the threshold that is defined between linear and non-linear elastic behaviour in the small strain range, in the medium strain range a threshold from which volumetric strains

start to become relevant is defined. This threshold is usually known as the volumetric shear strain threshold (Vucetic, 1994).

As this last method is used for specimens prepared in the laboratory, with selected materials and with known boundary conditions, it is difficult to apply it for problems on site, in which there are widespread heterogeneity and unidentified boundary conditions. This is going to testify to the fact that you are holding a high amount of models as far as lab analyses. [21] [22]

5.1.4. Models used

Following the presentation of the previous models and the considerations made, it was decided to adopt in the course of the analysis a simplified black-box model with three DoF: the first of which is the mass of the ground and that of the raised plane, the remaining DoF are represented, respectively, by the masses of the first floor and the second floor. For the interaction between them, following a schematization equivalent to Mass-Spring, the constitutive laws adopted will be the rate-independent Bouc-Wen for the DoF inherent in the structure, and modified, rate-dependent, Davidenkov for the DoF inherent in the terrain. The latter, since the original formulation was adapted to only laboratory models subject to cyclic loads with constant amplitude, was modified in such a way as to take into account loads with amplitudes varying in time. As you will see next, the model will be a combination of a degrading nonlinear spring in parallel with a viscous term. The nonlinear degrading spring is in turn divided in a linear elastic degrading term and a non-linear elastic term.

5.2. Acquisition of experimental data

To obtain information concerning the geological composition of the soil of Visso, geophysical tests were carried out, through which it was possible to obtain the fundamental frequency of the soil and the stratigraphic composition.

Site geophysical tests based on the propagation of seismic waves allow the estimation of elastic modules at very small deformation (initial tangent modules), because the sources used for the generation of waves release modest amounts of energy, which at most can cause localized plasticization phenomena around the point of application [23]. For this reason, the use of geophysical tests in the geotechnical-seismic characterization of construction sites is mainly aimed at determining the shear module G_0 and reconstruction of layering geometry of deposits (Lai et al., 2000). As regard the latter, one of the most relevant aspect in relation to local seismic response studies is the definition of the position of the bedrock [23].

From the point of view of characterizing the mechanical materials properties, the geophysical tests aimed at determining the propagation velocity of shear waves are particularly important. Tests based on speed propagation of compression wave are less relevant because, in the light of the particle and multi-phase nature soil and the theory of the propagation of seismic waves in saturated porous media, it is strongly influenced by interstitial fluid compressibility and

therefore does not constitute a valid indicator of the elastic properties of the solid skeleton. [23].

5.2.1. Notes on seismic refraction

As far as non-invasive tests are concerned, techniques based on the propagation of waves, such as refractive seismic and reflection, are mainly used to map the roof of the bedrock; the contrast of impedance between the latter and the materials above in terms of compression waves is in fact marked, even in the presence of an aquifer [23]. The seismic refraction is based on the phenomenon of critical refraction, which it involves the birth of a head wave that at some distance from the source arrives before the direct wave. The determination of this distance and the slope of the arrivals relative to direct waves and refracted waves in a diagram of first arrival times – distances (Dromocrona), allows the characterization of the deposits of soil in the presence of a sufficient contrast of impedance between the different layers [24]. As regards the measurement of the speed of shear waves, refractive seismic-based tests can be effectively used with horizontally polarized sources and receivers. The main limitations are related to the difficulties of generating SH waves and the intrinsic limitations of refractive methods, due to the presence of hidden layers and speed inversions. As regards the latter, in the case of layers characterised by lower propagation velocity than that of the overlying layers, the conditions of critical refraction cannot occur and therefore the slower layer is not identified with consequent errors in the estimation of the parameters of the other layers [24]. The problem of the hidden layers occurs instead in stratified means which, while presenting values of increasing speed with the depth, are characterized by contrasts of speed and thicknesses of the layers such that the waves refracted from a horizon quickly reach the surface and are detected before the waves refracted from the overlying layer, which is not identified. The consequences concern both a lack of identification of the layer and an error estimation of the thickness of the overlying state and the depths of the refractors horizons underlying the hidden layer [23].

5.2.2. Notes on the MASW tests

The type ***M.A.S.W. (Multichannel Analysis of Surface Waves)*** is a non-invasive test based on the propagation of surface waves, which, by propagating in a confined area near the free surface, are less attenuated than the volume waves; are mainly used for estimating the velocity V_s profile. In a heterogeneous medium having variable stiffness with the depth manifests itself the phenomenon of the geometric dispersion, whereby the phase velocity with which the waves propagate becomes function of the frequency [23]. From a physical point of view this phenomenon can be explained considering that harmonic waves of different frequencies are characterised by a different wavelength and consequently affecting superficial layers of different depths and volumes of soil having different mechanical characteristics and, therefore, different propagation speed.

The relationship between the phase velocity of Rayleigh waves (VR) to the frequency f it is usually called a dispersion curve and represents the central element in the use of Rayleigh waves for the characterization of soils. In fact, the dispersion curve is a function of the physical-mechanical and geometric properties of the medium and, instead of being able to estimate it experimentally, it can be used for the solution of an inverse problem having as objective the estimation of the model parameters for the ground [23].

Inversion

The experimental information regarding the dispersion curve is so used for soil characterization, solving a mathematical inverse problem. In the solution of the inverse problem usually some simplifications are adopted, in order to reduce the number of unknowns present and alleviate the problems of non-uniqueness of the solution. On Basis of a series of parametric analyses [21] It has been shown that the number of Poisson and the density of the individual layers play a marginal role. Therefore, the process of reversal is done by considering only the speed of the shear waves and the unknowns thickness of each layer and assigning a priori the values of density and Poisson number. In the choice of these values it is necessary to take into account the presence of the flap, which entails an abrupt variation in the value of Poisson's number [22].

The inversion process is iterative: starting from a first-attempt profile, built on the basis of simplified methods, and possibly a priori information regarding stratigraphy, the problem is resolved several times by varying the parameters that define the model until the best agreement is reached between the simulated dispersion curve and the experimental one.

Usually minimization algorithms at least squares are used to automate the procedure.

5.2.3. Notes on Down-Hole tests

The Tests down-Hole (DHT) represent a compromise in terms of accuracy and cost of execution because the use of a single hole allows considerable savings. The mechanical perturbation occurs in this case on the surface of the campaign plane in the immediate vicinity of the hole and the wave is detected by one or more receivers placed inside the hole itself [23]. The measurement is then repeated by varying the depth at which the receivers are placed. Interpretation can be done by following at least two different approaches. One possibility is to refer to the time interval between the first arrivals of P and S waves to two receivers positioned at different depths (distance typically between 1m and 2m) by assigning the estimated speed to the intermediate point.

This approach allows a high spatial resolution and a local estimation at different depths, but unfortunately it suffers much of the uncertainties in the determination of the moment of first arrival to the two receivers [23].

An alternative strategy is based on the interpretation of the direct times with the construction of a dromocrona that represents the variation of the first arrival times with the depth. The average gradients identified for different layers on the basis of the stratigraphic indications

obtained during the execution of the holes and the discontinuity points identified in the Dromocrona allow the estimation of the average propagation speeds for each layer [23].

5.2.4. Notes on passive tests

The experimental dispersion curve can also be obtained from passive measurements, exploiting the microtremors generated by anthropogenic actions and natural phenomena in the surrounding areas to site of interest ([25]; [26]; [27]). Passive measures are typically related to low frequency harmonic components and therefore allow characterizing up to several tens and sometimes hundreds of meters deep [23]. Acquisitions must be preferentially made using two-dimensional provisions of the receivers on the free surface, in order to be able to also make an identification direction of propagation of the detected wavecomponents. The passive measures carried out using linear shorings lead to a correct speed estimation only if the background noise is uniformly from all directions. For this reason it is always advisable to accompany them with active acquisitions on the itself, so that it can have at least one match, for the frequency intervals where possible, on the estimation of the dispersion curve with both the passive data and the active one [23].

5.2.5. HVSR Method

The HVSR method is a single station passive seismic test that highlights the frequencies at which the ground motion is amplified by stratigraphic resonance (http://www.geoamandola.it/pdf/Scopi_stratigrafico-sismici.pdf).

Being a passive type test, excitation source is the noise in the soil. In particular, the analysis consists of the measurement, and the subsequent elaboration, of the Environmental Microtremor in its three spatial components (x, Y and Z or E-W, N-S and Up-Down) at various frequencies.

Analysis of the spectral components of the recorded tracks can be:

- Derive the fundamental (or resonant) frequency of the site;
- Obtaining an interpretation of the high-depth seismic stratigraphic profile with estimation on the bedrock depth (seismic or lithological substrate) and the $V_{s,30}$ parameter (Average speed of waves S of cut in the first 30 meters of depth).

A soil vibrates with greater amplitude at specific frequencies (for the note of Resonance) not only when it is excited by an earthquake but also when it is excited by a tremor of any source; this means that the measurement of the resonance frequencies of the soil is possible everywhere and in a simple way, even in the absence of earthquakes.

The frequencies to which the resonance is manifested are described in the relation $f=V_s/(4*h)$, Where V_s represents the speed of the shear waves in the layer that resonates and h the thickness of the layer.

The test takes its name from the ratio of the horizontal spectral component H to the vertical one V , and it is from the graph of the ratio of the spectral components that the frequency is highlighted.

5.2.6. Case study

With regard the case study, several tests were carried out, including, respectively, three passive tests at single station HVSR (performed in the immediate vicinity of the structure), a Down-Hole test (performed in L. Go Filippo Corridoni at about 150 meters from the school) and a spreading MASW (also executed at the structure). In Figure 0.4 it is possible to notice the investigation field carried out during the seismic microzonation following the recent earthquakes [17].

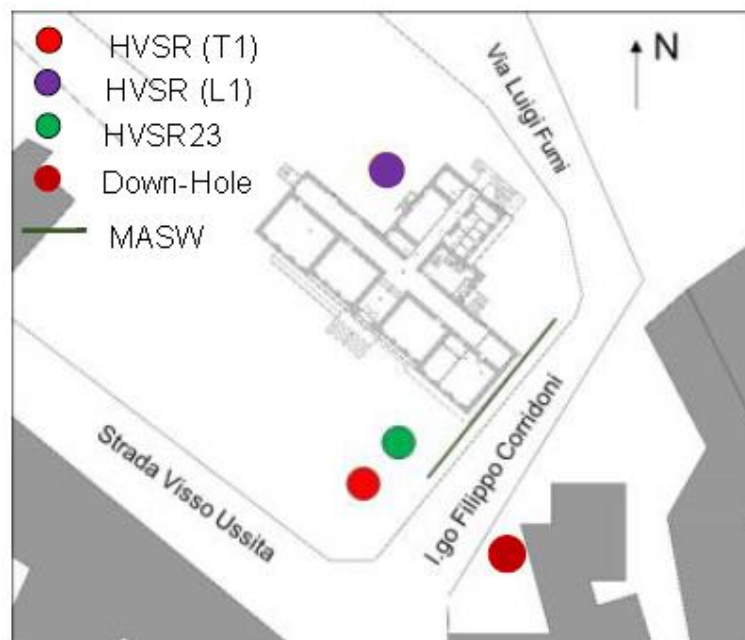


Figure 0.4: Plain view of the school and location of the surveys [17].

A borehole was drilled down to 35 m, highlighting the dominant presence of a silty-sandy gravel layer (SG), in which clayey silt (CS) and silty clay (SC) lenses are locally interbedded, as shown in Figure 0.5; and the water table was intercepted 2 m below the ground level [17].

In the borehole was performed Down-Hole test, leading to the profile of shear wave velocity V_s . In particular, the location of geognostic continuous coring survey is been identified with extreme care so that it can be representative of one of the microzones more significant, from the point of view of the areal and volumetric development of the soil of coverage, the urban planning of the area, the damage suffered as a result of the strong shocks that characterized the recent seismic sequence. In addition, the hole was conditioned (cementation and installation of the protective cockpit) to allow the execution of the test.

As far as MASW is concerned, to obtain a good resolution in terms of frequency, in addition to using 4.5 Hz geophones, a seismograph with 24-bit dynamics has been used [17]. In the execution of the test was used as energization system a beat hammer of 8.00 Kg, the source was placed to a distance of 5.7/10 m from the first geophone, with *Shots Conjugated*, for four acquisitions total [17].

For HVSR passive station seismic test, instead, the measurements were performed with two triaxial tromographs for environmental microtremors with acquisition times of 1200 s [17].

As it can be seen from the Figure 0.5, overall the speed profile tends to increase with the depth, showing a significant impedance contrast around 18 m and an inversion around 26 m, exactly where the silt lenses are thicker and closer to each other [17].

Moreover, the DH results are in fair agreement with the V_s profile measured through a MASW test close to the borehole.

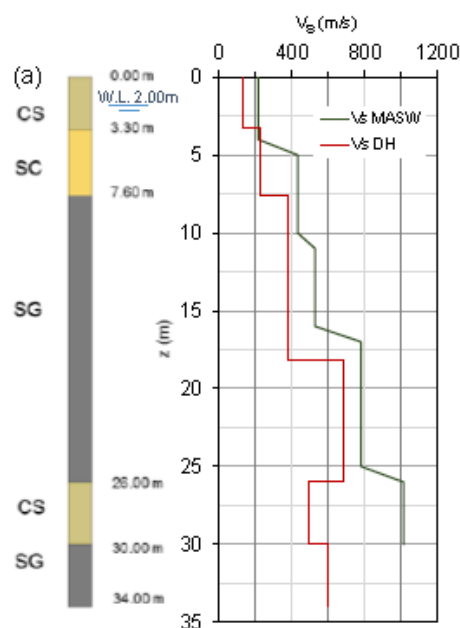


Figure 0.5: Soil profile and V_s profiles measured through DH and MASW technique [17].

This is reflected in the following Figure 0.6, made available thanks to the collaboration with UniNa and UniSannio, which shows the frequency through a peak of the curve, generally due to a minimum of the vertical component.

The comparison is shown with reference to three bedrock depths (35 m, 40 m and 45 m). The best agreement between measured and predicted predominant frequencies was found for a bedrock depth of 40 m, which is consistent with the geological model of the area [17].

For the identification of the frequency, the "Nakamura Technique" has been used, which, if the measures have been successful and if certain conditions of contrast of seismic impedance occur in the soil, can be used to evaluate the frequency of the site at the maximum detected on the curve.

The fundamental frequency of the site is therefore to be understood the most significant at low frequency and, in the case of study, the frequency identified is 3.64 Hz for a bedrock located at 40 meters of depth [17].

This frequency is very close to the frequency of the building.

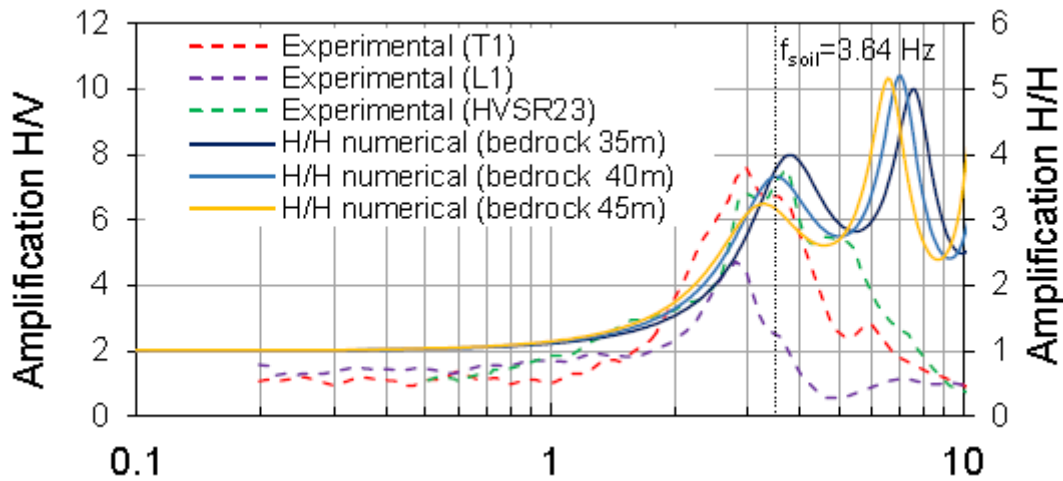


Figure 0.6: Estimation of fundamental soil frequency by HVSR method [17].

As previously mentioned, it is also possible to determine the stratigraphic profile of the soil up to high depths and the geotechnical-mechanical parameters of the various layers.

In Table 0.1 the mechanical and physical properties of the soil are summarized, the values of shear wave velocity resulting from the DH test were assumed for the layered subsoil model. The soil unit weight, γ , the Poisson's ratio, ν , and the shear wave velocity of the bedrock were inferred from data collected in the seismic microzonation.

These parameters were validated with the resonance values calculated through a 1D seismic response carried out along the same vertical.

STRATIGRAFIA	γ [Kg/m ³]	$Z_{i,min}$ [m]	$Z_{i,max}$ [m]	Δz [m]	V_s [m/s]	G [MPa]	ν [-]
Limo Argilloso (CS)	2000	0	3.2	3.2	136	38	0.4
Argilla limosa (SC)	2000	3.2	8	4.8	226	104	0.4
Sabbia ghiaiosa (SG1)	2100	8	18	10	383	314	0.3
Sabbia ghiaiosa (SG2)	2100	18	26	8	683	99	0.3
Limo Argilloso (CS)	2000	26	30	4	600	510	0.4
Sabbia ghiaiosa (SG1)	2100	30	40	10	602	776	0.3
Bedrock			40				

Table 0.1: Experimental soil parameters [17].

Thanks to the data collected following the tests carried out it will be possible to reconstruct, by code to the finite elements, the model with which we will proceed to the calibration of the mass participating in the analyzed phenomenon, and to carry out the seismic signal deconvolution (recorded at the base of the structure).

5.3. Dealing with soil structure-interaction

In order to determine the mass of soil that contributes to the phenomenon of the soil interaction structure following the seismic event being studied, a mass of known geometry was considered as a preliminary, and it was modeled up to the bedrock.

Being the school plant invers T-shaped and considering a hypothetical shape of pressures bulb stretched in the Y-direction of the structure and stretched in x direction, it was considered the external soil as if it were inconsistent, thus going up to a geometry in hexagonal type plan; in such a way as to consider a participation also of the portions of triangular terrain near the building.

Having also noticed, following a modal analysis and of inspections carried out, the occurrence of a rotational behaviour of the structure, it was therefore decided to take as geometry a mass that circumscrib this portion of soil and that could understand such a rotational movement.

As you know of a limited amount of experimental data, and in particular only the natural frequency of the soil and the relative stratigraphic composition, it will be necessary to carry out a sensitivity analysis, in order to evaluate the variability that each parameter has on the first numeric frequency. It was decided to carry out this analysis both on internal parameters of the model (tangential resistance module G for each layer), and on external parameters (boundary conditions).

Following this, it will be possible to fit the first frequency of the ground, in the direction Y, equal to 3.64 Hz, so that the mass of soil interacting with the structure can be obtained.

5.4. Ground motion deconvolution

The following chapter intends to describe at the theoretical level the local seismic response for the event of 26-10-2016 in the ground below the school of Visso; as well as the fundamental characteristics for geotechnical modelling with particular reference to the mechanical behaviour of soils and their properties.

5.4.1. Fundamental features

To give it a first definition, the RSL It can be defined as the set of variations that the seismic motion suffers in relation to the mechanical and geometrical properties of the deposits near the surface or the topography of the interest site; It is therefore necessary to refer to the stratigraphic amplification and the topographical amplification: the first one is linked to the variation of impedance within the ground, which entails an increase in the amplitude of the

displacements; the second is linked instead to a focus of energy due to the conformation of the Earth's surface [28].

During the course of the treatment will be considered only the stratigraphic amplification [28] (linked to the mechanical properties of surface soil deposits) considering a single-dimensional model that takes into account the vertical heterogeneity of the soil deposition. In the study of the local seismic response, the propagation of shear waves is usually considered; in facts, taking into account the phenomena of refraction of seismic waves and the decrease of impedance that characterizes the succession of materials of the Earth's crust approaching the surface, the horizontal components of motion associated with the seismic shock (which induce stricter actions on geotechnical constructions and systems) are mainly due to shear waves that propagate in vertical direction [29].

The construction of the geotechnical model requires first the choice of a framework of reference for modeling of the mechanical behavior of the soil. The mechanical response of soils to cyclic loads is somewhat complex and characterized by marked Non-linearity, accumulation of permanent deformation, energy dissipation and progressive decay of parameters mechanical effects due to the number of loads applied. In the presence of interstitial fluid, these issues are added to the accumulation of interstitial overpressures, if the soils are prevented or partial, which are the most frequent in terms of drainage consideration of the speed of application of the load.

The **Accurate modeling** of these phenomena requires the use of complex constitutive bonds, which, moreover, can hardly reproduce simultaneously all the specificities of soils behaviour; it would be necessary to refer to step-by-step integration procedures in the time of the equations of motion, taking into account the actual binding strain strains.

For this reason it is often preferred to refer to **Simplified constitutive Models**, which, although not rigorous, are able to reproduce adequately the response of the soils in reference to specific applications.

Therefore, as regards the seismic response of soil deposits, the equivalent linear visco-elastic approach represents a valid compromise between simplification of analyses and accuracy of results. This approach basically refers to linear visco-elastic solutions for the propagation of seismic waves, which can be easily implemented in a numerical code, by iteratively adjusting the constituent parameters according to the deformative level induced by seismic motion in the ground [30].

In summary, it is necessary for the characterization to concentrate in:

- Stratification geometry and bedrock position;
- Small deformation shear module and damping ratio;
- Decay curves of the shear module and damping ratio when the deformation level varies.

In this subsection will be treated the theory behind the Strata software, thanks to which it was possible to obtain, through deconvolution, the output accelerograms with which it will be possible to calibrate the parameters of the dynamic models considered.

5.4.2. Mechanical soil Behavior

The markedly nonlinear strains-deformation behaviour of the soils can be conveniently described by introducing either secant equivalent elastic modules or variable tangents as a function of the deformation level [23]. The Variation of the secant (or tangent) module according to the deformation is usually indicated as a decay or degradation curve of the modulus. Often these curves are reported with a normalization of the form secant with respect to the value of the module tangent to very small deformation G_0 , which also represents the value maximum of shear module. Figure 0.7 shows the trend of the tangential stress as the deformation varies (with the definition of the G_0 a very small deformation and the secant modulus G_{sec}) and the decay curve of the shear module [23].

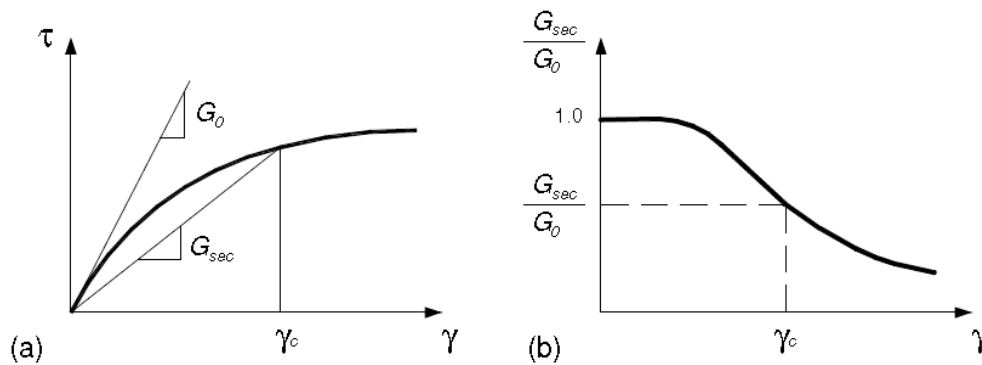


Figure 0.7: (a) Definition of the secant module of the initial tangent module (small deformation Module G_0) (b) Definition of the decay curve of the shear module [23].

As the quake is a cyclic load, it is also necessary to refer to the intrinsic dissipation of energy that occurs during the loading and unloading cycles, through the damping ratio D . It is defined as the ratio of the energy dissipation in the single load cycle ΔW and the energy of accumulated maximum deformation, specifically $D = \frac{1}{4\pi} \cdot \frac{\Delta W}{W}$.

The damping ratio is also dependent on the deformative level, as it is possible to experimentally observe a widening of the hysteresis cycles as the growth of the deformation of cyclic load peak.

As a result of the said, the following decay curves can be introduced (Figure 0.8) [23]:

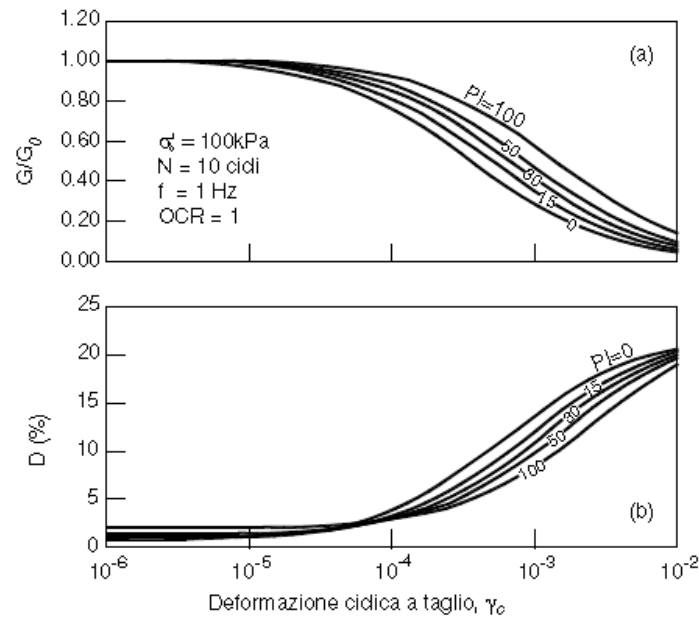


Figure 0.8: Dependence of the decay curves of the shear modulus and of the damping ratio from the plasticity index [23].

It is possible to experimentally observe how the decay curves depend on the state parameters and the physical properties of the soil, as well as the characteristics of the cyclic load applied; in particular this dependence is marked especially in relation to the variations in the plasticity index, as shown in the previous figure.

It is possible to observe in the degradation curves the existence of a small deformation interval in which the secant elastic modulus remains practically constant, by allowing in engineering terms the definition of a linearity threshold below which the behaviour of the Soil mechanic does not significantly differs from that of a visco-elastic medium Linear (Vucetic, 1994). In this range of deformations, the dissipation of energy in hysteresis cycles of Hysteresis is typically very low, with damping ratio values that rarely exceeds 1%. The threshold of cyclic linearity is increased to increase of the soil's plasticity index.

5.4.3. Equivalent linear Method

This è commonly referred to as the equivalent linear analysis, in which soils behavior is non linear, and its dynamic properties (Shear modulus G and damping ratio D) vary with shear deformation and, thus with the intensity of shaking caused by seismic motion and especially with the duration.

By Analyzing the site's response through linear equivalent analysis, the nonlinear response of soil is approximated by modifying the linear elastic properties according to the induced deformation level. Because the induced deformation depends on the soil properties, the shear modulus and the deformation-compatible damping ratio values are iteratively calculated based on the deformation calculated at the previous step [23].

Initially assuming that the deformations are null or negligible, the analyses are conducted using the values of G and D corresponding to very small deformation, so the value shear Module $G_{Max} = G_0$ at small deformation is calculated by:

$$G_{max} = \rho * V_s, \text{ where } \rho \text{ represents the density of the site, while } V_s \text{ the speed of the shear waves.}$$

On the basis of this assumption the displacement field induced in the deposit by the seismic wave and therefore the maximum shear value for the treated layer is evaluated. At this point it will be possible, on the basis of this value, to correct the stiffness module and the damping ratio using the decay curves.

Subsequently, following the increase in shear deformation, module G and damping D undergo a decrease and an increase respectively.

Since The process is iterative, G and D are recalculated on the basis of the new deformation and, for each new Layer, the new values are compared with the previous iteration and an error is calculated: If the error for all the layers is less than a defined threshold, the calculation will stop. Graphically, it is possible to see what was said in the next Figure 0.9, which highlights the initial values and iterative process [28].

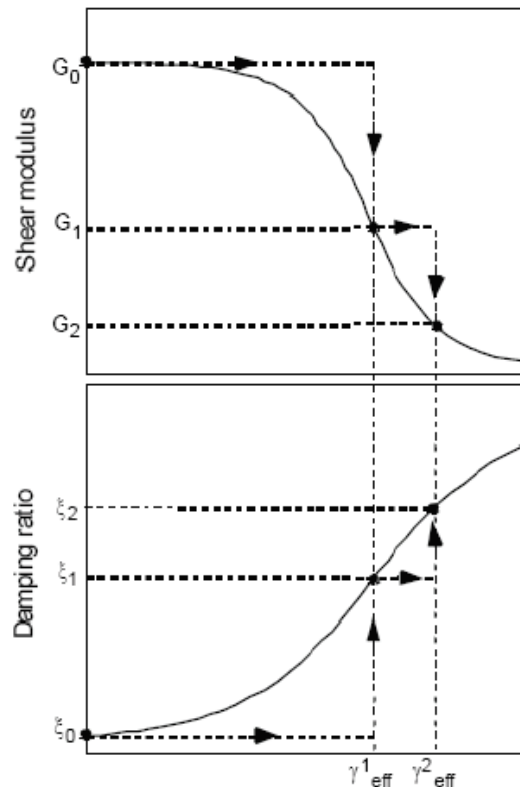


Figure 0.9: Explanation of the equivalent linear method [28].

Following this, through the assessment of displacement field, the dynamic response of the soil deposit is calculated.

In summary, nonlinear behaviour has been assumed for the soil, in which the dynamic properties vary in relation to the deformation level. In the linear equivalent method, therefore, the non-linear response of the soil is approximated by modifying the linear elastic properties of the soil on the basis of the induced tensional level.

The quantification of the local seismic response in the time domain can be carried out by referring to the ratio of the maximum acceleration values to the surface, or to the engineering point of interest, and the maximum value of reference seismic signal, it is thus possible to define the **Amplification factor** which, however, does not adequately account for the characteristics of the signals [28].

In the frequency domain, however, the quantification of the local seismic response is usually carried out by referring to a **Transfer function**, defined as the ratio between output signal of the system to the input signal [28].

One can therefore affirm that this function defines the alteration of the seismic signal produced by the soil system and, therefore, can be directly connected with the physical-mechanical and geometrical characteristics of the system. It is defined as a function with complex values, being a ratio of complex functions (Fourier spectra).

It is also possible to introduce the **Amplification function**, defined as the Transfer function module and represents the ratio of the corresponding modules of the two outgoing and inbound signals from the system. It was important to define it as this function contains the most relevant information, indicating which frequency components are most affected by the passage through the deposit. Therefore, taking into account the effects of non-linearity, the amplification function cannot be uniquely described by reference only to the mechanical parameters of the model, but will be dependent on seismic excitation and in particular of the levels induced deformative; Specifically, in a non-linear equivalent procedure, strong events will produce a marked decay of the stiffness module and a marked increase in the damping ratio, resulting in minor values of the amplification function [28].

The use of the Fourier transform also presupposes the validity of the principle of overlapping effects and therefore a linear behavior of the problem. Having ground a markedly nonlinear behaviour, it will be necessary to refer to a linearisation of the mechanical response through the linear equivalent method [28]. [31]

Another hypothesis has been used for the analysis, that is to consider only the variation of the mechanical properties of the soil with the depth compared to the campaign plane, referring to one **dimensional models** where it is assumed that the deposit is made up of soil layers with flat and parallel interfaces.

Having therefore considered a stratigraphic model, the following conditions must be imposed on the interface between the different layers:

- Continuity of the tensional state, for which it can be imposed $u_n(H_n, t) = u_{n+1}(0, t)$;
- Congruence of deformations, so $\tau_n(H_n, t) = \tau_{n+1}(0, t)$.

Where H_n represents the thickness of the n-th layer, while u_n and τ_n are the horizontal displacement and the tangential tension of the n-th layer respectively.

Returning to the transfer function, it is possible to provide a demonstration for visco-elastic soils: first of all it can be said that the solution can be obtained starting from the elastic solution using the principle of correspondence, thus introducing a complex stiffness module G^* defined as:

$$G^* = G(1 + i2D)$$

Being the transfer function defined as:

$$H_r(w) = \frac{FFT(u(0,t))}{FFT(U(H,t))} = \frac{1}{\cos k^* H} = \frac{1}{\cos\left(\frac{wH}{V_S^*}\right)}, \text{ with the wave number } k = \frac{w}{V_S^*};$$

Being able to write $V_S^* = \sqrt{\frac{G^*}{\rho}} = \sqrt{\frac{G(1+i2D)}{\rho}} = \sqrt{\frac{G}{\rho}}(1 + iD) = V_S(1 + iD)$, K^* becomes:

$K^* = \frac{w}{V_S^*} = K(1 - iD)$; the transfer function becomes:

$$H_r(w) = \frac{1}{\cos\left(\frac{wH}{V_S^*}\right)} = \frac{1}{\cos\left(\frac{wH}{V_S(1 + iD)}\right)}$$

Being our multilayer model, it will need to consider the impedance ratio α_z^* between the various layers:

$$H_r(w) = \frac{1}{\cos\left(\frac{wH}{V_S(1 + iD)}\right) + i\alpha_z^* \sin\left(\frac{wH}{V_S(1 + iD)}\right)}$$

So we found the value of the transfer function for a stratified model. Its amplification function will therefore be:

$$A_r(w) = |H_r(w)| = \frac{1}{\left| \cos\left(\frac{wH}{V_S(1 + iD)}\right) + i\alpha_z^* \sin\left(\frac{wH}{V_S(1 + iD)}\right) \right|}$$

$$\text{With } \alpha_z^* = \frac{\rho_s V_S^*}{\rho_r V_r^*}$$

A transfer function is used to compute the shear strain in the layer based on the outcropping input motion. In the calculation of the strain transfer function, the shear strain is computed at the middle of the layer ($z = h_m/2$) and used to select the strain compatible soil properties. Unlike the previous transfer functions that merely amplified the Fourier amplitude spectrum, the strain transfer function amplifies the motion and converts acceleration into strain.

In summary, therefore, the transfer function is used to estimate the seismic motion at the surface of the soil storage associated with a particular seismic motion detected on an outcrop and vice versa: in the first case the surface response will be given by convolution of the transfer function with the seismic signal, while in the second (and in the case the subject of this elaborate), the answer will be given by way of deconvolution of $H_r(w)$ with the signal. In order to perform the deconvolution of the signal, you will use the software “Strata”, computes the response for vertically propagating, horizontally polarized shear waves propagated through a site with horizontal layers. In the particular, Strata calculates dynamic site response of a column of one-dimensional solid using the linear propagation of waves with dynamic deformation-dependent soil properties.

5.4.4. Time series Method

In Time Series method, input is provided a temporal history of accelerations and FAS input is calculated from that time series using Fourier transform (FFT), in order to compute the discrete Fourier transformation on the based on time series provided [31].

The calculated FAS presents complex value and can be converted to amplitude and phase information.

As far as frequencies are concerned, they are calculated from the time step between the points and the total number of N points in the record: the highest possible sampling rate is known by the Nyquist frequency name and is defined as follows:

$$f_{N,Nyquist} = \frac{1}{2 * \Delta t}$$

Where Δt represents the time between two successive points.

It is possible to schematize the fundamental concepts of the Time Series approach in order to obtain the temporal history of acceleration on the surface [31]:

- Reading of acceleration time-series;
- Calculate the FAS input using the Fourier transform;
- Calculate transfer functions for site properties;
- Calculate FAS surface by applying the transfer functions to the FAS input;
- Calculate the surface Acceleration time-series through the inverse Fourier transform of surface FAS.

5.5. Formulations

In this section is discussed, in primis, the methodology used for the quasi-direct non-linear identification of the supposed 3 DoFs system using the Time-Frequency Distribution (TFD) computed with Short (Fast) Fourier Transform (SFFT) of the records [32], and second, the nonlinear laws assumed to replicate the dynamic response of the system are reported and introduced in the identification framework.

5.5.1. Nonlinear Identification with Time-Frequency distribution

For the identification purpose we assume to approximate any experimental records, ${}^d\mathbf{n}_e(t)$, of a general Degree of Freedom, d , in the following form:

$${}^d\mathbf{n}_n(t) = \sum_{i=1}^{d_I} {}^d p_i \cdot {}^d\mathbf{n}_i(t) \cong {}^d\mathbf{n}_e(t)$$

Where:

- ${}^d\mathbf{n}_n(t)$ is the numerical approximation of the experimental records with the expansion defined by the i -th parameter;
- ${}^d p_i$, are system parameters to be identified;
- ${}^d\mathbf{n}_i(t)$, are basic functions;
- ${}^d I$, is the order of the expansion (the total number of basic function) to approximate the d -th DoF experimental record;
- t denotes the time.

The goal of this subsection is to find in an efficient way the parameters, ${}^d p_i$, for a general DoF by using a linear TFD operator, $T(\cdot)$, allowing in this way instantaneous estimate of their values.

For this reason, we rewrite equation above as:

$$T({}^d\mathbf{n}_n(t)) \cong T({}^d\mathbf{n}_e(t))$$

Now, it is possible to write the following errors TFD equation because it is assumed a linear TFD, where ${}^d\mathbf{p}$ denotes the vector of the unknow parameters for the DoF d .

$${}^d\mathbf{E}(f, t; {}^d\mathbf{p}) = T({}^d\mathbf{n}_n(t)) - T({}^d\mathbf{n}_e(t))$$

Because we assume a linear TFD we can write the TFD of the errors, ${}^d\mathbf{E}(f, t; {}^d\mathbf{p})$ as:

$${}^d\mathbf{E}(f, t; {}^d\mathbf{p}) = T({}^d\mathbf{n}_n(t) - {}^d\mathbf{n}_e(t))$$

Then, in order to minimise the TFD of the errors, it is necessary to write the norm-2 squared ${}^d\mathbf{W}(f, t; {}^d\mathbf{p})$, for example using least-squares methods:

$${}^d\mathbf{W}(f, t; {}^d\mathbf{p}) = \left\| {}^d\mathbf{E}(f, t; {}^d\mathbf{p}) \right\|_2^2 = \text{Re}^2[{}^d\mathbf{E}(f, t; {}^d\mathbf{p})] + \text{Im}^2[{}^d\mathbf{E}(f, t; {}^d\mathbf{p})]$$

Remembering the linearity of $T(\cdot)$ it is possible to write the next formulation in terms of real and imaginary operators:

$${}^d\mathbf{E}(f, t; {}^d\mathbf{p}) = \sum_{i=1}^{d_I} {}^d p_i \text{Re}[T({}^d\mathbf{n}_i(t))] - \text{Re}[T({}^d\mathbf{n}_e(t))] \\ + j \left\{ \sum_{i=1}^{d_I} {}^d p_i \text{Im}[T({}^d\mathbf{n}_i(t))] - \text{Im}[T({}^d\mathbf{n}_e(t))] \right\}$$

Now separate the real components from the imaginary ones:

$$\text{Re}[{}^d\mathbf{E}(f, t; {}^d\mathbf{p})] = \sum_{i=1}^{d_I} {}^d p_i \text{Re}[T({}^d\mathbf{n}_i(t))] - \text{Re}[T({}^d\mathbf{n}_e(t))]$$

$$\text{Im}[{}^d\mathbf{E}(f, t; {}^d\mathbf{p})] = \sum_{i=1}^{d_I} {}^d p_i \text{Im}[T({}^d\mathbf{n}_i(t))] - \text{Im}[T({}^d\mathbf{n}_e(t))]$$

By defining the following equations and replacing them in the above, you can obtain a new formulation of ${}^d\mathbf{W}(f, t; {}^d\mathbf{p})$:

$$T_{\text{Re}}({}^d\mathbf{n}_i) = \text{Re}[T({}^d\mathbf{n}_i(t))] \quad T_{\text{Re}}({}^d\mathbf{n}_e) = \text{Re}[T({}^d\mathbf{n}_e(t))]$$

$$T_{\text{Im}}({}^d\mathbf{n}_i) = \text{Im}[T({}^d\mathbf{n}_i(t))] \quad T_{\text{Im}}({}^d\mathbf{n}_e) = \text{Im}[T({}^d\mathbf{n}_e(t))]$$

Introducing previous equations in ${}^d\mathbf{W}(f, t; {}^d\mathbf{p})$ it is easy to demonstrate that:

$$\begin{aligned}
{}^d\mathbf{W}(f, t; {}^d\mathbf{p}) = & \sum_{i=1}^{d_I} \left\{ {}^d p_i^2 \cdot (T_{Re} \circ^2({}^d \mathbf{n}_i) + T_{Im} \circ^2({}^d \mathbf{n}_i)) \right. \\
& - 2 {}^d p_i \cdot (T_{Re}({}^d \mathbf{n}_i) \circ T_{Re}({}^d \mathbf{n}_e) + T_{Im}({}^d \mathbf{n}_i) \circ T_{Im}({}^d \mathbf{n}_e)) \\
& \left. + \sum_{\substack{k=1 \\ \forall k \neq i}}^{d_I} [{}^d p_i {}^d p_k \cdot (T_{Re}({}^d \mathbf{n}_i) \circ T_{Re}({}^d \mathbf{n}_k) + T_{Im}({}^d \mathbf{n}_i) \circ T_{Im}({}^d \mathbf{n}_k))] \right\} \\
& + (T_{Re} \circ^2({}^d \mathbf{n}_e) + T_{Im} \circ^2({}^d \mathbf{n}_e))
\end{aligned}$$

The previous equation can be written in a simpler form by defining the following quantities, in which the symbol (\circ) denotes the Hadamard operator (i.e. Hadamard product, exponent, etc.):

$${}^d\mathbf{Q}_{ik}(f, t; {}^d\mathbf{p}) = T_{Re}({}^d \mathbf{n}_i) \circ T_{Re}({}^d \mathbf{n}_k) + T_{Im}({}^d \mathbf{n}_i) \circ T_{Im}({}^d \mathbf{n}_k)$$

$${}^d\mathbf{Q}_{ie}(f, t; {}^d\mathbf{p}) = T_{Re}({}^d \mathbf{n}_i) \circ T_{Re}({}^d \mathbf{n}_e) + T_{Im}({}^d \mathbf{n}_i) \circ T_{Im}({}^d \mathbf{n}_e)$$

A new formulation of ${}^d\mathbf{W}(f, t; {}^d\mathbf{p})$ it is therefore proposed:

$${}^d\mathbf{W}(f, t; {}^d\mathbf{p}) = \sum_{i=1}^{d_I} \left\{ {}^d p_i^2 {}^d\mathbf{Q}_{ii} - 2 {}^d p_i {}^d\mathbf{Q}_{ie} + \sum_{\substack{k=1 \\ \forall k \neq i}}^{d_I} [{}^d p_i {}^d p_k {}^d\mathbf{Q}_{ik}] \right\}$$

After a differentiation of the previous equation respect both ${}^d p_i$ that ${}^d p_k$, it is important to found the stationary points ${}^d_o\mathbf{p}$ of ${}^dW({}^d\mathbf{p})$, $\forall f, \forall t$.

The stationary points have global characteristics for ${}^d\mathbf{W}(f, t; {}^d\mathbf{p})$ because ${}^d\mathbf{H}$, which represents the Hessian matrix of ${}^dW({}^d\mathbf{p})$, $\forall f, \forall t$, is constant (and this comes from the quadratic form of ${}^d\mathbf{W}(f, t; {}^d\mathbf{p})$). In addition, being ${}^dH_{ik} = {}^dH_{ki}$, the Hessian matrix is symmetric and squared; thus, all its eigenvalues are strictly positive if its determinant is different from zero. It is possible to said that points, ${}^d_o\mathbf{p}$, $\forall f, \forall t$ are global minimum of ${}^d\mathbf{W}(f, t; {}^d\mathbf{p})$.

Clearly, the system of equations ${}^dW_i({}^d\mathbf{p}) = 0$ coincide to solve the following least-squares problem $\forall f, \forall t$, where ${}^d\mathbf{H}$ is symmetric and squared:

$${}^d\mathbf{H} {}^d\mathbf{p} = {}^d\mathbf{b} \quad \forall f, \forall t$$

Where ${}^d b_i = 2 {}^d Q_{ie}$. The problem above can be solved by inverting ${}^d \mathbf{H}$ if $\det({}^d \mathbf{H}) \neq 0$, and in this situation it is ensured that ${}^d \mathbf{p}, \forall f, \forall t$, represents the global minimum of ${}^d \mathbf{W}(f, t; {}^d \mathbf{p})$. For numerical reasons it is also possible to replace the inversion operation with the pseudo-inversion computed with the Singular Value Decomposition algorithm, that allow to reach a solution also in the case of conditioned Hessian matrices.

It is possible to derivate the following system, which provide the parameters of the expansion, ${}^d \mathbf{p}$, for each time:

$$\begin{cases} {}^d \mathbf{p} = {}^d \mathbf{H}^{-1} {}^d \mathbf{b} & \forall t \\ {}^d H_{ik} = 2 \int_0^t \left(\int_0^{f_s/2} {}^d \mathbf{Q}_{ik}(f, \tau; {}^d \mathbf{p}) df \right) d\tau \\ {}^d b_i = 2 \int_0^t \left(\int_0^{f_s/2} {}^d \mathbf{Q}_{ie}(f, \tau; {}^d \mathbf{p}) df \right) d\tau \end{cases}$$

Where f_s is the sampling frequency of the signal ${}^d \mathbf{n}_e(t)$. If the integral $\int_0^t (\cdot) d\tau$ is computed for $t = t_e$ where t_e is the length of the signal (in seconds) it is possible to get a constant value of ${}^d \mathbf{p}$ [32].

5.5.2. Modified Davidenkov

In this section it is introduced initially the original model and its formulation in stress terms, and after a modified version of the attritive Davidenkov law has been introduced to model the soil/raised ground floor dynamics.

Here the model is described in detail and a numerical example to demonstrate its effectiveness is reported for validation [33].

- **Original Model**

Davidenkov model proposes to provide a simple but robust formulation that uses only a small number of physically meaningful parameters. In particular, it proposes explicit formulas to capture different nonlinear hysteretic soil response including, especially, a constitutive model and backbone curve [4].

Preliminarily, it is necessary to start from the definition of the characteristics of the formulation of Davidenkov, which is presented, in tensional terms, in this way [4]:

$$\tau = G_{max} \cdot \left\{ \gamma - \text{sign}(\dot{\gamma}) \cdot \frac{\alpha}{n} \cdot [(\Delta\gamma + \text{sign}(\dot{\gamma}) \cdot \gamma)^n - 2^{n-1} \cdot (\Delta\gamma^n)] \right\}$$

Where:

- G_{\max} represents the shear modulus at very small deformation;
- γ is the shear strain;
- $\Delta\gamma$ is the amplitude of the cyclic shear strain;
- N is the exponent of the model order;
- α is a nonlinear parameter.

It has been chosen to use this formulation to study the non-linear hysteretic response of the soil because it correctly simulates the behaviour of materials consisting of particles, for example Rocks, sand and sediment, which have dynamic behaviors characterized by attritive interaction [4].

These Nonlinear macroscopic responses of soils are the consequence of complex friction mechanisms involving the contact between the grains and the rearrangement of the same as a result of load-unloading cycles.

Moreover, the variation of the damping ratio is the testimony of a dissipated energy that can be calculated through a hysteretic cycle of deformation.

This model, in fact, captures the dependence of the internal friction well with the amplitude of the stress.

However, since this model was formulated for laboratory tests, in which the signals exhibit a constant amplitude, the original formulation must be modified.

To take into account the variation in the amplitude of the seismic signal, and then to try to adhere to it as faithfully to the real case, it was decided to modify the original model.

- ***Modified model***

The modified model is a combination of a degrading nonlinear spring in parallel with a viscous term. The nonlinear degrading spring is in turn divided in a linear elastic degrading term and a non-linear elastic term [33].

So, the nonlinear elastic term, proportional to B , is represented by the backbone curve of the original Davidenkov model [33]. To overcome the elimination of the attritive hysteresis, after the modification involving the use of the backbone curve instead of the original law, a linear viscous term is introduced to capture the energy dissipation. In addition, the viscous term is required to model the rate-dependent nature of the soil. The model is reported hereinafter for a 1 DoF system:

$$F(t) = (A - AD\varepsilon(t))\mathbf{u}(t) + (B + BE\varepsilon(t))\text{sign}(\dot{\mathbf{u}}(t)) \left[2^{N-1}|\mathbf{u}(t)|^N - (|\mathbf{u}(t)| + \text{sign}(\dot{\mathbf{u}}(t))\mathbf{u}(t))^N \right] / N + C\dot{\mathbf{u}}(t)$$

Where A , B , C , D , and E are the model parameters. In particular:

- $A > 0$ is the linear elastic term;
- B regulates the type of nonlinearity;
- $C > 0$ is the viscous constant that regulates the energy dissipation;
- $D > 0$ is a degrading term for the linear elastic term, A ,
- E is a parameter that allows a change of the nonlinear behavior (softening/hardening).

The parameter B can be described by the following formulation:

$$B_1 = B_{0,1} + B_{0,1} \cdot E_1 \cdot \varepsilon(t)$$

When $E < 0$ the behavior imposed by B tend to be inverted, while for value of $E > 0$ the behavior, dictated by B , is accentuated.

Finally, N affect the global linearity of the force-displacement law. High values of N produce a linear law, while low values of N produce a rounding behaviour.

In particular, Figure 0.10 reports the model with $u(t) = 8 \cdot 10^{-4} \sin(2\pi t)$, $A=180e6$, $B=-666e8$, $C=5e6$, $D=3e-3$, $E=3e-3$ and $N=2$. Since $B < 0$, the system exhibits a hardening behavior.

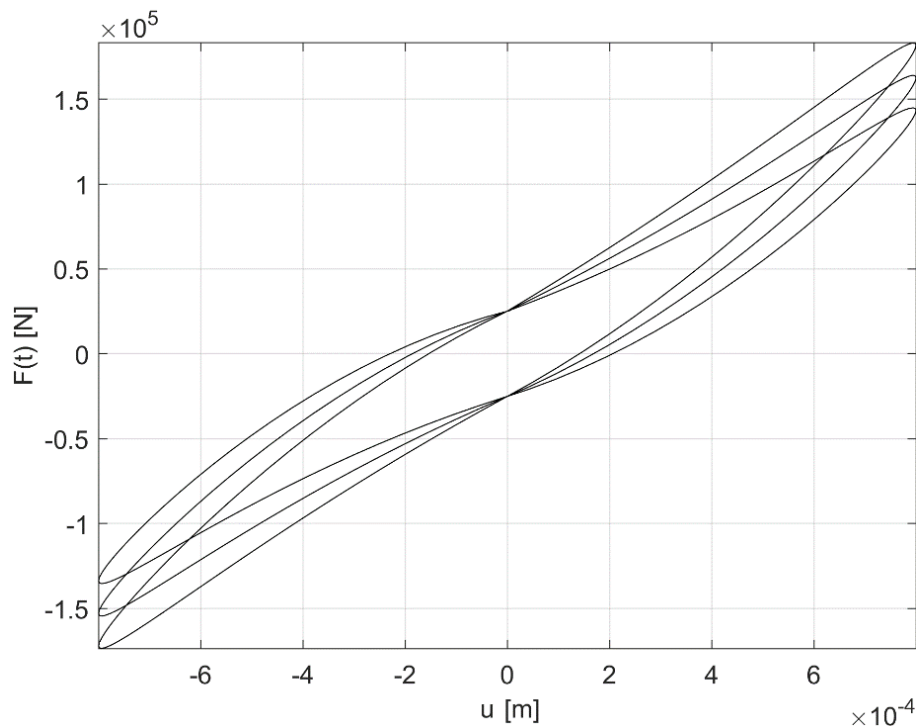


Figure 0.10: Modified Davidenkov model with hardening behavior ($B < 0$) [33].

In Figure 0.11, instead, the behavior of the system is softening because $B > 0$, in particular $B=666e8$.

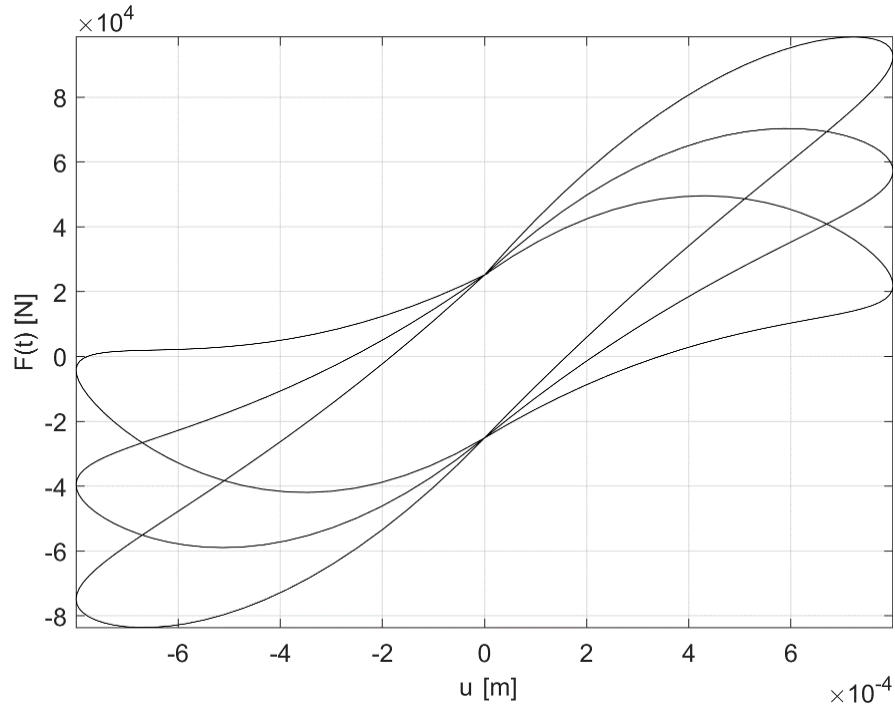


Figure 0.11: Modified Davidenkov model with softening behavior ($B>0$) [33].

5.5.3. Numerical model validation

In order to test the effectiveness of the model, a non-linear identification of a 1 DoF system simulated numerically is explored in this subsection.

The system is subjected to the Loma Prieta earthquake available in MatLab [34], rescaled to obtain a Peak Ground Acceleration (PGA) of 3.73 m/s². To simulate the presence of a low amount of noise, a zero mean random time history with amplitude equal to the 1% of the standard deviation of the original signals has been added, both to the input and output emulated channels.

The two added noises were supposed to be not correlated. The mass of the system was supposed to be known and equal to $M_e=1e4$ kg, while the initial stiffness was chosen to be $A_e0=1e7$ N/m. The damping ratio was assumed to be $\zeta=3\%$.

Defined the equation of motion, the procedure used to identify the law parameters of shear force in page 61, described in previous sub-chapter, has been applied. In this case $K_{0,jr}=K_{0,11}=A$. To simulate the occurrence of damage, the linear elastic stiffness term has been degraded using a Weibull type law assumed as:

$$A_e(t) = A_{e0}\{1 - R[1 - \exp(-(t/20)^{10})]\}$$

This ensuring a reduction of the stiffness, R , at about 15 s from the beginning of the earthquake. The equation of motion becomes:

$$M_e \ddot{\mathbf{u}}(t) + 2\zeta \sqrt{M_e A_e(t)} \dot{\mathbf{u}}(t) + A_e(t) \mathbf{u}(t) = -M_e \mathbf{a}_g(t)$$

In this equation, $\mathbf{a}_g(t)$ is the input ground motion, i.e. the rescaled Loma Prieta earthquake, while the remaining terms have been defined previously.

For the SFFT of the signal a 526 points periodic hamming window has been assumed. Then, to update the nonlinear parameters of the law, N , a hybrid particleswarm/patternsearch algorithm, [34], has been used, with lower and upper boundary on N of 1 and 10 respectively and starting value of 5.5.

Figure 5.12 reports the outcomes of the numerical validation for a reduction of the initial stiffness of 6%, ($R=0.06$). It is possible to note as the behavior of the single DoF system is captured very well both in time and frequency domain. As regard the prediction of the fictitious damage, a slightly difference is denoted in the natural frequency, f_n , reduction due to the stiffness degradation [33].

In Table 0.2 instead, the numerical values of the updated parameters are reported. The initial updated stiffness $A=1.0141e+07$, is very close to the value supposed, $Ae0=1.0000e7$, showing a normalized difference of about 1.41%. As regard the viscous term $C=1.8857e+04$, its value can be compared with the supposed initial value $=1.9107e+04$. Also in this case the normalized difference between the two values remains low, equal to -1.31% [33].

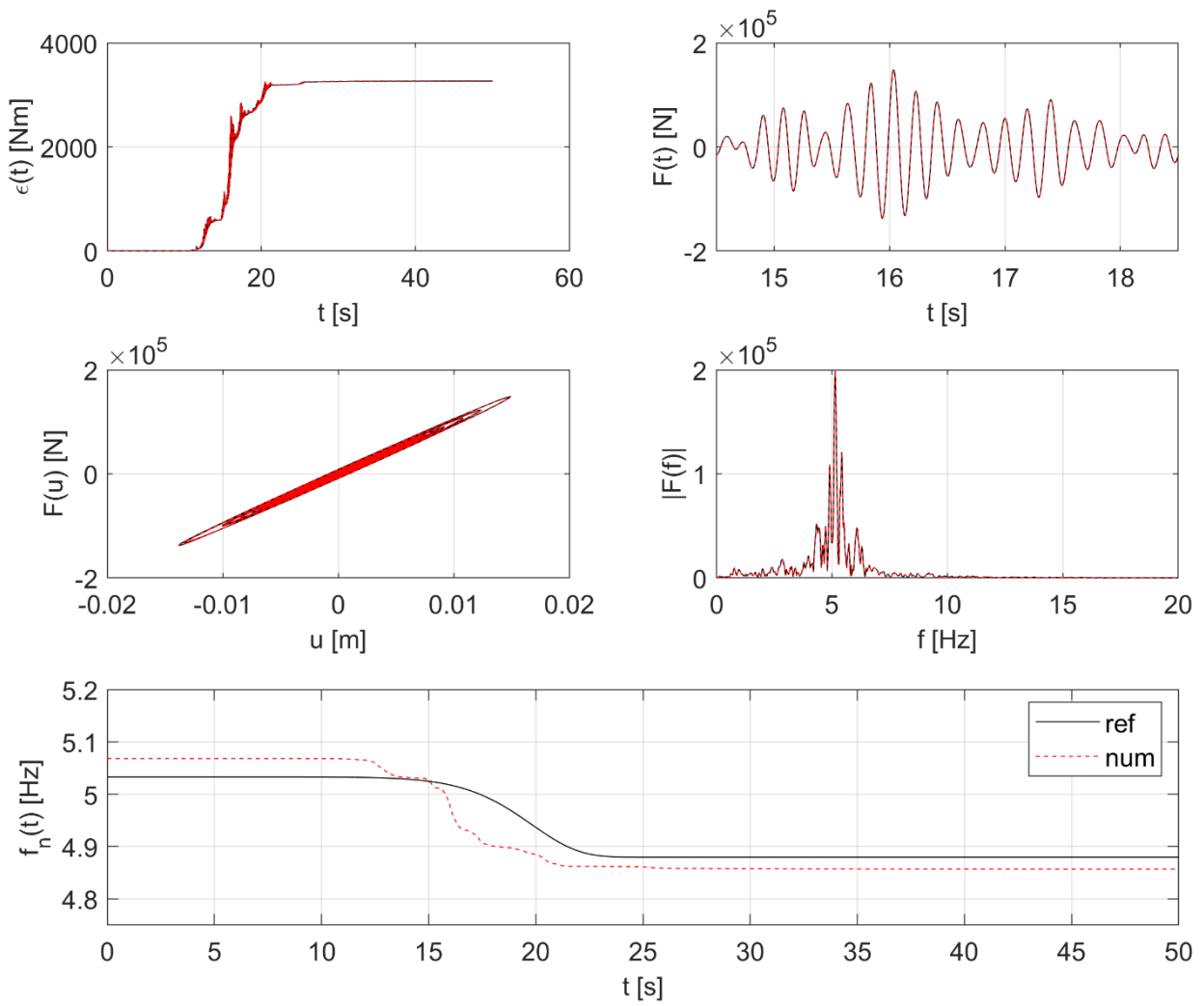


Figure 0.12: Results parameters of the numerical model [33].

A [N/m]	B [N/m ^N]	C [Ns/m]	D [-]	E [-]	N [-]
1.0141e+07	1.2310e+06	1.8857e+04	2.5007e-05	-0.0016	1.4867

Table 0.2: Updated parameters of the numerical model [33].

5.5.4. The 3 DoFs black-box model

The black box model is the result of the interaction between two different dynamic models, those of Bouc-Wen and the modified one by Davidenkov, so it is possible to study the behavior of a 3 DoF system.

The nonlinear part of the system is analysed now, in which the masses in play can be considered as series springs, which, in turn, may be analysed in parallel with respect to the linear part.

In this section, therefore, it will be a matter of analysing the forces affecting the system, i.e. the shear force on each floor, for the different formulations relating to the various degrees of freedom, since the modified formulation of Davidenkov, and for the other two that of Bouc-Wen. It proceeds to the fitting a system composed by springs and masses in series in which the applied forces are the shear acting on the individual planes and as displacement their relative displacements.

So, it is possible to write the following equation of the shear force that agent on each floor:

$$F_d = \sum_{i=d}^D f_i$$

Where:

- **F** represents the shear force on the individual plane,
- **f** the inter-storey forces;
- **D** The total number of "degree of freedom", three in the analyzed case.

The previous equation can be written for each floor and takes the following form:

$$F_1 = f_1 + f_2 + f_3;$$

$$F_2 = f_2 + f_3;$$

$$F_3 = f_3.$$

Initially it is necessary to start from the equation of motion and then to define the restoring force, so:

$$\mathbf{M}\ddot{\mathbf{u}} + \mathbf{f} = -\mathbf{M}\mathbf{a}_g$$

Since Bouc-Wen thinks in differential terms, it is necessary to derive the equation above, so you get:

$$\mathbf{M}\ddot{\mathbf{u}} + \dot{\mathbf{f}} = -\mathbf{M}\dot{\mathbf{a}}_g \mathbf{v}_t$$

Where \mathbf{v}_t represent the drag vector that in the case studied can be considered equal to $\mathbf{v}_t = \begin{Bmatrix} 1 \\ 1 \\ 1 \end{Bmatrix}$.

Having assumed a lumped mass system, thanks to which it is possible to consider the mass only concentrated on the slab of the relative plan, it is possible to decouple the system obtaining:

$$\mathbf{m}_d \cdot \ddot{\mathbf{u}}_d + \mathbf{f}_d = -\mathbf{m}_d \cdot \dot{\mathbf{a}}_g$$

With d that represents the i -th DoF of the black box system. Translate $\ddot{\mathbf{u}}_d$ a second member:

$$\dot{\mathbf{f}}_d = -\mathbf{m}_d \cdot (\ddot{\mathbf{u}}_d + \dot{\mathbf{a}}_g) = \mathbf{m}_d \cdot [-(\ddot{\mathbf{u}}_d + \dot{\mathbf{a}}_g)]$$

You can see how in the previous formula you have a derivate of the numerical restoring force on the left, and a known term right.

Assuming a lumped-mass model of the mass matrix, the restoring shear forces, $\mathbf{F}_d(t)$ for the assumed system take the following form:

$$\mathbf{F}_d(t) = \mathbf{F}_{d,L}(t) + \mathbf{F}_{d,NL}(t) = \sum_{j=d}^D m_j [-(\ddot{\mathbf{u}}_j(t) + \mathbf{a}_g(t))]$$

In the following section it is analysed the three different part that composed the restoring force formulation:

- **Linear part**

The linear elastic components of the shear force, $\mathbf{F}_{d,L}(t)$, are:

$$\mathbf{F}_{d,L}(t) = \sum_{j=d}^D \sum_{r=1}^D K_{jr} \mathbf{u}_r(t)$$

In which K_{jr} is a linear model parameter that represent the stiffness, and it is defined by:

$$K_{jr} = K_{0,jr} - K_{0,jr} \delta_{jr} \boldsymbol{\varepsilon}$$

In this equation $\boldsymbol{\varepsilon}$ represent an estimate of the total energy dissipated by the system during the seismic event.

$$\text{Being: } \varepsilon = \sum_{i=1}^D \int_0^t f_i \cdot \dot{u}_i dt = \int_0^t f_1 \cdot \dot{u}_1 dt + \int_0^t f_2 \cdot \dot{u}_2 dt + \int_0^t f_3 \cdot \dot{u}_3 dt$$

The stiffness matrix of the linear part is now reported, used in the formulation of the restoring force, it is chosen a generical model in which all spaces are full.

$$K = \begin{bmatrix} K_{11} & K_{12} & K_{13} \\ K_{21} & K_{22} & K_{23} \\ K_{31} & K_{32} & K_{33} \end{bmatrix}$$

For Betti theorem, in order to simplify our analysis, it is possible to consider symmetric stiffness matrix, in which $K_{12} = K_{21}$, $K_{13} = K_{31}$ and $K_{23} = K_{32}$.

- **Non linear part**

In this section will be introduced the nonlinear part of the analysis through hysteretic and degradating behaviour of the material.

Then, the nonlinear laws assumed to replicate the dynamic response of the system are reported and introduced in the identification framework.

Bouc-Wen

Replacing the formulation of the restoring force, for Bouc Wen is possible to write the following non linear part in general terms [1], [2], [3]:

$$\dot{f} = B \text{sign}(\dot{u} \cdot f) \cdot |f|^N \cdot \dot{u} + \gamma \cdot |f|^N \cdot \dot{u}$$

In general term:

$$\dot{f}_d = \beta_d \text{sign} \left[(\dot{u}_d - \dot{u}_{d-1}) \cdot \sum_{i=d}^D f_i \right] \cdot \left| \sum_{i=d}^D f_i \right|^{n_d} \cdot (\dot{u}_d - \dot{u}_{d-1}) - \gamma_i \cdot \left| \sum_{i=d}^D f_i \right|^{n_d} \cdot (\dot{u}_d - \dot{u}_{d-1}) - \sum_{i=d}^D f_{d+1,NL}$$

The following conditions are also introduced:

$$\dot{u}_0 = 0$$

$$\dot{f}_{D+1} = 0$$

3-rd Degree of Freedom

The following is the formulation of the shear force \dot{F}_3 , written in differential terms in relation to Bouc-Wen's law.

$$\dot{F}_3 = \dot{f}_3 = (k_{0,31} - k_{0,31}\delta_{31}\varepsilon) \cdot \dot{u}_1 + (k_{0,32} - k_{0,32}\delta_{32}\varepsilon) \cdot \dot{u}_2 + (k_{0,33} - k_{0,33}\delta_{33}\varepsilon) \cdot \dot{u}_3 - \beta_3 \cdot \text{sign}[(\dot{u}_3(t) - \dot{u}_2(t)) \cdot f_3] \cdot |f_3|^{n_3} \cdot (\dot{u}_3(t) - \dot{u}_2(t) - \gamma_3 \cdot |f_3|^{n_3} \cdot (\dot{u}_3(t) - \dot{u}_2(t)))$$

Only the nonlinear part is highlighted below:

$$\begin{aligned} \dot{F}_{3,NL}(t) = & -B_3 \text{sign}[(\dot{u}_3(t) - \dot{u}_2(t))F_3(t)] |F_3(t)|^{N_3} (\dot{u}_3(t) - \dot{u}_2(t)) \\ & - C_3 |F_3(t)|^{N_3} (\dot{u}_3(t) - \dot{u}_2(t)) \end{aligned}$$

The parameters that vary are now separated by constant parameters, in which ${}^d p_n$ and ${}^d n_n(t)$ are respectively the parameters that do not vary and those instead are the variable parameters:

$${}^3 F_n = \sum_n^3 {}^3 p_n {}^3 n_n(t)$$

In which the term n represent the numbers of the parameters.

So, for the 3-th DoF, the parameters are:

${}^3 p_n$	${}^3 n_n(t)$
$k_{0,31}$	\dot{u}_1
$k_{0,32}$	\dot{u}_2
$k_{0,33}$	\dot{u}_3
$k_{0,31}\delta_{31}$	$-\varepsilon\dot{u}_1$
$k_{0,32}\delta_{32}$	$-\varepsilon\dot{u}_2$
$k_{0,33}\delta_{33}$	$-\varepsilon\dot{u}_3$
β_3	$-\text{sign}[(\dot{u}_3(t) - \dot{u}_2(t)) \cdot f_3] \cdot f_3 ^{n_3} \cdot (\dot{u}_3(t) - \dot{u}_2(t))$
γ_3	$- f_3 ^{n_3} \cdot (\dot{u}_3(t) - \dot{u}_2(t))$

Table 0.3: Time dependent parameters ${}^3 n_n(t)$ and non Time dependent (${}^3 d_n$) for 3rd DoF.

It is important to say that the variables that depends on time are known, while the $^d p_n$ are the unknown of the problem.

2-nd Degree of Freedom

Being:

$$F_2 = f_2 + f_3; \text{ it is possible to write } \dot{f}_2 = \dot{F}_2 - \dot{f}_3$$

For the second shear force, is necessary to consider also the linear part of the third DoF. We now want to show that the linear elastic components of the other DoF do not come into play in the formulations of the DoF:

$$\begin{aligned} \dot{F}_2 = \dot{f}_2 + \dot{f}_3 = & (k_{0,21} - k_{0,21}\delta_{21}\varepsilon) \cdot \dot{u}_1 + (k_{0,22} - k_{0,22}\delta_{22}\varepsilon) \cdot \dot{u}_2 + (k_{0,23} - k_{0,23}\delta_{23}\varepsilon) \cdot \\ & \dot{u}_3 + (k_{0,31} - k_{0,31}\delta_{31}\varepsilon) \cdot \dot{u}_1 + (k_{0,32} - k_{0,32}\delta_{32}\varepsilon) \cdot \dot{u}_2 + (k_{0,33} - k_{0,33}\delta_{33}\varepsilon) \cdot \dot{u}_3 - \beta_2 \cdot \\ & \text{sign}[(\dot{u}_2 - \dot{u}_1) \cdot (f_2 + f_3)] \cdot |f_2 + f_3|^{n_2} \cdot (\dot{u}_2 - \dot{u}_1) - \gamma_2 \cdot |f_2 + f_3|^{n_2} \cdot (\dot{u}_2 - \dot{u}_1) - (k_{0,31} - \\ & k_{0,31}\delta_{31}\varepsilon) \cdot \dot{u}_1 - (k_{0,32} - k_{0,32}\delta_{32}\varepsilon) \cdot \dot{u}_2 - (k_{0,33} - k_{0,33}\delta_{33}\varepsilon) \cdot \dot{u}_3 + \beta_3 \cdot \text{sign}[(\dot{u}_3 - \dot{u}_2) \cdot \\ & f_3] \cdot |f_3|^{n_3} \cdot (\dot{u}_3 - \dot{u}_2) + \gamma_3 \cdot |f_3|^{n_3} \cdot (\dot{u}_3 - \dot{u}_2) = (k_{0,21} - k_{0,21}\delta_{21}\varepsilon) \cdot \dot{u}_1 + (k_{0,22} - \\ & k_{0,22}\delta_{22}\varepsilon) \cdot \dot{u}_2 + (k_{0,23} - k_{0,23}\delta_{23}\varepsilon) \cdot \dot{u}_3 - \beta_2 \cdot \text{sign}[(\dot{u}_2 - \dot{u}_1) \cdot (f_2 + f_3)] \cdot |f_2 + f_3|^{n_2} \cdot \\ & (\dot{u}_2 - \dot{u}_1) - \gamma_2 \cdot |f_2 + f_3|^{n_2} \cdot (\dot{u}_2 - \dot{u}_1) + \beta_3 \cdot \text{sign}[(\dot{u}_3 - \dot{u}_2) \cdot f_3] \cdot |f_3|^{n_3} \cdot (\dot{u}_3 - \dot{u}_2) + \gamma_3 \cdot \\ & |f_3|^{n_3} \cdot (\dot{u}_3 - \dot{u}_2) \end{aligned}$$

Only the nonlinear part is highlighted below:

$$\begin{aligned} \dot{F}_{2,NL}(t) = & -B_2 \text{sign}[(\dot{\mathbf{u}}_2(t) - \dot{\mathbf{u}}_1(t)) \mathbf{F}_2(t)] |\mathbf{F}_2(t)|^{N_2} (\dot{\mathbf{u}}_2(t) - \dot{\mathbf{u}}_1(t)) \\ & - C_2 |\mathbf{F}_2(t)|^{N_2} (\dot{\mathbf{u}}_2(t) - \dot{\mathbf{u}}_1(t)) \end{aligned}$$

Similar to before, we now proceed to identify the parameters dependent on time and those that remain unchanged. The following report is recalled:

$${}^2F_n = \sum_n^2 {}^2p_n \quad {}^2n_n(t)$$

Values of K_{32} e k_{23} , previously assessed for the analysis of the third DoF, not been reported as no longer used in the reduction base.

2p_n	${}^2n_n(t)$
$k_{0,21}$	\dot{u}_1
$k_{0,22}$	\dot{u}_2
$k_{0,21}\delta_{21}$	$-\varepsilon\dot{u}_1$
$k_{0,22}\delta_{22}$	$-\varepsilon\dot{u}_2$
β_2	$-\text{sign}[(\dot{u}_2 - \dot{u}_1) \cdot (f_2 + f_3)] \cdot f_2 + f_3 ^{n_2} \cdot (\dot{u}_2 - \dot{u}_1)$
γ_2	$- f_2 + f_3 ^{n_2} \cdot (\dot{u}_2 - \dot{u}_1)$

Table 0.4: Parametri che dipendono dal tempo ${}^2n_n(t)$ e quelli non (2d_n) per il secondo DoF.

By reusing the equation of motion and referring to what is mentioned above, we can rewrite the relationship of the restoring force:

$$f_d = \sum_n^d {}^d p_n {}^d n_n(t) \cong -\mathbf{m}_d \cdot \mathbf{g}_d = -\mathbf{m}_d \cdot (\ddot{\mathbf{u}}_d + \mathbf{a}_g)$$

With the equation above, then, we try to approximate the restoring force with the function g_d , which represents a polynomial expansion.

At this point, it is necessary to introduce what you will go to insert inside of Matlab: in this regard, we will create matrices in such a way as to determine the parameters unknown that, in our case, are the values of the coefficients $n_1 n_2 n_3$ of the two different dynamic models.

The previously written report can be rewritten in matrix terms:

$$\mathbf{N}_j \mathbf{p}_j = -\mathbf{M} \mathbf{g}_d$$

In which j thus represents the j -th parameter considered. You can now introduce the following matrices \mathbf{N}_j , \mathbf{P}_j e $[\mathbf{M}^* \mathbf{a}_g]$ which have respectively the size of $[8 \times 8]$, $[8 \times 1]$ and $[3 \times 1]$.

Having the matrix $\mathbf{M} \mathbf{g}_d$ the size of a $[3 \times 1]$, you must use a Short Fourier Transform of the signal to calculate the Time-Frequency distribution (referred to in chapter 5.5.1) and, as a result, calculate the evolution of model parameters over time.

To do this you use the function “*Dirpest*” of Matlab, which takes into input both the parameters referred to n_i , which will be the ones that multiply the functions in the expansion and are known values, both the parameters referred to n_e , which have experimental origin and are those related to the previous g_d .

In particular, n_i is the matrix of the total “numerical” jerk approximated by a Bouc-Wen oscillator, having as lines the number of time step and as columns the number of parameters;

\mathbf{n}_e , instead, is a vector of the total “experimental” jerk having dimension equal to numbers of time step as lines and one column. The aim is to calculate \mathbf{n}_i and \mathbf{n}_e for any DoF. It is important to introduce also the sampling frequency, in Hz, and the length of the signals, in second, and so you can determine the values ${}^d p_n$ using the function:

$$p(\text{end}, :) = \mathbf{dirpest}(n_i, n_e, f_s, t_e, 1, \text{windo})$$

At this point, is possible to specify what is necessary to write as code for the **third** and second DoF:

$$\begin{aligned} {}^3 n_i(:,1) &= v_1 \\ {}^3 n_i(:,2) &= -v_1 * \varepsilon \\ {}^3 n_i(:,3) &= v_2 \\ {}^3 n_i(:,4) &= -v_2 * \varepsilon \\ {}^3 n_i(:,5) &= v_3 \\ {}^3 n_i(:,6) &= v_3 * \varepsilon \\ {}^3 n_i(:,7) &= \\ & -\text{sign}[(\dot{u}_3(t) - \dot{u}_2(t)) \cdot f_3] \cdot |f_3|^{n_3} \cdot (\dot{u}_3(t) - \dot{u}_2(t)) \\ {}^3 n_i(:,8) &= \\ & -|f_3|^{n_3} \cdot (\dot{u}_3(t) - \dot{u}_2(t)) \\ {}^3 n_e &= m_3 * g_{d3} = -m_3 * (a_3 + a_g) \end{aligned}$$

The parameters ${}^d p_n$ that could be determined by the previous function are now reported:

- $k_{0,31} = p(:,1)$, con $K_{0,31}=K_{0,13}$;
- $\delta_{31} = p(:,2)/p(:,1)$, con $\delta_{31} = \delta_{13}$;
- $k_{0,32} = p(:,3)$, con $K_{0,32}=K_{0,23}$;
- $\delta_{32} = p(:,4)/p(:,3)$, con $\delta_{32} = \delta_{23}$;
- $k_{0,33} = p(:,5)$;
- $\delta_{33} = p(:,6)/p(:,5)$;
- $\beta_3 = p(:,7)$;
- $\gamma_3 = p(:,8)$.

Thanks to this, it is possible to find the calibration parameter N_3 .

For the **second** DoF, the values of n_i and n_e are:

$${}^2 n_i(:,1) = v_1$$

$${}^2n_i(:,2) = -v_1 * \varepsilon$$

$${}^2n_i(:,3) = v_2$$

$${}^2n_i(:,4) = -v_2 * \varepsilon$$

$${}^2n_i(:,5) =$$

$$-sign[(\dot{u}_2 - \dot{u}_1) \cdot (f_2 + f_3)] \cdot |f_2 + f_3|^{n_2} \cdot (\dot{u}_2 - \dot{u}_1)$$

$${}^2n_i(:,6) =$$

$$-|f_2 + f_3|^{n_2} \cdot (\dot{u}_2 - \dot{u}_1)$$

In this case, as you are already aware of the values of K_{23} , K_{31} , K_{32} e K_{33} , the value of 2n_e can be written such as ${}^2n_e = F_{d2} - (K_{23} \cdot v_3 + K_{32} \cdot v_2 + K_{31} \cdot v_1)$.

In the same way as before, the parameters 2p_n are reported:

- $k_{0,21} = p(:,1)$, con $K_{0,21} = K_{0,12}$;
- $\delta_{21} = p(:,2)/p(:,1)$, con $\delta_{21} = \delta_{12}$;
- $k_{0,22} = p(:,3)$;
- $\delta_{22} = p(:,4)/p(:,3)$;
- $\beta_2 = p(:,5)$;
- $\gamma_2 = p(:,6)$.

Thanks to this, it is possible to find the calibration parameter N_2 .

It is important to emphasize that the parameters N_2 and N_3 characteristic of Bouc Wen more have a high value and more the non-linearity is accentuated: a value of N low corresponds almost to a linearity, for a value that tends to infinity we have instead a perfect elasto plastic behavior.

Modified Davidenkov

Here is reported the equation of the nonlinear part used:

$$\mathbf{F}_{1,NL}(t) = B_1 sign(\dot{\mathbf{u}}_1(t)) [2^{N_1-1} |\mathbf{u}_1(t)|^{N_1} - (|\mathbf{u}_1(t)| + sign(\dot{\mathbf{u}}_1(t)) \mathbf{u}_1(t))^{N_1}] / N_1 + C_1 \dot{\mathbf{u}}_1(t)$$

$$B_1 = B_{0,1} + B_{0,1} E_1 \varepsilon(t)$$

Similar to Bouc-Wen, the variables dependent on time and the parameters, through the following report, are now differentiated:

$${}^1F_n = \sum_n^1 {}^1p_n {}^1n_n(t)$$

As before, you separate time-dependent terms from those not for the first DoF.

1p_n	${}^1n_n(t)$
$k_{0,11}$	u_1
$k_{0,12}$	u_2
$k_{0,13}$	u_3
$k_{0,11}\delta_{11}$	$-\varepsilon u_1$
$k_{0,22}\delta_{22}$	$-\varepsilon u_2$
$k_{0,23}\delta_{23}$	$-\varepsilon u_3$
B_1	$sign(\dot{\mathbf{u}}_1(t)) [2^{N_1-1} \mathbf{u}_1(t) ^{N_1} - (\mathbf{u}_1(t) + sign(\dot{\mathbf{u}}_1(t))\mathbf{u}_1(t))^{N_1}]/N_1$
C_1	$\dot{\mathbf{u}}_1(t)$

Table 0.5: Time-dependent parameters ${}^1n_n(t)$ and non 1d_n for the first DoF.

At this point, is possible to specify what is necessary to write as code for the **first** DoF:

$$\begin{aligned} {}^1ni(:,1) &= u_1 \\ {}^1ni(:,2) &= -u_1 * \varepsilon \\ {}^1ni(:,3) &= u_2 \\ {}^1ni(:,4) &= -u_2 * \varepsilon \\ {}^1ni(:,5) &= v_1 \end{aligned}$$

As you are aware of all the stiffness values, except K_{11} , 1n_e can be written as:

$${}^1n_e = F_1 - (K_{12} \cdot u_2 + K_{13} \cdot u_3 + K_{21} \cdot u_1 + K_{22} \cdot u_2 + K_{23} \cdot u_3 + K_{31} \cdot u_1 + K_{32} \cdot u_2 + K_{33} \cdot u_3)$$

In the same way as before, the parameters ${}^d p_n$ are reported:

- $k_{0,11} = p(:,1)$,
- $\delta_{11} = p(:,2)/p(:,1)$;
- $B_1 = p(:,3)$;
- $E_1 = p(:,4)/p(:,3)$;
- $C_1 = p(:,5)$.

Contrary to what is said for parameters N_2 and N_3 To Bouc Wen, a high value of N_1 corresponds to a linearity.

Following all the formulations introduced, it was thus able to determine the parameters of the constitutive models adopted.

5.6. Final model

In this section will then explain the final model obtained, remembering to be a simplified model represented by a 3 DoF system: the first of which is constituted, as previously said, by the ground and the mass of the raised plane; the second and third are made up of the second and third floors respectively.

In accordance with the constitutive laws adopted, therefore, following a mass-spring equivalent schematization, the model will be obtained in Figure 0.13.

The linear elastic part consists of a stiffness matrix *Full* having as its terms the values of k_{11} , k_{22} , k_{33} , K_{12} , K_{23} e K_{13} and, always for Betti's theorem, the following relationships apply $K_{12} = K_{21}$, $K_{23} = K_{32}$.

Being Bouc-Wen rate independent, it can be noted that for the second and third DoF there is no viscous term and there is no degradation, whereas, instead, it is present in the first degree of freedom (ruled by Davidenkov) through the term viscous *C*. It is useful to emphasize that the curved springs represent non-linear chain-like interplane springs, while the bars represent a variation of stiffness over time. Finally, the double bars for the first DoF are characteristic of a variation of linearity from softening to hardening.

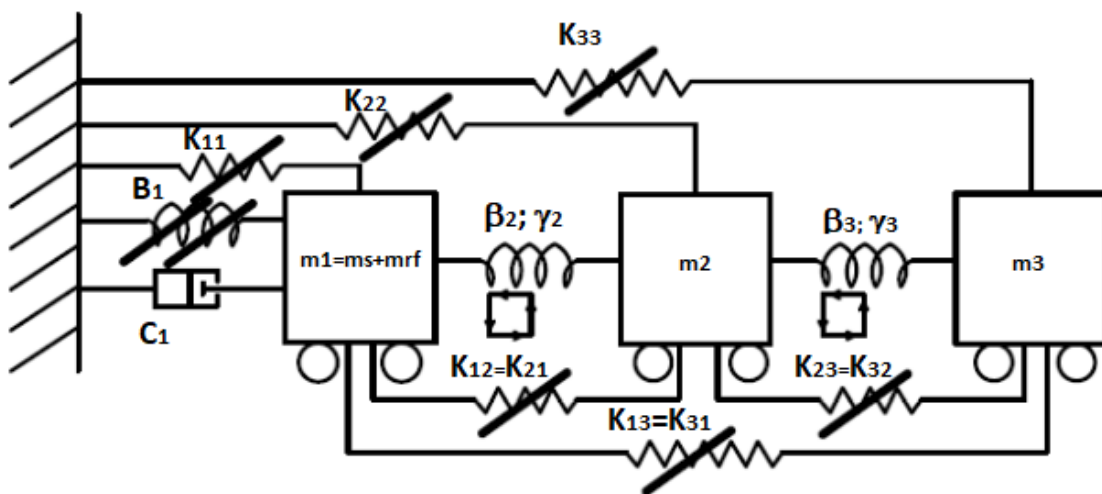


Figure 0.13: The final Model used in the analysis.

Thanks to the definition of these features of the model taken, now you are in possession of all tools aimed at solving the equations previously reported.

6. Application

In this section the soil-structure interaction problem is initially analyzed in order to estimate the mass of the soil that participates to the dynamics of the soil-structure system by using a finite element (FE) model.

First, we will be introduced the model and its characteristics thanks to which it was possible carry out the calibration of the mass, specifying, in particular, stratigraphic data and assumptions used.

Then the input signals will be deconvoluted at the depth identified as $Z_0 = 18$ m, will be introduced into the equation of motion as a known term $g_d = -m_d \cdot (u(t) + a(t))$.

Thanks to the knowledge of the experimental data, the signals of input agents on the structure and those transed through deconvolution following the passage inside the ground, one could switch to the calibration of the parameters of the two dynamic models considered.

6.1. Calibration of the soil-mass

In order to define a reduced model of the soil-structure system, a linear elastic FE model of the soil has been constructed. The model counts about 97382 nodes with 3 DoFs (X,Y,Z) each one. Moreover, it is consider an 8 nodes brick element with an average dimension of 0.80 m, that has been used to model the linear elastic behavior of the soil.

It thus started from a geometry which has the following coordinates, with origin fixed in the first point (Table 0.1):

p.ti	x_{in} [m]	y_{in} [m]
1	0	0
2	40	0
3	40	12
4	26	25
5	15	25
6	0	12

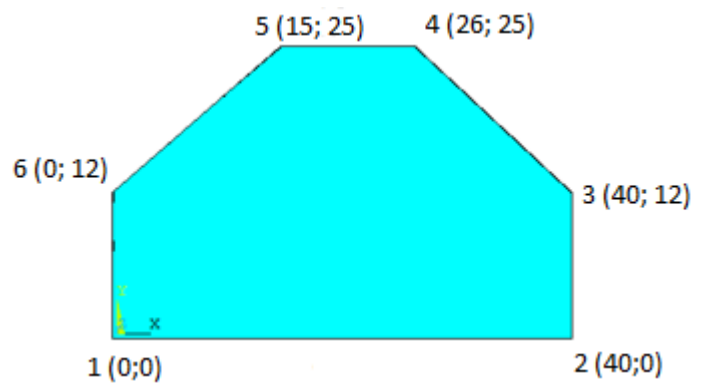


Table 0.1: Initial coordinates of plan geometry before sensitivity analysis.

6.1.1. Sensitivity analysis

It was then necessary to carry out a sensitivity analysis, in such a way as to understand which was the parameter which most influenced the analysis and the identification of the participant mass. Consequently going to change the size of the cluster of soil respectively in the X and Y direction, it was found that it is possible to increase only by 0.5, This value was considered in

a way that would take into account an external boundary slightly larger than the size of the structure. As a result of the considerations made, the size of the hexagon in plan assume the following coordinates (Table 0.2):

p.ti	x_{in} [m]	y_{in} [m]	Δx	Δy	x_{fin} [m]	y_{fin} [m]
1	0	0	-0.5	-0.5	-0.5	-0.5
2	40	0	0.5	-0.5	40.5	-0.5
3	40	12	0.5	0.5	40.5	12.5
4	26	25	0.5	0.5	26.5	25.5
5	15	25	-0.5	0.5	14.5	25.5
6	0	12	-0.5	0.5	-0.5	12.5

Table 0.2: Coordinates of the geometry in the plant with which the sensitivity analysis was carried out.

After this, because the availability of the only first experimental natural frequency of the soil, a sensitivity analysis for the other parameters has been performed to assess the variability that each parameter of the model has on the first numerical frequency. The parameters, P , accounted for the sensitivity analysis reports the experimental values of the soil parameters. For this analysis, it is taken in account also the variability of the vertical dimension z (varying its values between 0-40 m) and the shear modulus G (varying their values between 1/10 and 10 times its experimental value for each layers).

In addition, to ensure that the dimensions along the X-direction were correct, the horizontal parameter was also introduced L , causing it to vary between 0-10 m (e.g: the bottom dimension of the model in Table 0.1 b becomes 41 m + 2L during the sensitivity analysis).

Being the first fundamental frequency of the system equal to 3.64 Hz, we proceeded with the sensitivity analysis in such a way to derive a combination of parameters so that it was possible to obtain, through analysis by FEM model, the numerical value obtained through an experimental campaign.

Figure 0.1 reports the results of the sensitivity analysis, where $f_{1,i}$ indicates the first numerical frequency, while $\sigma(f_1,i)$ denotes the standard deviation of the f_1 with respect to the i -th parameter that are reported in the legend.

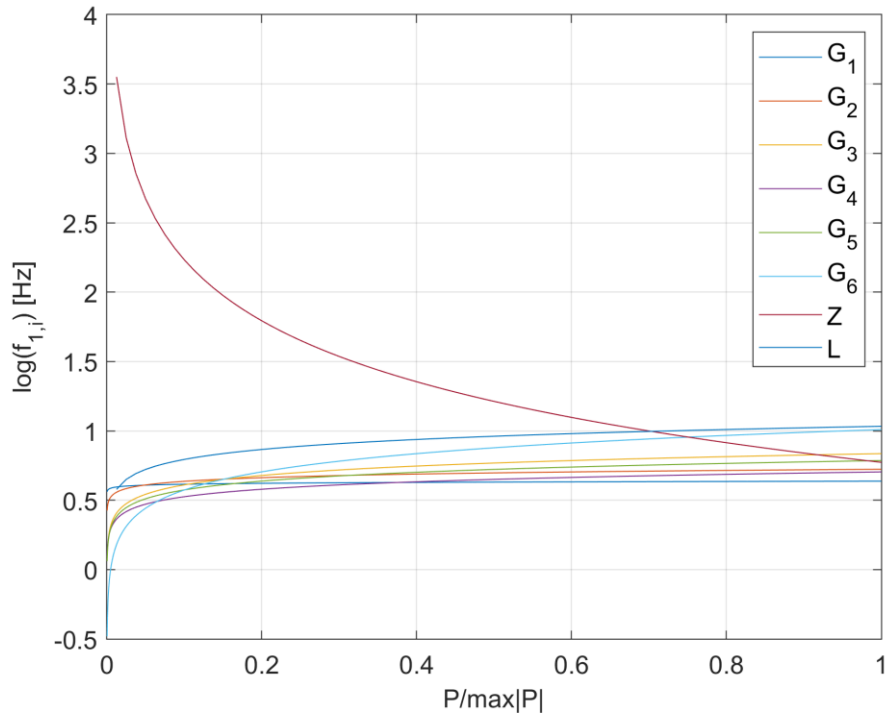


Figure 0.1: Sensitivity analysis: variation of the first frequency with the parameters.

It is can easily see how the parameter Z refers to the depth is the one with a greater variation than the other parameters.

What is said is confirmation in the following Figure 0.2, in which is possible to see that the depth of the model, $P_7=Z$, cause the 80.5 % of the total variability of f_1 .

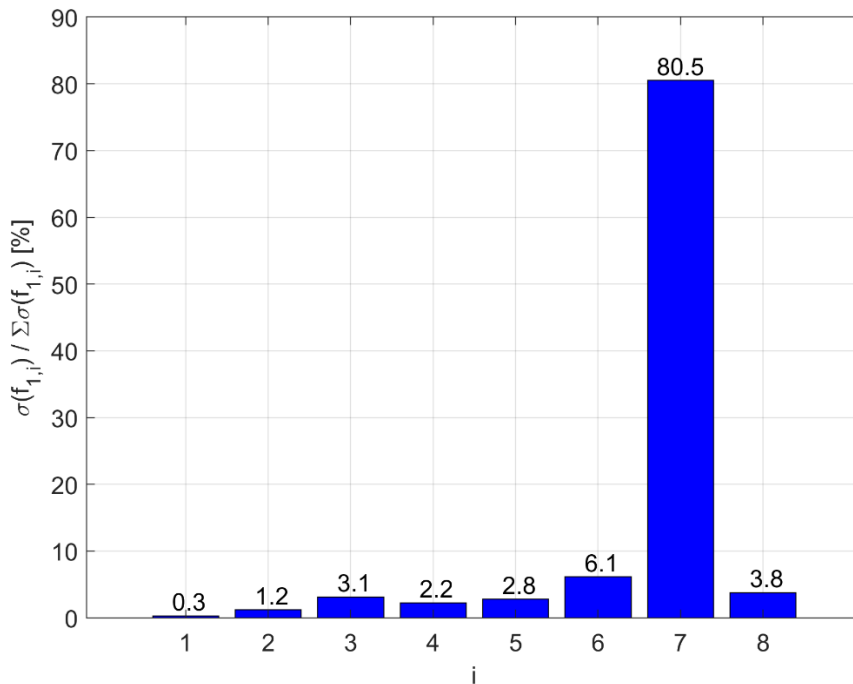


Figure 0.2: Sensitivity analysis: percentage of the total variability of the first natural frequency carried by each model parameter.

With the 3.8 % of variability of the f_1 there is the parameter $P_8=L$, which testifies to the importance of recruitment, in both directions (x and z), with regard to the geometry of the model.

The analysis carried out on the parameters linked to the mechanical characteristics of the soil, with particular reference to the values of the sixth and third layers, $P_6= G_6$ and $P_3= G_3$, highlighted a participation in the variation of f_1 equal to 6.1 and 3.1% of the total, respectively. Then, in decreasing order of variability one have: G_5, G_4, G_2, G_1 , with respectively 2.8, 2.2, 1.2 e 0.3 % of total variability.

Following the results depicted in Figure 0.2, a slight unexpected behavior is denoted for the 3rd layer that bring more variability than the 4th and 5th layers.

This behaviour is probably due to greater thickness of the third layer and for the composition of the fourth layer, which has a velocity of the shear waves V_s and shear strength modulus equal to 683 m/s and 999e6 Pa respectively, considerably higher than those of the third layer. Summarizing the results obtained from the analysis, it can be said that, due to the high variability carried by Z , the updating of the FE model contemplated this parameter, while the other parameters are fixed to the experimental values.

Being available the experimental natural frequency of the ground, it is now possible to calibrate the ground mass going to modify the depth of the ground in order to obtain the same value of the experimental datum.

6.1.2. Geometry of the model

As mentioned previously in chapter 5, it was decided to hypothesize a surface of ground breaking in the shape of a hexagon, in such a way that it tried to retrace the T-inverse form of the School of Visso, thus considering the participation of the triangular zones immediately adjacent to the structure.

With the sensitivity analysis, it was shown that the parameter that most influenced the analysis was Z , the other parameters, however, were assumed to be equal to the values of the experimental data, while the L value was assumed equal to 0 (i.e. the dimensions of the FE model of the soil approximate the external dimensions of the building).

In Figure 0.3 It is thus reported the geometry in plan of the solid of ground obtained following the assumptions made, in which one specifies the relative lengths for each side.

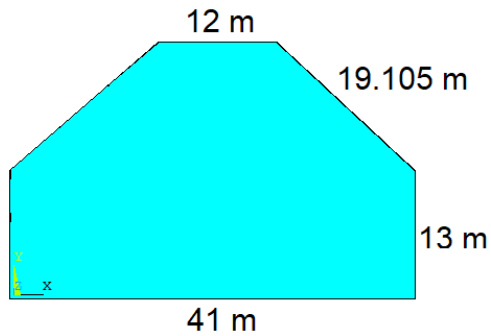


Figure 0.3: Plan geometry of the soil.

We now proceed to the description of the model of the ground solid used for the calibration of the soil mass:

- **Boundary conditions**

The model at the base of the solid was fully restrained thanks to the introduction of external hinges in order to prevent the presence of displacement.

For the vertical faces, it is chosen to leave these faces free because it was considered that the ground with mediocre consistency and therefore with low stiffness.

On the upper surface, moreover, it was decided not to affix any constraint, thus leaving the surface free.

Following calibration, in order to obtain the experimentally evaluated fundamental frequency, the boundary conditions have been modified and, as a result, the previously described condition has been applied to different volumes of soil, starting from that to greater depth, until a conformation is achieved thanks to which the desired frequency has been found.

- **Mesh**

What about the Mesh, it is chosen to attribute to the soil the property of **“solid”**, and, following the assignment of the properties to each individual layer, a regular mesh has been attributed for each element of the model, having a **Linsize** equal to **0.8**.

It was decided to use a regular mesh as there was no need to investigate and obtain particular information for a specific portion of soil.

In Figure 0.4 the complete model is shown, highlighting the final geometry of the 3D solid, the characteristics of the boundary conditions and the type of mesh used.

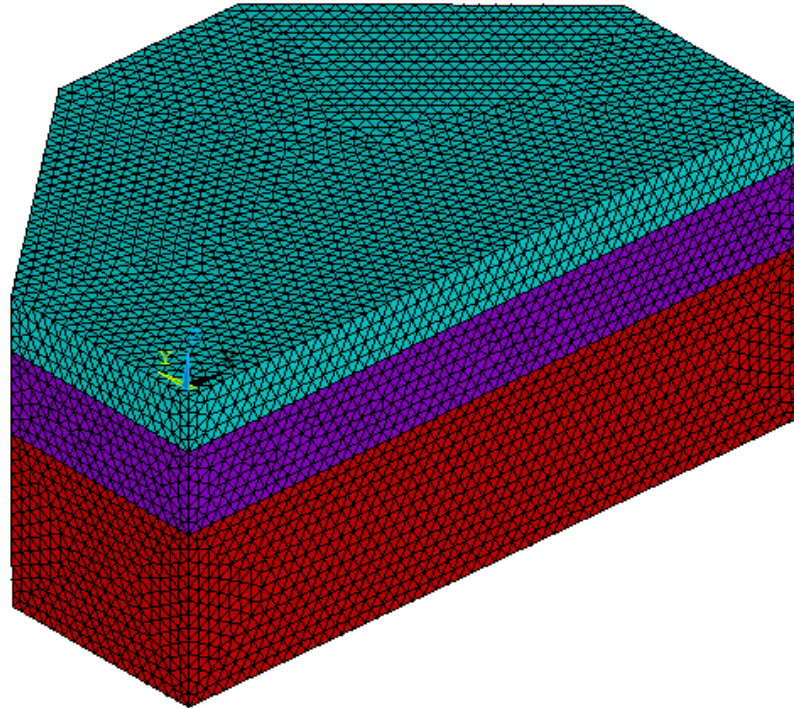


Figure 0.4: Solid model for soil calibration.

- **Stratigraphy**

Thanks to the knowledge of the experimental data coming from seismic test with single station, of which to the chapter 5, it was possible to specify within the model the stratigraphic composition adopted, with the attribution for each single layer of the parameters mechanical, such as elastic modulus E , Poisson's ratio ν and density γ , both geometric parameters, such as the thickness of each layer, to the depth of the bedrock.

The relationship with which the elastic module has been obtained and for each layer from the tangential module is reported for completeness:

$$E_i = 2 \cdot G_i \cdot (1 + \nu_i)$$

In the following Table 0.3 the values of the mechanical and geometric parameters used are therefore reported.

Mechanical parameters of model			
Layer	γ [Kg/m ³]	ν [-]	E [MPa]
1	2000	0.4	106.4
2	2000	0.4	291.2
3	2100	0.3	816.4
4	2100	0.3	2597.4
5	2000	0.4	1428
6	2100	0.3	2017.6

Geometric parameter of model	
Layer	$z_{i,max}$ [m]
1	3.2
2	4.8
3	10
4	8
5	4
6	10

Table 0.3: Mechanical and geometric parameters that are introduced in FE model.

In Figure 0.5 is reported the FE model taken with the relative stratigraphy, in which the thickness of each single layer is highlighted.

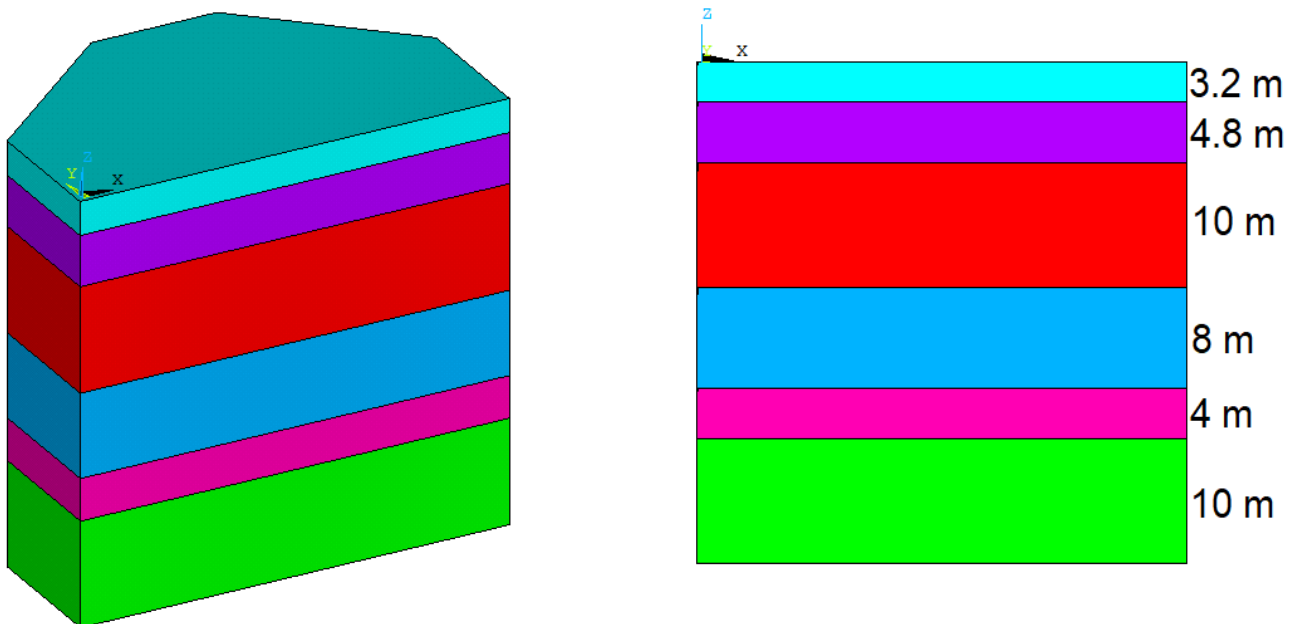


Figure 0.5: FE model of the soil.

Thus, having introduced the geometry, boundary conditions and mesh, it is now possible to perform the analyses to determine the portion of mass that participates dynamically with the structure during the seismic event considered.

6.1.3. Results after calibration

After the calibration, the optimal value of the depth of the restraint was found to be $Z_o = 18$ m, i.e. the depth of the third layer of the starting FE model.

In Table 0.4 reports the initial and updated values of the parameter Z and the numerical frequencies.

Configuration	z [m]	f ₁ [Hz]	f ₂ [Hz]	f ₃ [Hz]
Initial	40	1.81	2.27	2.85
Updated	18	3.64	3.90	4.24

Table 0.4: Initial and updated value of Z , f_1 , f_2 and f_3 .

Following the calibration of the model, the previous numerical frequencies have been identified; specifically, the frequency f_1 represents, as already mentioned, the fundamental frequency of the ground used for the calibration, the f_2 represents the frequency in X-direction, and f_3 is the frequency referred to the modal form of rotational type.

It is important to note in the previous table how the frequency obtained by numerical analysis with an FE model corresponds to the experimental one obtained by passive seismic test performed on site.

Starting from the new depth of the model, Z_0 , it was possible to calculate the mass of the soil that hypothetically participates to the dynamics of the soil-structure system: It has proven to be the mass of the first three layers, e risulta essere pari a **$m_s=32467500$** kg.

Following an eigen analysis carried out on the calibrated solid previously described, in subsequent Figure 0.6, Figure 0.7, Figure 0.8 instead, is reported the first 3 numerical modes of the updated FE model.

The first modal shape is characterized by pure translation along Y, the second one highlights a predominant component along the X-direction with rotating components, and finally the third shows a purely rotational form.

STEP=1
SUB =1
FREQ=3.64113

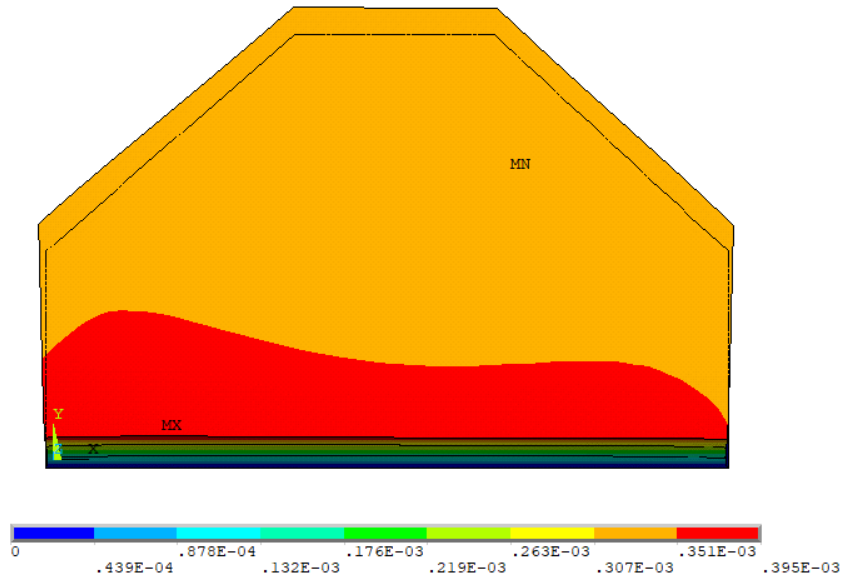


Figure 0.6: First modal shape after calibration of the soil-mass.

STEP=1
SUB =2
FREQ=3.90021

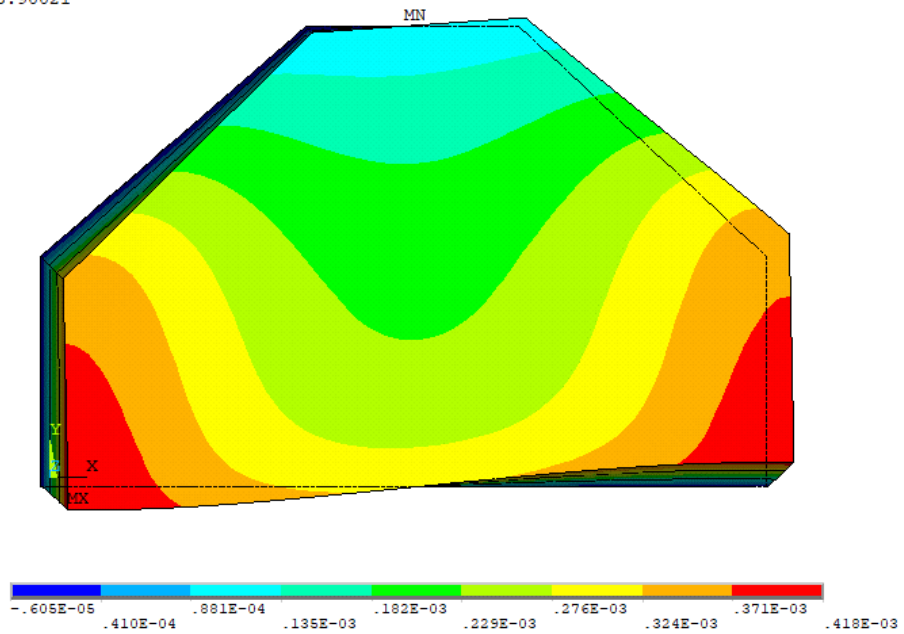


Figure 0.7: Second modal shape after calibration of the soil-mass.

STEP=1
SUB =3
FREQ=4.23558

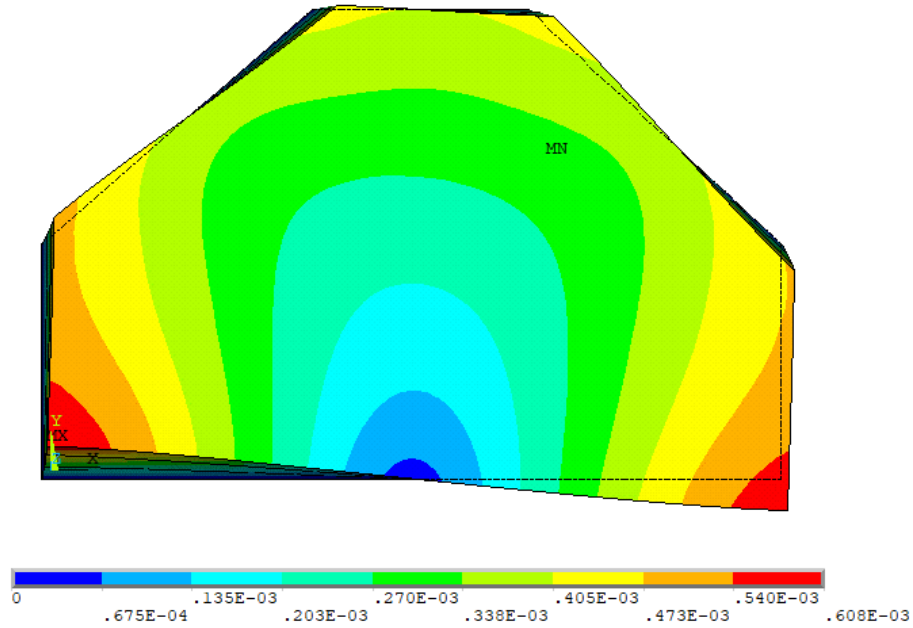


Figure 0.8: Third modal shape after calibration of the soil-mass.

6.1.4. Depth validation in third layer correspondence

Having determined the amount of participant mass, we now want to try to find a geomechanical justification to the fact that the experimental frequency of 3.64 Hz was found by considering a FE model up to the depth of $Z_0 = 18$ m.

In this regard, the contrast of impedance present between the various layers and between the layers and the bedrock is analysed in this paragraph. The formulations used respectively for the first and the second case are reported:

$$I_{C,i} = \sqrt{\frac{\rho_{i+1} \cdot V_{s,i+1}}{\rho_i \cdot V_{s,i}}} \quad I_{C,B} = \sqrt{\frac{\rho_B \cdot V_{s,B}}{\rho_i \cdot V_{s,i}}}$$

In which i represents the i -th layer of the ground and the index goes from 1 to 6 with step 1, while $\rho_{S+1} = \rho_B$ e $V_{s,i+1} = V_{s,B}$ denote the density and the shear wave velocity of the bedrock.

In the following Table 0.5 the values of the impedance ratios calculated by the different formulations are reported:

$I_{c,i}$ [-]	$I_{c,B}$ [-]
1.29	3.24
1.33	2.52
1.34	1.89
0.91	1.41
1.03	1.54
1.50	1.50

Table 0.5: Values of impedance contrast in relation to each layer and bedrock.

It is possible to graph the values shown above in the following graphs:

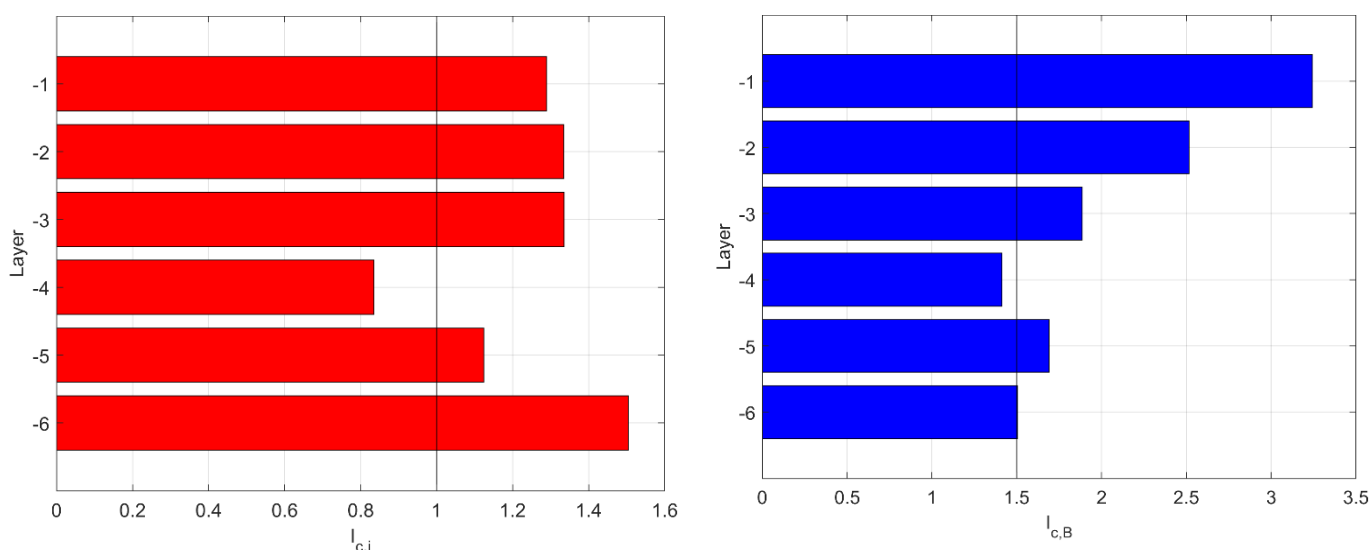


Figure 0.9: a) interlayer contrast of impedance; b) bedrock contrast of impedance

The graph on the left (in red) represents the impedance contrast between the different layers of the model, while the one on the right (in blue) the contrast that the various layers have in reference to the bedrock. From Figure 6.9 it is possible to see that the interlayer contrast of impedance attributed at layer 4 is minor that 1, denoting inversion of the wave due to the presence of a layer with an high dynamical stiffness if compared to the neighboring layers.

Although the third and fourth layers are both made of gravelly sand, layer 3 has a velocity V_s Equal to 383 m/s, while the fourth is decidedly higher than 683 m/s; similarly, the tangential module G also suffers a significant increase, passing from 314 MPa of the third layer to 999 MPa of the fourth [17].

The above mentioned values of the V_s And of module G, and normally, one would expect a reversal of the waves in correspondence of layers with soils having different particle size composition, with particular reference for example to layer 4, consisting of gravelly sand and for which with a composition coarse granulometric, and for example at Layer 5, consisting of clayey silt with a fine particle size.

In addition, from the same figure, it is possible to note that the interlayer contrast decreases up to the 4th layer, then its value remains approximately constant for the 3rd, 2nd and 1st layers. Instead, in Figure 6b, the bedrock contrast of impedance helps to visualize how the shear waves amplify with respect to the waves coming from the bedrock. From this figure one can easily denote as the contrast is almost constant under the 4th layer (indeed, it could be interpolated by a parabolic function), while a high, linear, increase of the bedrock contrast is found starting from the 3rd layer up to the surface. This could explain a high participation of the first three layers of soil in the dynamics of the soil-structure system.

6.2. Ground motion deconvolution

In order to use the software "Strata" [31], it is necessary to know the parameters of the various soil layers, in particular the speed of the shear waves V_s , the shear resistance module G and the decay curves of the shear and damping module.

Being now aware of the stratigraphic profile of the soil and the physical-mechanical properties of each layer (determined in Chapter 5.2.), it is possible to import on the software all the information necessary for the reconstruction of the accelerograms to variation of the passage within the soil depot.

6.2.1. "General setting"

The parameters of input needed to perform the analysis through the software in this section are clarified. Specifically, therefore, it is necessary to define initially the *Linear Equivalent method* (previously analyzed in chapter 5.4.3.) and then define the "Time Series" approach. To complete the General Setting operating framework, in addition it is necessary to define the tolerance error and the number of maximum iterations that the software must make before reaching convergence; the first sets the difference, in terms of shear modulus or damping ratio, to which the method is assumed to converge, while the latter represents the number of iterations required for the program for equivalent Visco-elastic analysis. These values were taken from 0.5% and 30 iterations, respectively.

It is more important to specify the role of the actual stress shear ratio, which represents the proportion of the maximum deformation actually considered. Would typically assume equal to 0.65, otherwise it may be defined by the following equation:

$$SSR = \frac{M - 1}{10}$$

The value of M represents the magnitude of the seismic event of 26-10-2016 amounted to 5.4, for which it was inserted within the software the value 0.44.

When the programme transposes an accelerogram to assess the behaviour of the soil, it loses its validity taking the maximum shaking value and, following the analysis, the maximum

deformation value: this is because these values are meaningful only for a limited moment of time.

As a result, you need to find a portion of the maximum deformation value, equal to $\gamma_{eff} = SSR \cdot \gamma_{max}$, and more representative of soil behavior.

6.2.2. Soil types

One of the most important and commonly encountered problems in geotechnical earthquake engineering is the evaluation of ground response parameters. Much progress has been made in the development of analytical procedures for evaluating the response of soil deposits in seismic loading conditions. Successful application of such procedures for determining ground response in specific cases, however, is essentially dependant on the incorporation of representative soil properties in the analyses. For accurate computation of ground response problems, accurate information about dynamic shear modulus and damping ratio value is required, which are incorporated through shear modulus and damping curves.

Following this, having previously found that the layer of soil was composed of clayey silt, limosa clay and gravelly sand, it is now necessary to assign the corresponding specific weight and above all the correct statistical distribution of nonlinear properties that best approximate the behavior of each material.

In particular, it has been chosen to use for the layers of clayey silt and sand gravelly distributions present in the literature, such as Vucetic & Dobry respectively with average plasticity index equal to 15 for the silt clay and Seed & Idriss (also with medium plasticity index) for gravelly sand.

- **Vucetic & Dobry**

Vucetic and Dobry (1991) presented a parametric study showing the influence of the plasticity index on the seismic response of clay sites excited by the accelerations recorded on rock in Mexico City during the 1985 earthquake [35].

Based on the review of a number of available cyclic loading results, they concluded that the plasticity index (PI) is the main factor controlling the locations of the modulus reduction curve G/G_{max} versus γ_c (cyclic shear strain) and material damping ratio curve λ versus γ_c , for a wide variety of saturated soils ranging from clays to sands [35].

In Figure 0.10 the trend of G/G_{Max} ratio and damping ratio D are reported to the increase deformation level for the formulation proposed by Vucetic & Dobry.

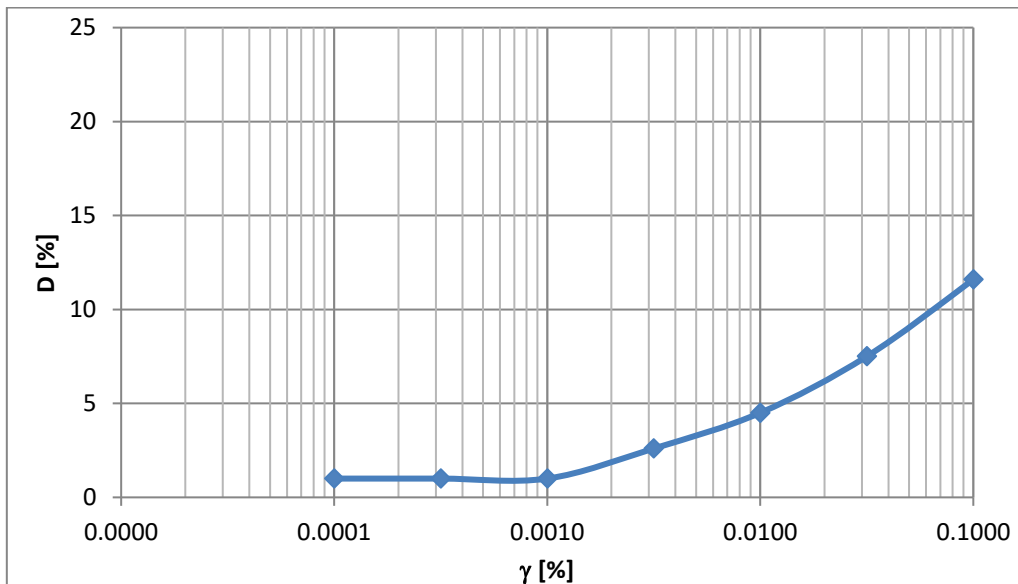
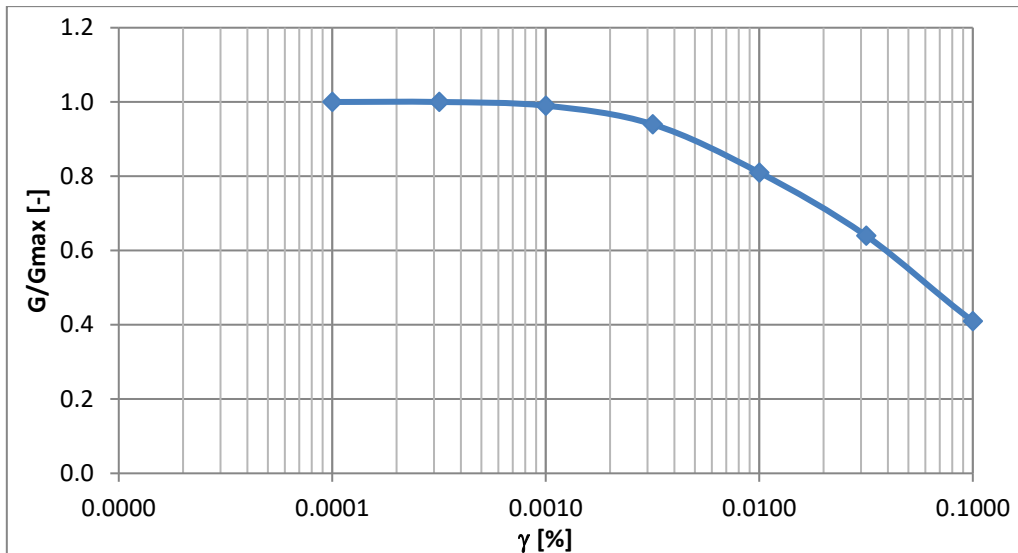


Figure 0.10: Trend of G/G_{max} and D to varying deformation level for Vucetic & Dobry formulation.

- **Seed & Idriss**

Many experimental investigations for sandy soils have been carried out and formulated for general use by Seed and Idriss (1970), Hardin and Drnevich (1972), Seed et al (1986), Kokusho (1980). Seed and Idriss (1984) reviewed a number of studies and found that in general, the shear modulus values of sands are strongly influenced by effective confining pressure, strain amplitude and void ratio but not significantly by variation in grain size characteristics [35]. As before, in Figure 0.11 the trend of G/G_{Max} ratio and damping ratio D are reported to the increase deformation level for the formulation proposed by Seed & Idriss.

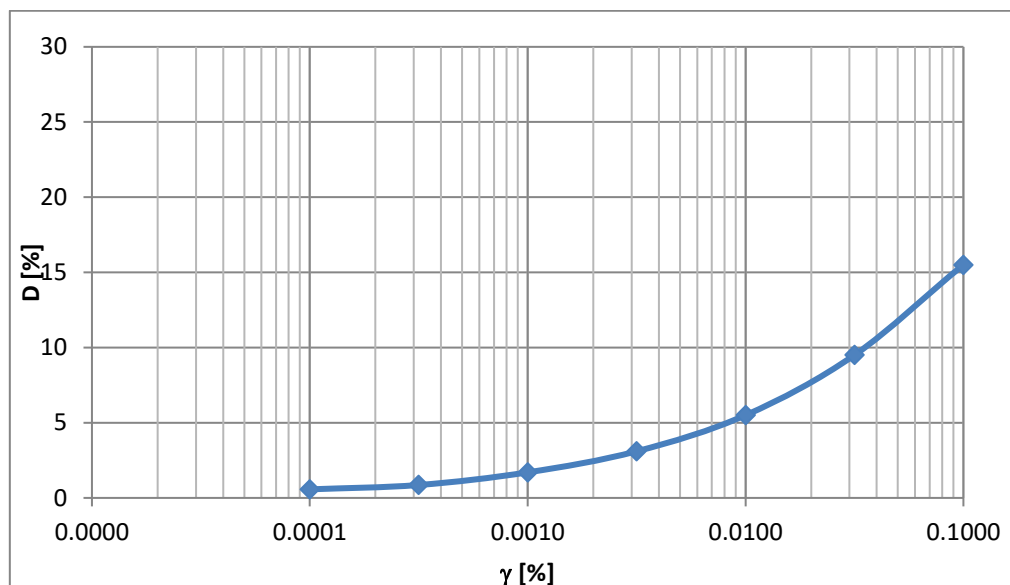
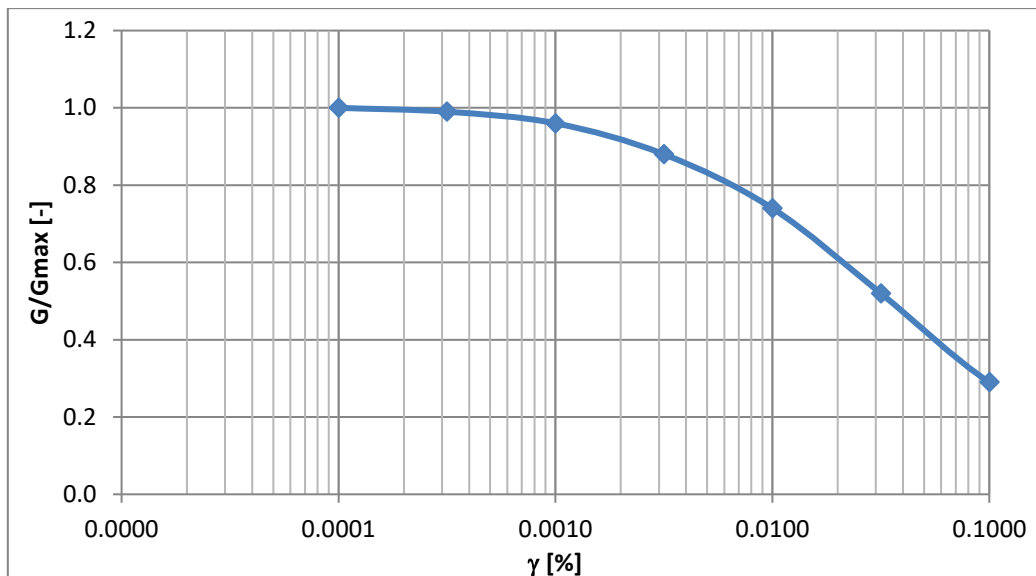


Figure 0.11: Trend of G/G_{max} and D to varying deformative level for Seed & Idriss formulation.

- **Rollins**

As the sand layer consisted of a larger particle size component, i.e. gravel, it was thought could be useful also the curves of Rollins.

Rollins (1998) studied results available from at least 15 investigations where cyclic shear tests were performed on gravels to determine shear modulus and damping relationships presented in literature. He summarized the available data, presented best-fit curves for shear modulus and damping relationships, and reviewed factors which affect these parameters [35]. He concluded that best-fit hyperbolic curve can be used to define the mean normalized shear modulus, G/G_{max} , versus cyclic shear strain, γ , curve for gravels based on data from the 15

investigators. The mean curve for gravels is closer to the curve for sand determined by Seed and Idriss (1970) than the curve for gravels reported by Seed et al (1986). He analysed 980 data points from 15 investigations and suggested that the G/G_{max} versus γ curve is essentially independent of sample disturbance, fines content (range 0-9%), gravel content, and relative density. It is, however, moderately dependent on the confining pressure [35].

The formulation of G/G_0 and D are following reported:

$$\frac{G}{G_0} = \frac{1}{[1 + 20\gamma (1 + 10^{(-10\gamma)})]}$$

$$D = 0.8 + 18(1 + 0.15\gamma^{-0.9})^{-0.75}$$

However, in the course of the analysis, it was decided to use the formulations used by Seed & Idriss; Rollins Curves are reported equally (Figure 0.12) as an example at varying levels of the deformative level:

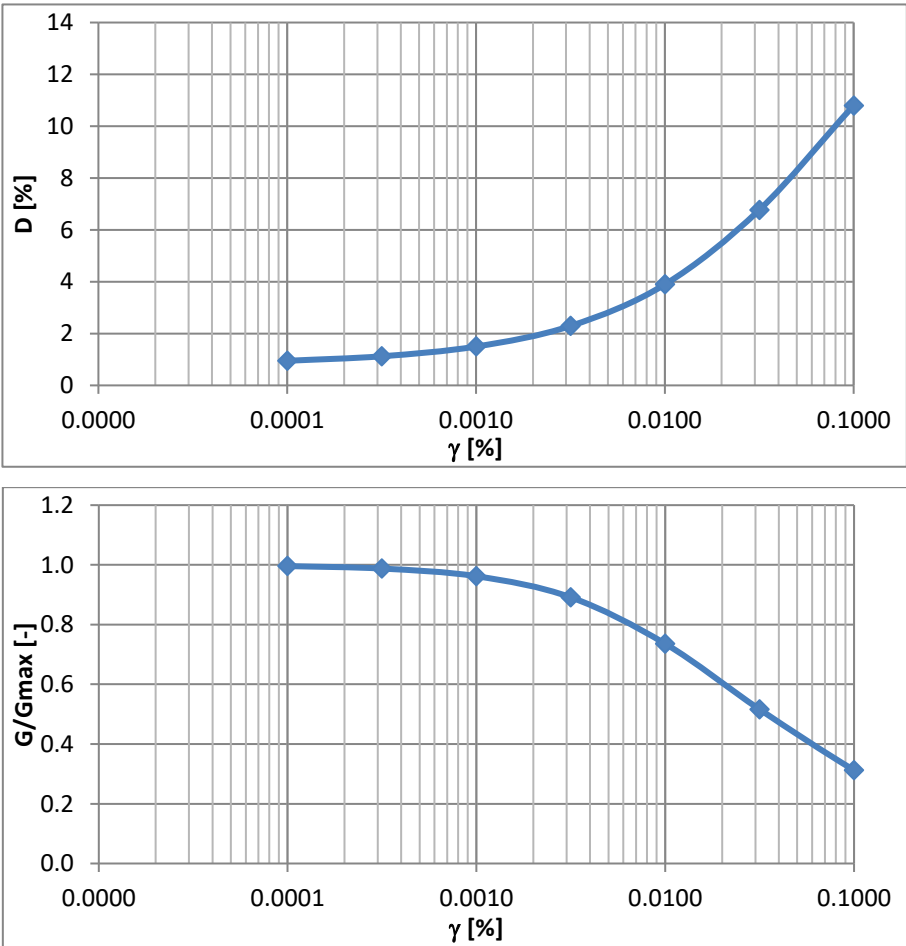


Figure 0.12: Trend of G/G_{max} and D to varying deformative level for Rollins formulation.

6.2.3. Soil discretization

In this section you will perform the discretization of the stratigraphic profile of the volume of soil considered; performing this operation in the most efficient way possible means reducing and almost cancelling problems due to resonance.

Discretize the profile with layers too thick would mean losing much of the information because, being the dynamic response of the terrain assessed in the middle of the layer, it would take values of unrepresentative deformations of the real state deformative possibly present, risk of considering values even close to zero; discretized in a more detailed way, instead, you can better reconstruct the information about the behavior of the soil.

The stratigraphy of the soil was so modified to avoid problems due to resonance, so the layers had to be divided into substrates in such a way that the Wave length λ is always greater than the thickness of the layer.

Specifically, remembering that the first resonance frequency of the ground is $f_0 = \frac{V_S}{4 \cdot h}$, and being the $\lambda = V_S/f = 4h$, the thickness of the layer must be less than $\lambda / 4$; If not, however, for $h = \lambda / 4$, it is in the resonance condition.

As the transfer function H, referred to in Chapter 5.4., defined as the ratio between the amplitude of the motion on the surface and that in the underlying layer, if I had exactly one layer of thickness $h = \lambda / 4$, the amplitude of motion in the underlying layer would be equal to 0, and consequently the transfer function would tend to infinity.

As a result of said, we can therefore define the new minimum thickness with the the following relationship, in which 25 Hz is a reference frequency:

$$H_{min,i-strato} < \frac{\lambda_{min}}{4} = \frac{V_S}{4 \cdot 25 \text{ Hz}}$$

This passage has been carried out in such a way as to prevent the seismic harmonics from resonating and to prevent the software is not be able to go to convergence near such frequencies. It is reported below in Table 0.6 the complete discretization of the soil model up to the depth of 40 meters, in which the thickness of the new layers is highlighted, the type of soil and the relative velocity V_S .

Sub-layers	Depth [m]	Thickness [m]	Soil type	V_S [m/s]
1	0.00	1.00	Clay silt	136
2	1.00	1.00	Clay silt	136
3	2.00	1.20	Clay silt	136
4	3.20	0.80	Clay silt	136
5	4.00	1.00	Silty clay	226
6	5.00	1.00	Silty clay	226
7	6.00	1.00	Silty clay	226

8	7.00	1.00	Silty clay	226
9	8.00	1.00	Gravel sand	383
10	9.00	1.00	Gravel sand	383
11	10.00	1.00	Gravel sand	383
12	11.00	1.00	Gravel sand	383
13	12.00	1.00	Gravel sand	383
14	13.00	1.00	Gravel sand	383
15	14.00	1.00	Gravel sand	383
16	15.00	1.00	Gravel sand	383
17	16.00	1.00	Gravel sand	383
18	17.00	1.00	Gravel sand	383
19	18.00	1.00	Gravel sand	683
20	19.00	1.00	Gravel sand	683
21	20.00	1.00	Gravel sand	683
22	21.00	1.00	Gravel sand	683
23	22.00	1.00	Gravel sand	683
24	23.00	1.00	Gravel sand	683
25	24.00	1.00	Gravel sand	683
26	25.00	1.00	Gravel sand	683
27	26.00	1.00	Clay silt	500
28	27.00	1.00	Clay silt	500
29	28.00	1.00	Clay silt	500
30	29.00	1.00	Clay silt	500
31	30.00	1.00	Gravel sand	602
32	31.00	1.00	Gravel sand	602
33	32.00	1.00	Gravel sand	602
34	33.00	1.00	Gravel sand	602
35	34.00	1.00	Gravel sand	602
36	35.00	1.00	Gravel sand	602
37	36.00	1.00	Gravel sand	602
38	37.00	1.00	Gravel sand	602
39	38.00	1.00	Gravel sand	602
40	39.00	1.00	Gravel sand	602
41	40.00	Half space	Bedrock	1300

Table 0.6: Discretization of stratigraphic model.

6.2.4. Results after deconvolution

As a result of the said, Figure 0.13 shows the accelerogram registered at the basement of the structure by channel 21, while in Figure 0.13 (b) the accelerogram is reported following the deconvolution process at a depth of 18 m.

For the analysis, the new input used for the analysis of the ground structure interaction will be the deconvoluted accelerogram at 18m.

It can see how the passage within the soil deposit changes the amplitude of the seismic motion.

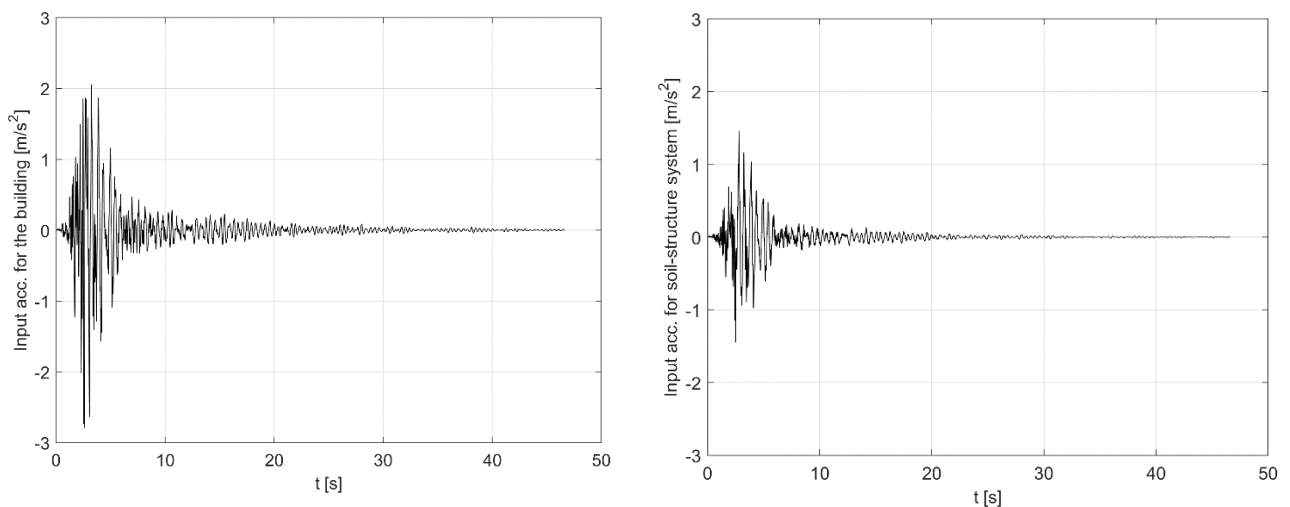


Figure 0.13: Seismic input for the building or output for the soil-structure system at channel 21 (a), seismic input for the soil structure system (b)

6.2.4. Data filtering

In order to know the values of the accelerograms at 18 meters of depth necessary to calibrate the parameters of the two dynamic models considered, it is necessary to filter the signals recorded by the base triad (channels 21, 22 and 23) and by the other biaxial channels.

To do this, initially need to define the sampling rate f_s , equal to 250 Hz, and a sampling time t_s , equal to $1/f_s = 0.004$ S.

The data was filtered from 0.5 to 20 Hz because the frequency content of the quake is usually included in these frequencies and, specifically, filters were used to 0.5 to correct baseline errors or low frequency errors, while above 20 Hz, in which there are mainly frequencies linked to a noise component, are not interested in the study as it is difficult to make a quake can present similar value.

Specifically, a Butterworth filter was used. To Determine the filter order, we used the following MATLAB-implemented function: **buttord** (*w_p*, *w_s*, *R_p*, *R_s*) .

Input parameters are therefore:

- *W_p*: Passband corner (cutoff) frequency, specified as a scalar or a two-element vector with values between 0 and 1, with 1 corresponding to the normalized Nyquist frequency, π rad/sample.
- *W_s*: Stopband corner frequency, specified as a scalar or a two-element vector with values between 0 and 1, with 1 corresponding to the normalized Nyquist frequency, π rad/sample.
- *R_p*: Passband ripple, specified as a scalar expressed in dB.
- *R_s*: Stopband attenuation, specified as a scalar expressed in dB.

These values assumed for the case study: $W_p = [0.5 \ 20]/(f_s/2)$; $W_s = [0.5/1.25 \ 20*1.25]/(f_s/2)$; $R_p = 3$ to ensure $W_n = W_s$; $R_s = 8$ to ensure the stability in the pole-zero circle with minimum order [36].

Once the acceleration values were filtered, it was possible to determine the corresponding velocity and displacement values through the function “**cumtrapz**”.

The function `cumtrapz(X,Y)` integrates Y with respect to the coordinates or scalar spacing specified by X. In our case we used: $v = cumtrapz(t, acc)$ e $u = cumtrapz(t, v)$. [36]

6.3. Resolution of equations

6.3.1. Determination of masses refers to 2-nd and 3-rd Degree of Freedom

Having the finite element model available for the school under study, obtained for the drafting of another elaborate, it was possible to know the masses inherent to the second and third floors. To introduce the masses the main features are reported with which the structure has been modeled of the school through the use of the Ansys software: As far as the horizontal and vertical elements were concerned, it is used “*Shell*” elements, which are suitable for the analysis of structures with thin or relatively thick shells and is characterized by four nodes with six degrees of freedom for each node as translations in the X, Y, and Z directions and rotations around the X, Y, and Z axes, both for linear analyses including large rotations and/or large deformation. Element “*Shell*” is following represented on (Figure 0.14).

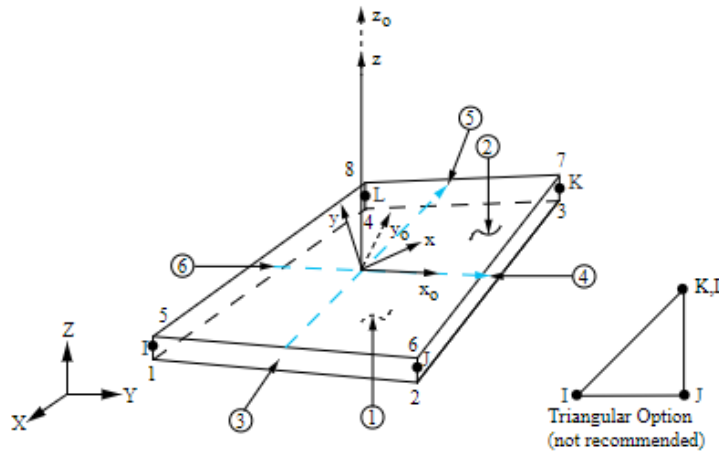


Figure 0.14: Modeling a "Shell" element within the FE software.

To simulate the ground of coating were used spring elements, elements one-dimensional simulating the behavior of Winkler Springs; they are suitable for longitudinal or torsional analysis and can cover the role of shock absorbers by longitudinal springs exploiting monoaxial compression-tension with three degrees of freedom for each node. It also covers the role of torsional spring damper, also with three degrees of freedom on each node (rotations around the nodal axes X, Y and Z).

The said is shown in the following Figure 0.15.

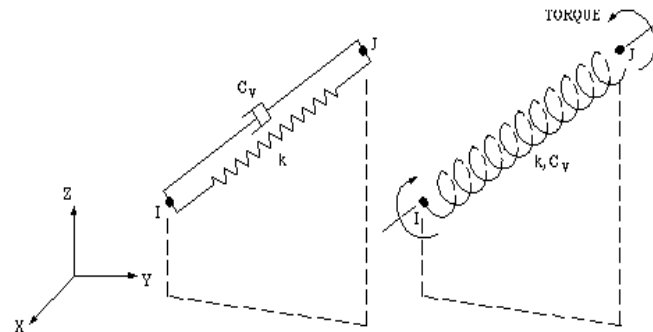


Figure 0.15: Modeling of a "Combin" element within the FE software.

Having data from a double screw jack test, they have been assigned to the structural elements and not the following mechanical properties: Compression resistance f_m , Shear strength τ_0 , elastic modulus E, shear module G, specific weight W and finally, to simulate the ground, stiffness representing the springs inserted.

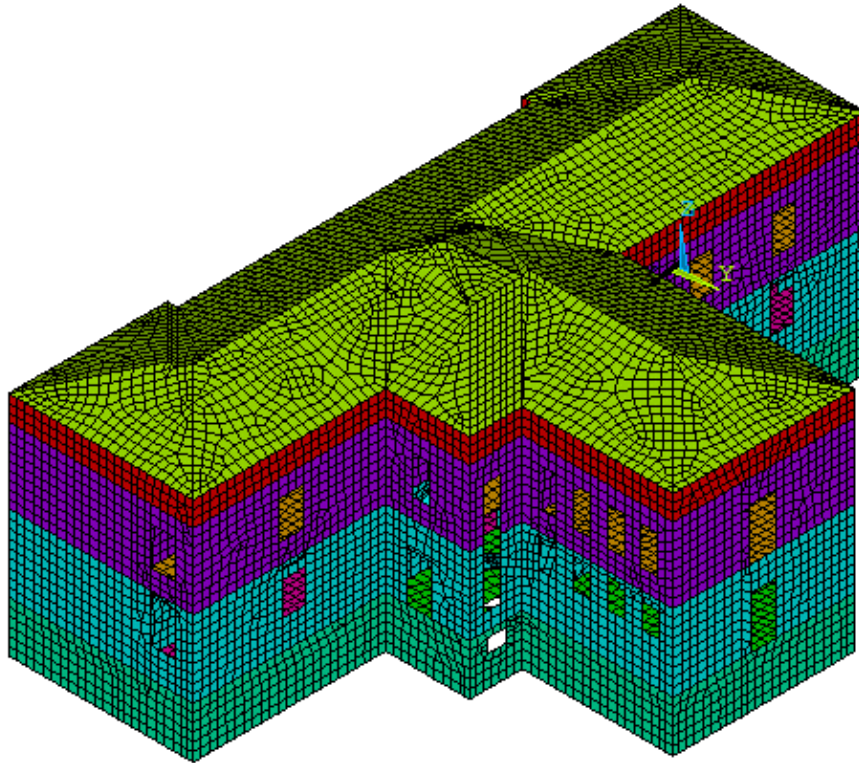


Figure 0.16: Modelling of the building using FEM software.

Thanks to the modeling of the structure using FE software, reported in Figure 0.16, and following the analysis of the loads performed both on structural elements and not, were identified the masses related to the first and second floor, for our case will be the mass m_2 and the mass m_3 .

It is therefore now aware of the totality of the masses participating in the phenomenon used, and are finally reported in the following Table 0.7.

<i>Soil:</i>	<i>Raised Ground Floor:</i>	<i>Soil+Raised Ground Floor:</i>	<i>1st Floor:</i>	<i>2nd Floor:</i>
m_s	m_{rf}	$m_1 = m_s + m_{rf}$	m_2	m_3
32467500	1602960	34070460	1675040	1188600

Table 0.7: Mass of the system, values in [Kg].

The above values refer to the following Figure 6.17, which shows, on the left, a prospectus of the building, while on the right the relative schematization of the disposition of the masses considered:

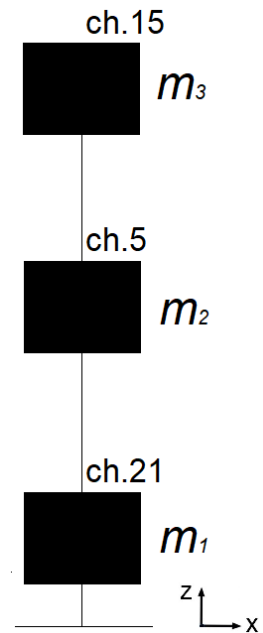


Figure 0.17: a) Building front; b) Ddisposition of the masses.

The lumped mass of the raised ground floor was then added to the mass of the soil to deal with the absence of records at the raised ground floor. The lumped masses of the first and second floor were attributed to the second and third DoF respectively.

6.3.2. Parameter determination, model updating

In this section we show the parameters determined through calibration using the selected algorithm: they identified, in particular, the linear parameters $K_{0,j}$ and D_j and non-linear B_j , C_j , E_j and N_j , concerning both the formulation of Bouc-Wen and Modified Davidenkov. We now proceed with a brief explanation on the calibration mode and the type of algorithm used.

In General, the calibration is done by minimizing the objective function (i.e. the cost function), going to equal the numerical values with the experimental values.

Once linear and nonlinear multipliers mentioned above have been defined, the choice of the variation range of these parameters has been: to update for example the nonlinear parameters of the laws, N_d , a hybrid particleswarm/patternsearch algorithm, [14], has been used, with lower and upper boundary on N_j of 1 and 10 respectively and starting value of 5.5. The procedure is shown below in a brief outline:

- Initially a first starting value is hypothesized and it is inserted within the numerical equation;
- I run the TFD (nn) and the TFD (ne) and make a difference, estimated later the form squared;
- Get a value of the cost function that defines the difference between the TFD.

It is therefore possible to affirm that, in each Iteration, the algorithm, generating a set of random parameters within the range chosen, in order to make converge the result for minimize the cost function J. In order to find the ni parameters, the cost function is now reported.

$${}^d J({}^d \mathbf{p}; N_d) = \int_0^{t_e} \left(\int_0^{f_s/2} \|T({}^d \mathbf{n}_n(t)) - T({}^d \mathbf{n}_e(t))\|_2^2 df \right) d\tau$$

Finally, it was possible to find, for each degree of freedom, the parameters characteristic of the linear part and not of the different formulations for Bouc Wen and Modified Davidenkov respectively:

- **Linear part**

3-rd Degree of Freedom

j	$K_{0,j1}$ [N/m]	$K_{0,j2}$ [N/m]	$K_{0,j3}$ [N/m]	D_{j1}	D_{j2}	D_{j3}
3	-168522817	-1373633633	1578364170	-6.70E-06	1.58E-06	7.63E-07

Table 0.8: Update parameters for the third DoF: $K_{0,jr}$ e D_{jr} .

2-nd Degree of Freedom

j	$K_{0,j1}$ [N/m]	$K_{0,j2}$ [N/m]	$K_{0,j3}$ [N/m]	D_{j1}	D_{j2}	D_{j3}
2	-1643395377	3262159987	-1373633633	5.50E-07	9.76E-07	1.58E-06

Table 0.9: Update parameters for the second DoF: $K_{0,jr}$ e D_{jr} .

1-st Degree of Freedom

j	$K_{0,j1}$ [N/m]	$K_{0,j2}$ [N/m]	$K_{0,j3}$ [N/m]	D_{j1}	D_{j2}	D_{j3}
1	55253915817	-1643395377	-168522817	1.65E-06	5.50E-07	-6.70E-06

Table 0.10: Update parameters for the first DoF: $K_{0,jr}$ e D_{jr} .

- **Non linear part**

Finally, there are remaining parameters related to the nonlinear part of the formulations, in particular therefore B, C and N for Bouc-Wen and and for Modified Davidenkov for the 3 DoF of the simplified model:

3-rd Degree of Freedom

j	B _j	C _j	N _j
3	73.62	27.82	1.0142

Table 0.11: Update non linear parameters for the third DoF: B_j, C_j, N_j.

2-nd Degree of Freedom

j	B _j	C _j	N _j
2	71.82	-17.68	1.0109

Table 0.12: Update non linear parameters for the second DoF: B_j, C_j, N_j.

1-st Degree of Freedom

j	B _j	C _j	N _j	E ₁
1	60288072791	13910459	1.0446	-2.06E-06

Table 0.13: Update parameters for the first DoF: B_j, C_j, N_j, E₁.

At this point, thanks to the knowledge of the parameters constituting the formulations of Bouc Wen and Davidenkov, it was possible to graphify the restoring force for the 3 degrees of freedom of the simplified model, comparing the numerical one (in red) and experimentally one (in black).

In Figure 0.18 it is thus reported the restoring force referred to the first degree of freedom (thus referred to the ground), which, it is recalled, is determined through the formulation of Davidenkov.

In particular, the trend of the black line, which refers to the experimental value, is given by the acceleration recorded by channel 21 for the value of the mass referred to the first degree of freedom of the simplified model; the red trend, on the other hand, represents the restoring force always given by the mass m_1 for the acceleration which involves the numerical model considered following the calibration of the parameters.

It is also important to underline how, in fact, the trends represent the cycles of histerisi for a real building.

It is possible to note from the graph that the stiffness, determinable as the ratio between the force and the displacement, is taken in a quite satisfactory way, however the experimental curve shows discrepancies from the numerical one in particular for the non linear where the values are more discordant. This behavior can be justified by the fact that the model used involves the use, for example, of solid stiffness matrices: however, for the soil, being a material with variable behaviour, there is a higher degree of uncertainty compared to materials such as concrete or masonry and, therefore, such uncertainties are reperdimensing on the fitting of experimental and numerical data.

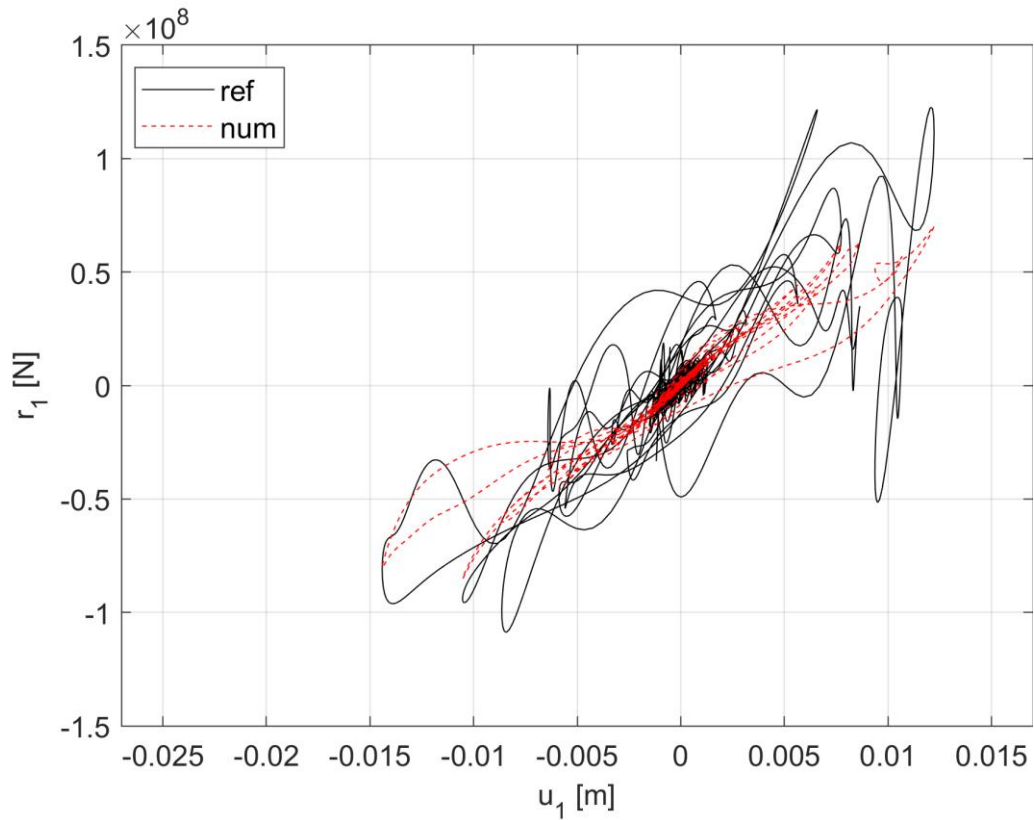


Figure 0.18: Trend of numerical and experimental Restoring force for first DoF.

As regards the second restoring force, it is recalled that it is determined by the accelerogram recorded at Channel 5 and the mass of the second degree of freedom of the simplified model considered.

It is possible to see in Figure 0.19 like the numerical curve (identified thanks to the formulation of Bouc-Wen), it is very good for the experimental one, even if you have slight discrepancies as if the whole model for the nonlinear part was more hardening than in reality.

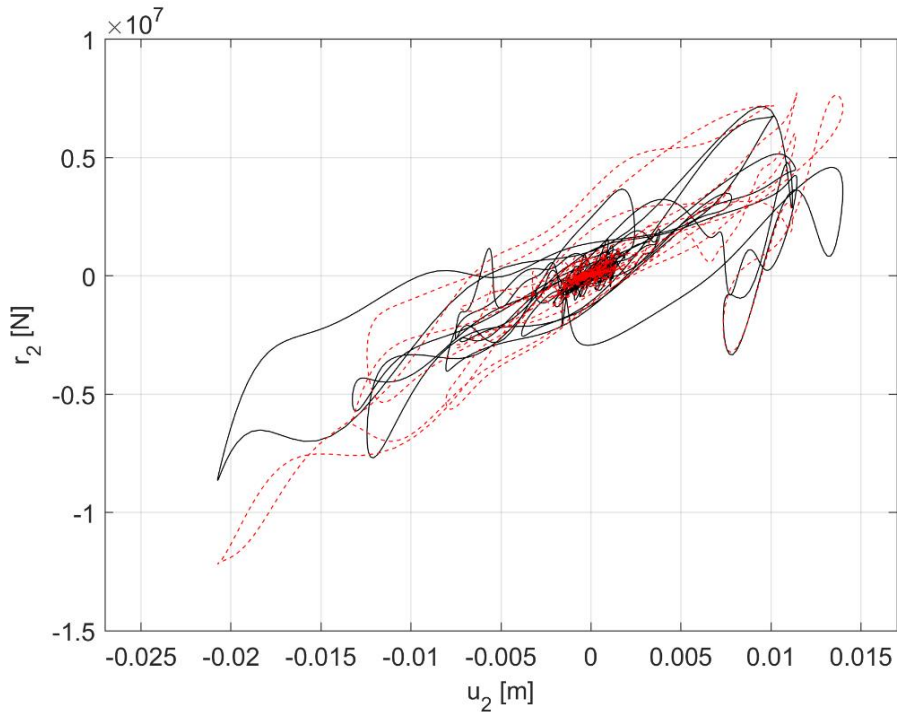


Figure 0.19: Trend of numerical and experimental Restoring force for second DoF.

You can notice, instead, in Figure 0.20 what the numerical restoring force referred to the third degree of freedom to fit the experimental trend, determined, this time, by recording the accelerogram from Channel 26.

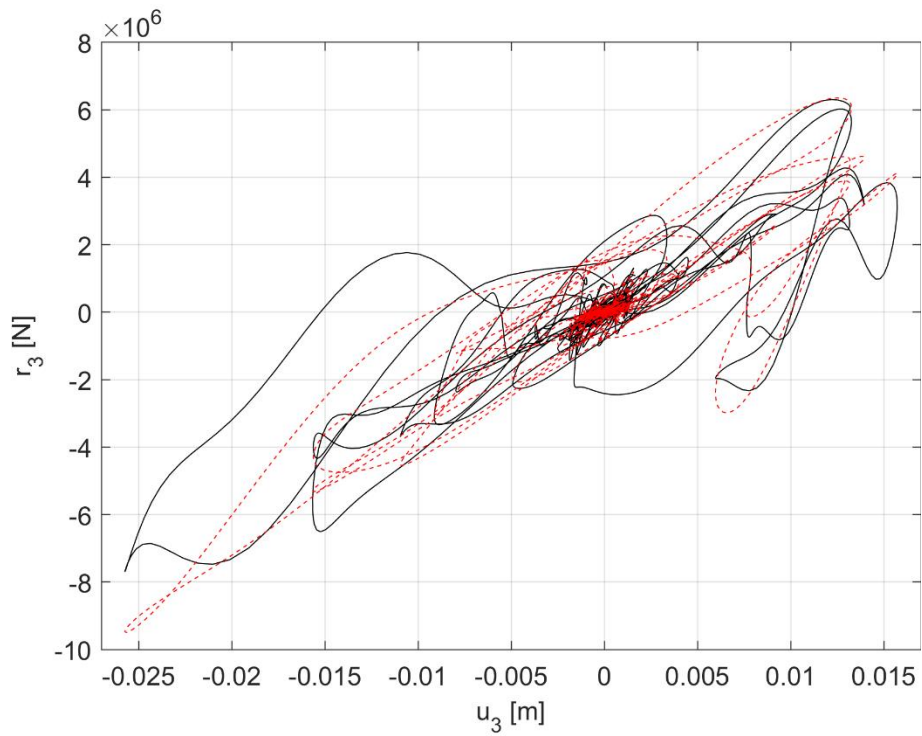


Figure 0.20: Trend of numerical and experimental Restoring force for first DoF.

In Summary, it is possible to be satisfied with the tenant for the third and second degree of freedom, because the trends of experimental curves and numerical curves, except for minor discrepancies, are similar. The trend of the numerical curve for the first degree of freedom, however, is slightly discordative from the experimental one: this testifies to the fact that the ground represents a component on which there are widespread uncertainties, both as regards the matrices of stiffness taken both for the recruitment considered.

It is now possible to represent the variation of the force over time.

Considering a time interval between 1.5 and 6 seconds, in the following Figure 0.21, Figure 0.22, Figure 0.23 there is the trend of force as time varies, both for the numerical case and for the experimental case; it is evident, in particular, how the first and third, referring respectively to the first and third DoF, fit satisfactorily the evolution of the experimental value for almost the whole of the time interval considered, conversely, on the other hand, the second Force, inherent in the second DoF, thick in a less satisfactory manner for narrow intervals of time.

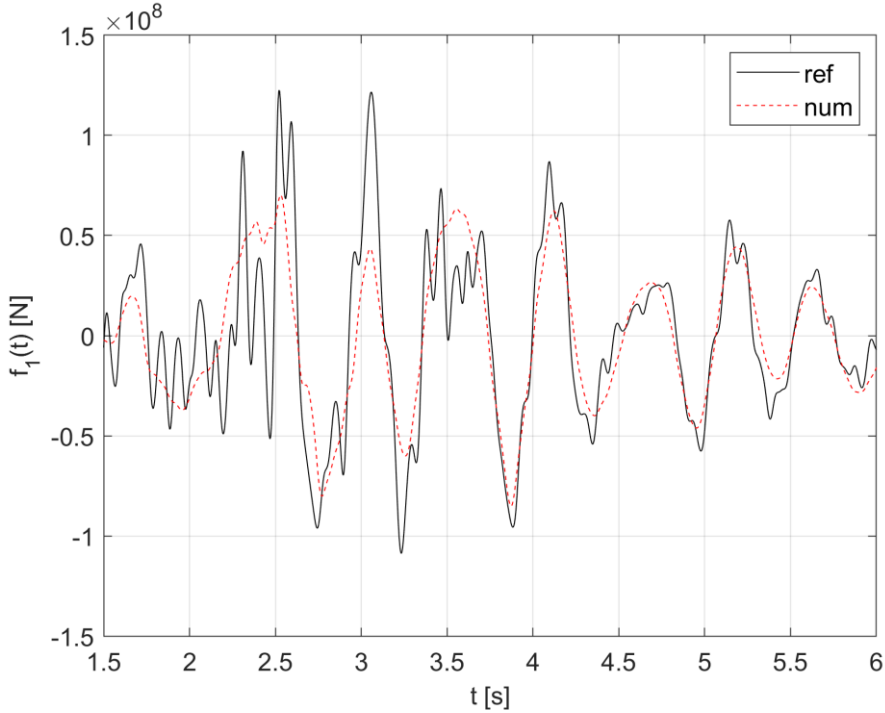


Figure 0.21: Variation of Force on time about 1st DoF.

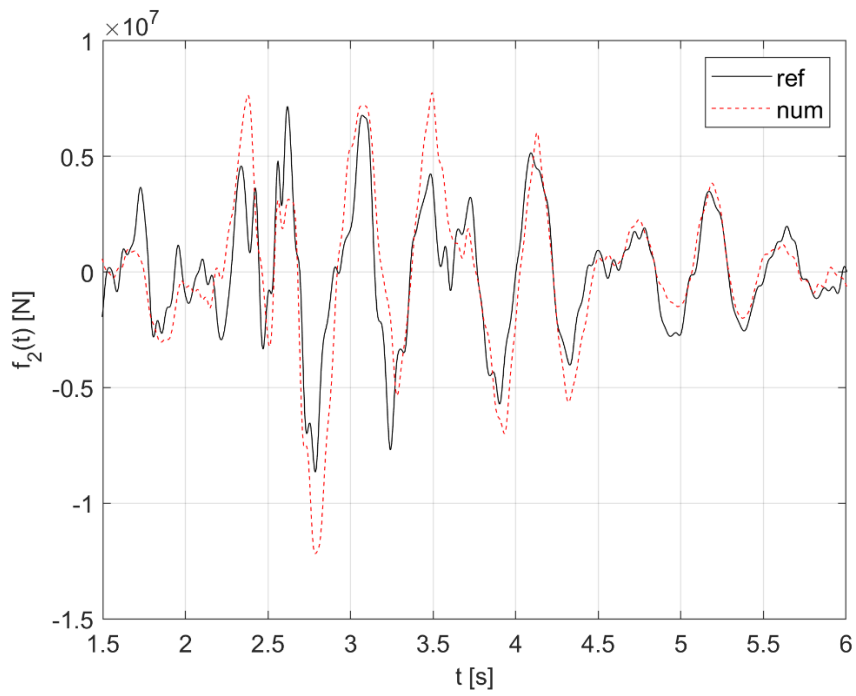


Figure 0.22: Variation of Force on time about 2nd DoF.

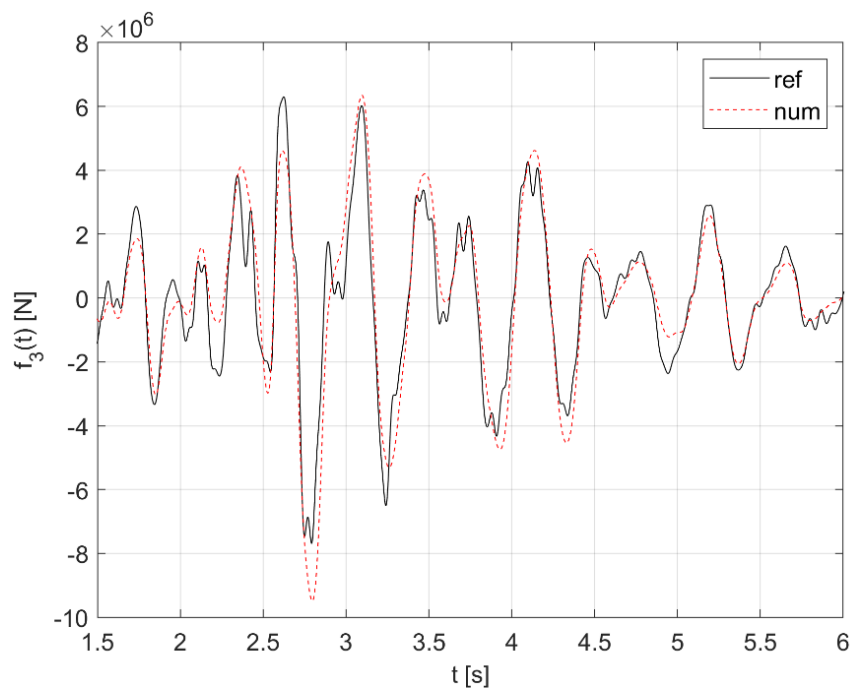


Figure 0.23: Variation of Force on time about 3rd DoF.

6.3.3. Postprocessing

After the calibration of parameters, self analysis was carried out, i.e. the analysis of eigenelements and autoveptors for each moment of time.

Initially the constancy of the K_0 has occurred in time and later, it was possible to calculate a time variant stiffness matrix using:

$$K_{jr} = K_{0,jr} - K_{0,jr} \delta_{jr} \epsilon$$

In order to solve a time dependent Eigen-Problem, it is initially necessary to consider the previously obtained mass matrix, defined as:

$$M = \begin{bmatrix} m_1 & 0 & 0 \\ 0 & m_2 & 0 \\ 0 & 0 & m_3 \end{bmatrix} = \begin{bmatrix} 34070460 & 0 & 0 \\ 0 & 1675040 & 0 \\ 0 & 0 & 1188600 \end{bmatrix}$$

By introducing in the code a vector having as dimension 1xlength of the signal over time, with the previously written formulation, subsequently, it is therefore possible to determine by problem to the sixths a matrix of stiffness in the time and, consequently, derive a variation of the frequency over time.

It is possible return to the following Figure 0.24, the variation of the frequency over time, both as regards f_1 , f_2 and f_3 . It denotes, in particular, that the first frequency started from a value of 3.88 Hz, similar to the value you had for the ground, following the calibration, where you had $f_2 = 3.90$ Hz in X-direction.

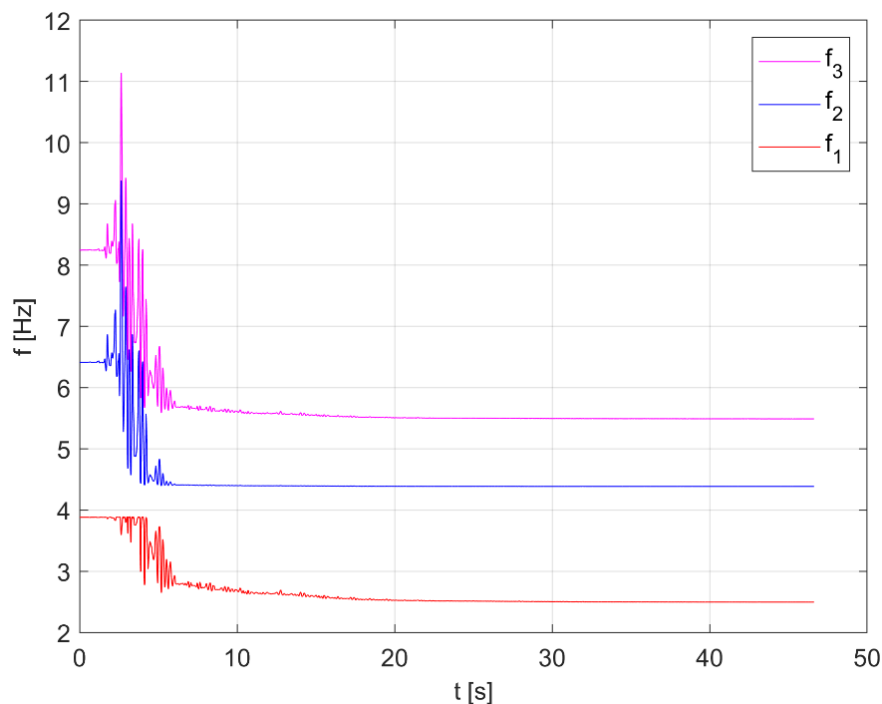


Figure 0.24: Variation of Frequency on time.

In Figure 0.25 instead, it is reported the trend of elastic stiffness as time varies, it shows how, after about 10 seconds, all reach a certain stability.

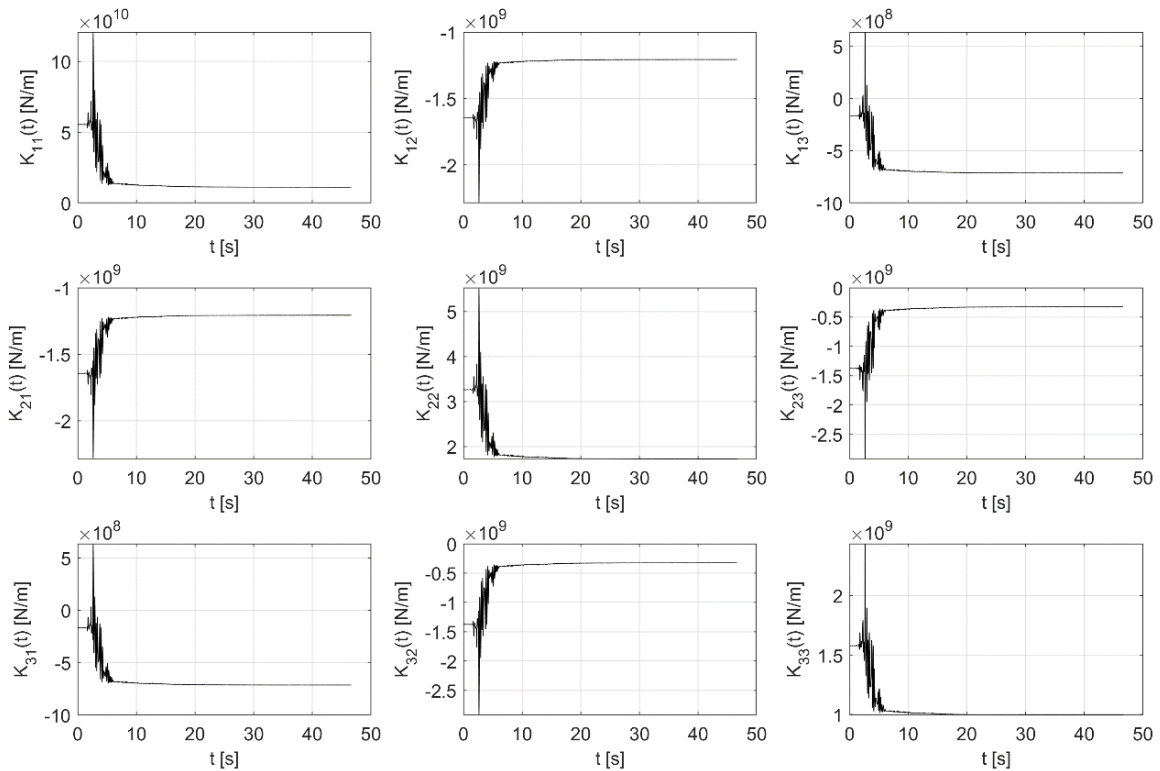


Figure 0.25: Variation of Stiffness on time.

One can thus obtain modal forms over time with consequent determination of the parameter of interaction terrain structure, also in time.

The results of the eigen-analysis are reported in Figure 0.26 and Figure 0.27, which report the pre- and post- main shock frequencies, f_h , the percentage of participation mass, $M_{p,h}$.

For the frequencies, a global reduction of the values is denoted for each mode. The reduction is almost uniform approaching the 35 % for the first mode, the 31 % for the second mode and the 33 % for the last mode.

It is worth noting that reduction in frequency values cannot be directly related to damage when modal quantities are identified with strong earthquakes, in fact the existence of amplitude-frequency relations can temporarily cause a wander in frequency values [37].

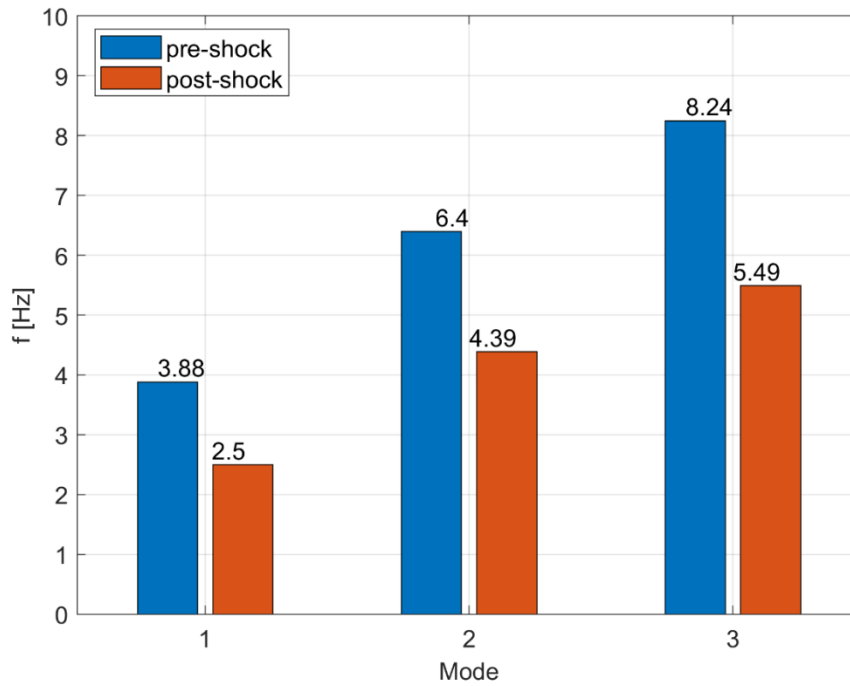


Figure 0.26: Identified modal quantity, pre- and post- main shock: percentage of participation mass.

It is possible to notice from the graph above how the numerical frequency of the soil-structure system, equal to 3.88 Hz, is very similar to the numerical frequency of the only soil system in the x direction, and equal to 3.90 Hz.

As regards the percentage of participation mass, a sudden inversion of the participation between the first two modes is observed after the main shock, resulting in a high participation of the first mode (about 98.54 %).

For the third mode, a low participation is noticed before and after the main shock, con valore rispettivamente di 0.57 e 0 %.

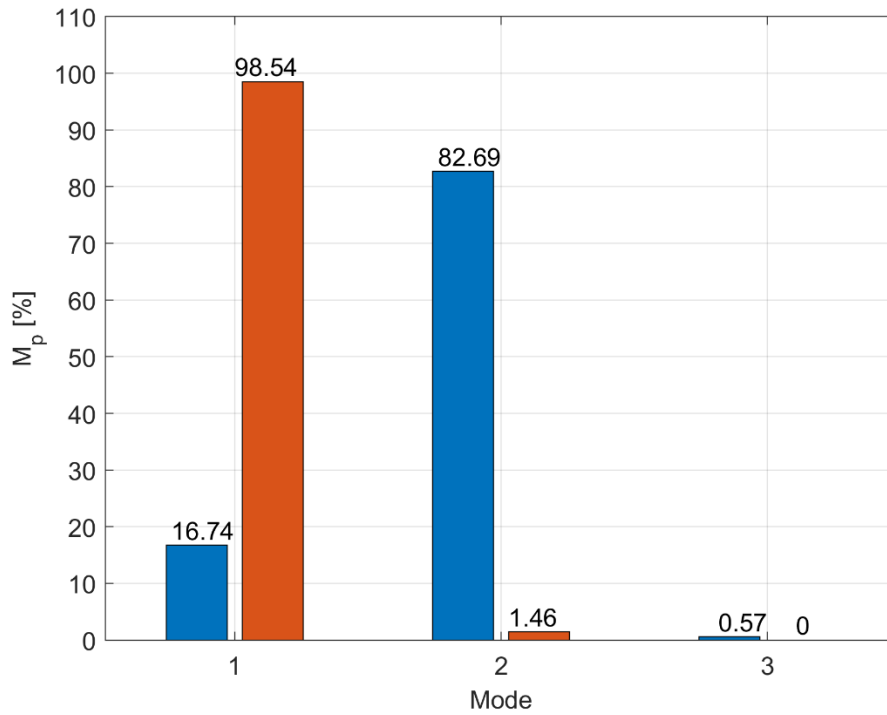


Figure 0.27: Identified modal quantity, pre- and post- main shock: percentage of participation mass.

From the following figures is instead possible to observe the modal shapes for the three identified modes pre- and post- main shock.

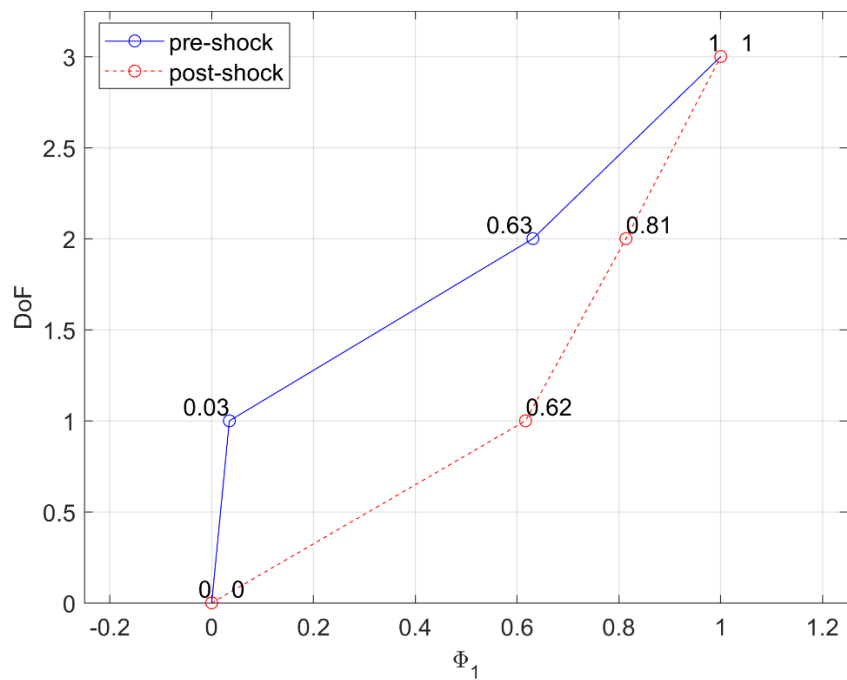


Figure 0.28: Identified modal shape, pre- and post- main shock: 1st mode.

In Figure 0.28 it is evident the non-interaction before the earthquake, while following the earthquake it is possible to notice instead a rigid form, in which the displacement of the structure is almost constant, while one has exclusively a displacement of the ground: it is thus in the condition of the Maximum interaction in which the dynamics of the simplified model is regulated mainly by the ground. What is said is justified by the fact that in Figure 0.27 the participant mass passes from a pre-quake value of 16.74 to a post-earthquake value of 98.54%.

In Figure 0.29 the second modal form of the soil-structure system, pre (in blue) and post (in red) is represented. Before the earthquake there is a high value regarding the displacement of the soil and a modest variance; this is testified by the fact that one has a participant mass value referred to the second high mode, equal to 82.69%, and a value of SSII equal to 48.21% and therefore i have a marked interaction between the structure and the ground.

After the quake, however, the value of the interaction is lowered, and this is testified by both the modest participant mass value, 1.46%, and the value of 13.91% of SSII.

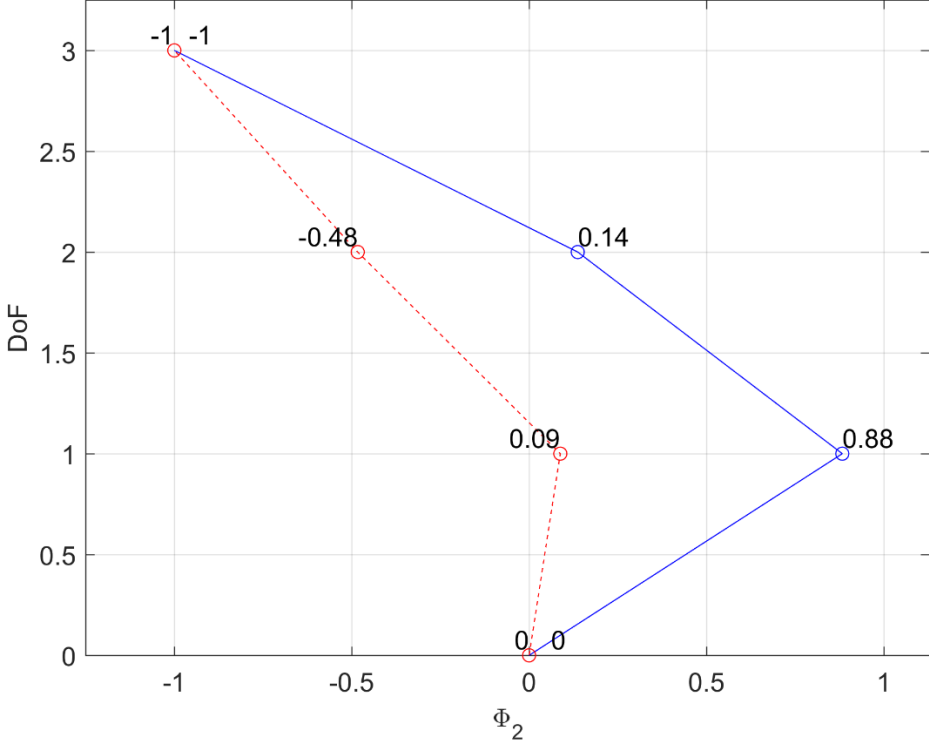


Figure 0.29: Identified modal shape, pre- and post-main shock: 2nd mode.

Instead, as regards the third modal form, present in Figure 0.30, the non-interaction between soil and structure is evident, both for the pre- and post case.

This is obvious if you consider the mass values participating in Figure 0.27, equal to 0.57 and 0% respectively for the pre- and post-quake case.

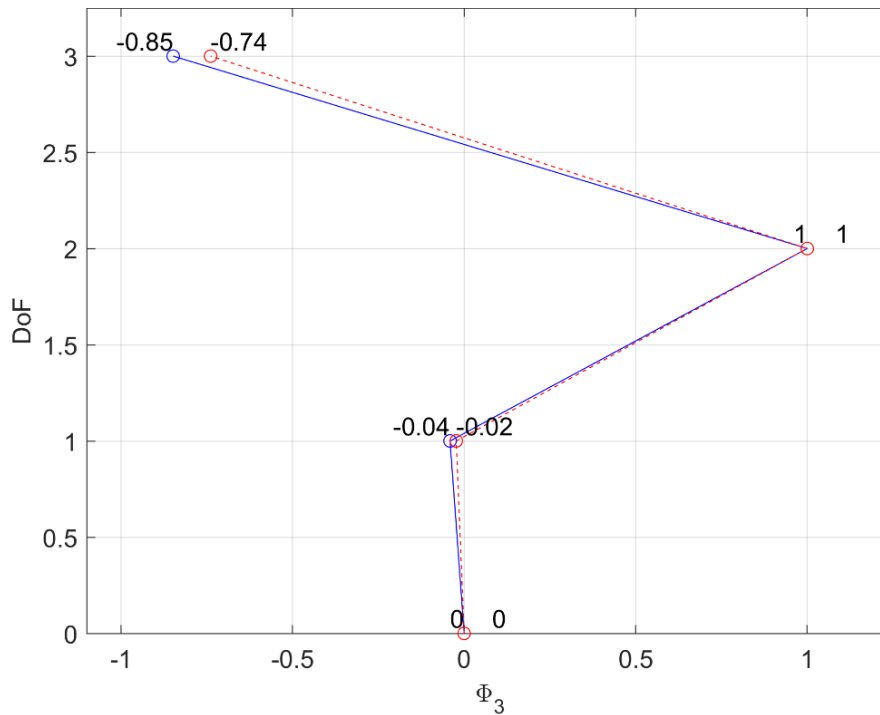


Figure 0.30: Identified modal shape, pre- and post-main shock: 3rd mode.

The following Soil-Structure Interaction index, $SSII_h$, to quantify the soil effects on each mode, h , of the building, are now reported:

$$SSII_h = \frac{|\phi_{1,h}|}{|\phi_{1,h}| + \sigma(\phi_h)}$$

Where:

- $\phi_{1,h}$ is the coordinate of the eigenvector ϕ_h , related to the DoF of the soil;
- $\sigma(\phi_h)$ is the unbiased standard deviation of the eigenvector.

By equation of SSII, it is easy to note that $SSII_h$, is a quantity that takes values between 0 and 1, as all the terms in the equation are positive.

We now analyse the two different possibilities:

- $SSII_h$ approach values of 1 it means that the deviation of the modal shape is zero, and then the building behaves, for the analyzed mode, as a rigid body on the ground. Situation of maximum interaction for which the dynamic is governed exclusively by the ground in which the building remains almost stationary;
- $SSII_h$ tends to zero it means that the coordinate of the soil is very low if compared with a variation of the modal shape, indicating a low role of the soil in the dynamics.

Finally, because the linearity of the terms, SSI_h , and thus SSI , are invariant respect to a rescaling of the modal shapes.

Figure 0.31 reports the SSI indices calculated for the case study, in particular for the pre and post shock.

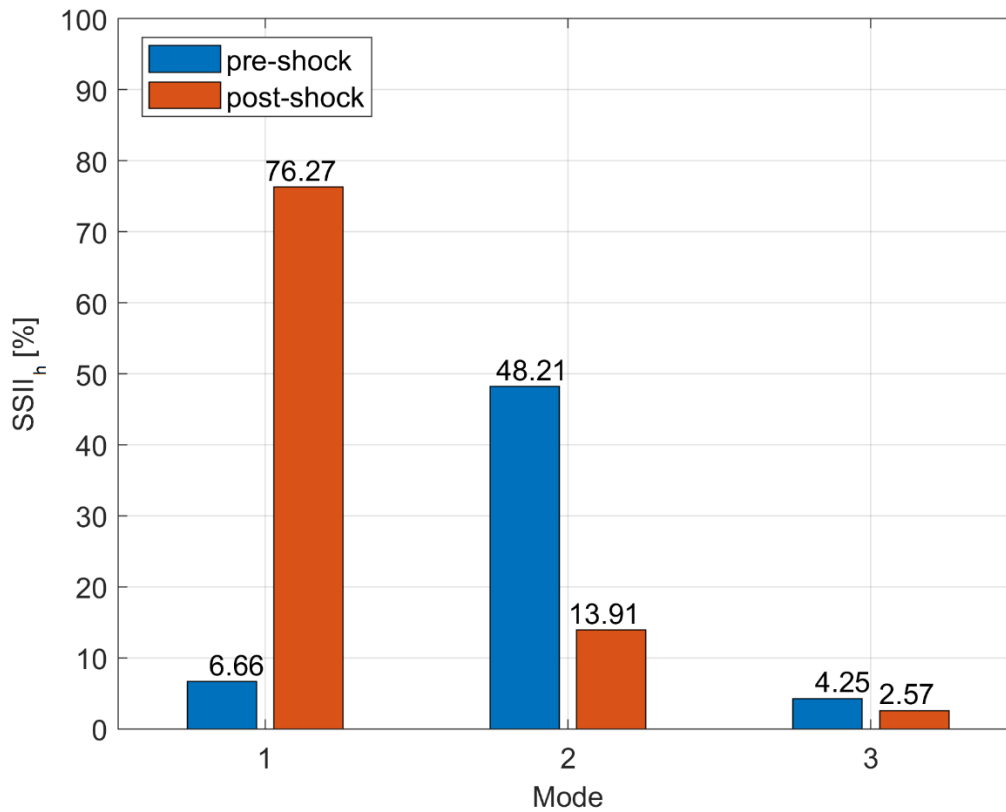


Figure 0.31: Proposed Soil-Structure Interaction index, pre- and post- shock: SSI_h .

From Figure 0.31 it is thus possible to observe pre-and post-quake values for various ways:

- Pre-Quake: the value of the soil was mainly acting on the second way, the value of SSI being equal to 48.21%; a confirmation can be seen in Figure 0.27 as the second way has a very high participant mass equal to 82.69% of the total participant mass;
- During The quake: SSI is governed almost exclusively by the first mode, which has a value equal to 76.27% of the total value; therefore, following the event, the first way was the one most subject to the phenomenon of the interaction soil structure. It is also testified by the fact that the first mode undergoes the most significant change and, while for mode 2 and 3 the value of SSI is decreased, for the first one is increased.

This is also testified by the fact that you had a frequency of 3.88 Hz and one $f_2=3.90$ Hz.

The SSII index can be then combined using a modal combination technique, e.g. the Squared Root of the Sum of the Squares (SRSS), to obtain an index of the building defined by:

$$SSII = \sqrt{\sum_h SSII_h^2}$$

The SRSS technique for the case study was adequate as the modes are well distanced.

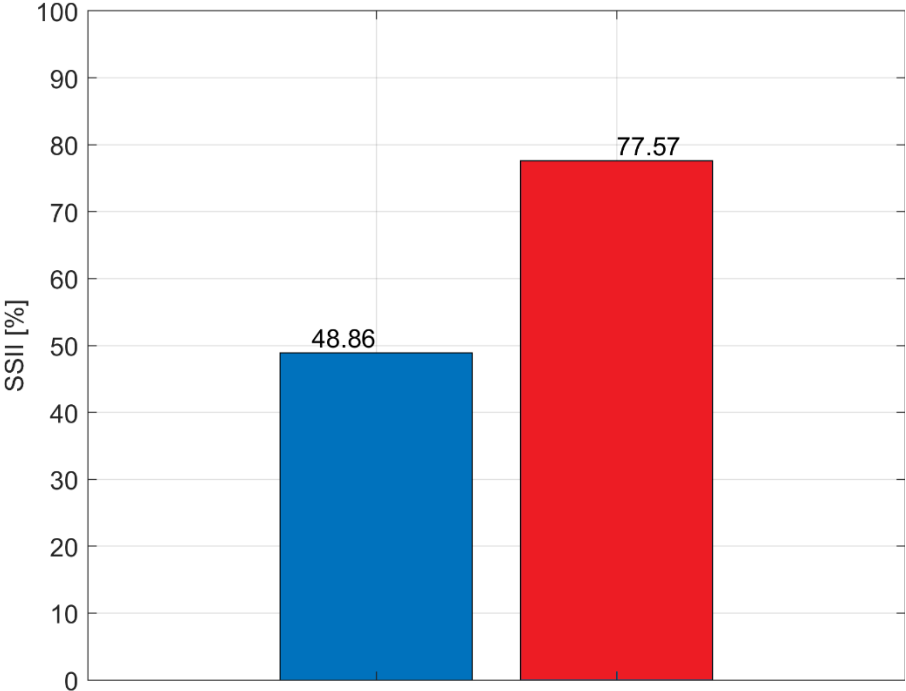


Figure 0.32: Proposed Soil-Structure Interaction index, pre- and post- shock: SSII.

In Figure 0.32 is represented the modal combination of the structure indicator for both the pre-quake and the post, it is possible to affirm that the structure has certainly undergone interaction, and this is given by the fact that the percentage value increases and goes from 48.86 to 77.57%: this is due to the fact that during the earthquake the ground has taken on more and more importance in the dynamics of the building, as if the mass of soil, according to our assumptions at 18 meters of depth, was increasingly detached from the rest of the ground below and you both incorporated in the general soil-structure system. What has been said testifies to the fact that during a generic earthquake, the dynamics of the buildings interacts closely with the dynamics of the soil, with the generation of a model that involves the particles of both the masses and both the dynamics.

In summary, from Figure 0.31 it is possible to conclude that the SSI mainly affected the first mode after the main shock, while the effects on the remaining modes decreased during the quake. However, Figure 0.32, suggests an increase of the soil effects in the dynamics of the overall building at the end of the quake.

7. Conclusion

In the present work, the calibration of a nonlinear system that accounts for soil-structure interaction phenomena has been performed by minimizing the difference between the Time-Frequency Distribution (TFD) of the recorded signals and the TFD of a numerical black-box model consisting of rate-independent Bouc-Wen type oscillators for the upper part of the system and a modified, rate-dependent, Davidenkov type oscillator for the bottom part.

For the estimates of the masses of the mixed soil-structure 3 DoFs system, available FE models have been adopted, thanks to which it was possible to determine the masses referred to the second and the third degree of freedom of the structure. Then a deconvolution of the seismic ground motion has been performed to obtain the acceleration input, at 18 m under the surface, of the mixed system. For the deconvolution, an equivalent linear elastic method was used, with the determination of specific constitutive laws for the decay curves inherent in the relationships between the shear resistance modules and damping, as the particle size varies. The calibrated nonlinear model was then used to solve the time dependent eigen-problem. This allowed the estimate of the modal parameters before and after the quake: in particular the variation of frequency and stiffness on time. The nonlinear identification has been performed on a reduced model of the building, connected with a reduced model of the soil that was preliminary calibrated to fit the first experimental frequency of the site of the building.

Finally, an index to quantify the soil effects on the dynamics of the system has been proposed. The results of the work are summarized hereinafter:

- The calibrated linear FE model of the soil reveals a first frequency in accordance with the experimental data, i.e. 3.64 Hz, and a second and third frequency of 3.90 Hz and 4.24 Hz, respectively;
- From the third layer of the soil up, the contrast of impedance starts to increase suddenly, indicating a high amplification of the waves in those layers, respect to the wave in the bedrock;
- After the quake, all the frequencies of the system reduced of about 33-35%, however, the system exhibited a strong soil-structure interaction, quantified on a scale between 0 and 1 at about 76%. This could have affected the estimate of the frequencies, as a high play of the soil in the dynamics of the system, would produce a wandering of the frequency value due to its time variant nature;
- The soil behavior predominantly affected the first mode, in fact the soil-structure interaction index increased from 6.66 % up to 76.27 %. For the other modes the soil effects on the dynamics of the system were reduced during the quake. This bring to

the consideration that the first mode may have been more subjected to wandering effects due to possible strong changes in soil constitution.

Due to the availability of time dependent modal properties, as a future work, the connection between the proposed soil-structure interaction index, SSI_h , and the instantaneous frequencies of the system, f_h , could be studied to find possible correlation paths or causality dependence.

8. Attachments

8.1. Non-linear identification

```
close all;
clear;
clc;
tic;

%% SOLVERS DATA
global Fd3;
global eps;
global v1;
global v2;
global v3;
global F3;
global fs;
global te;
global windo;
%
global Fd2;
global K23;
global K31;
global K32;
global K33;
global F2;
%
global F1;
global K12;
global K13;
global K21;
global K22;
global u1;
global u2;
global u3;
%
global BBf
global AAf

N3min = 1;
N3max = 10;
N3start = 5.5;
%
N2min = 1;
N2max = 10;
N2start = 5.5;
%
N1min = 1;
N1max = 10;
N1start = 5.5;

sol = 7;

% sol = 1 -> interior point
% sol = 2 -> minimax optimization
% sol = 3 -> genetic algorithm
% sol = 4 -> patternsearch
% sol = 5 -> simulated annealing
```

```

% sol = 6 -> particleswarm
% sol = 7 -> hybrid particleswarm-patternsearch

optionsPSOPS = optimoptions('particleswarm');
optionsPSOPS.HybridFcn = @patternsearch;
optionsPSOPS.SwarmSize = 10;

%% INPUT DATA

dir = 'X';

% % 26-10-main
name = '201610261710';

% setting initial condition to have zero velocity
if dir == 'Y'
    nsampi = round(1.132*fs);
elseif dir == 'X'
    nsampi = round(1.356*fs);
end

nsampf = length(ACCI);

ts = 1/fs;
t = (0:(nsampf-nsampi+1)-1)*ts;
te = t(end);
fres = 1/te;
f = -fs/2:fres:fs/2;

ag = ACCI(nsampi:nsampf);

a3 = ACC(nsampi:nsampf,3);
a2 = ACC(nsampi:nsampf,2);
a1 = ACC(nsampi:nsampf,1);

v3 = VEL(nsampi:nsampf,3);
v2 = VEL(nsampi:nsampf,2);
v1 = VEL(nsampi:nsampf,1);

u3 = DIS(nsampi:nsampf,3);
u2 = DIS(nsampi:nsampf,2);
u1 = DIS(nsampi:nsampf,1);

ge3 = -(a3+ag);
ge2 = -(a2+ag);
ge1 = -(a1+ag);

gde3 = gradient(ge3,ts);
gde2 = gradient(ge2,ts);
gde1 = gradient(ge1,ts);

mrf = 1602960;
mpp = 1675040;
mur = 1188600;
Msoil = 32467500;

m3 = mur;
m2 = mpp;

```

```

m1 = Msoil+mrf;

f3 = m3*ge3;
f2 = m2*ge2;
f1 = m1*ge1;

fd3 = m3*gde3;
fd2 = m2*gde2;
fd1 = m1*gde1;

F3 = f3;
F2 = f2 + f3;
F1 = f1 + f2 + f3;

Fd3 = fd3;
Fd2 = fd2 + fd3;
Fd1 = fd1 + fd2 + fd3;

windo = hamming(max(round(length(ag)/11),2), 'periodic');

eps = cumtrapz(t,f3.*v3) + cumtrapz(t,f2.*v2) + cumtrapz(t,f1.*v1);

%% Filter design
Wp = [0.5 20]/(fs/2);
Ws = [0.5/1.25 20*1.25]/(fs/2);
Rp = 3;
Rs = 8;
[order_butter,WWWn] = buttord(Wp, Ws, Rp, Rs);
[BBf,AAf] = butter(order_butter,WWWn);

%% NLI DoF n. 3
ne = []; ni = [];

% start NL calibration of N -----
fprintf('Starting optimization of N3 \n');
if sol == 1
    [N3,W3best] = fmincon( @OFN3 , N3start , [] , [] , [] , [] , N3min ,
N3max);
elseif sol == 2
    [N3,W3best] = fminimax( @OFN3 , N3start , [] , [] , [] , [] , N3min ,
N3max);
elseif sol == 3
    [N3,W3best] = ga( @OFN3 , 1 , [] , [] , [] , [] , N3min , N3max);
elseif sol == 4
    [N3,W3best] = patternsearch( @OFN3 , N3start , [] , [] , [] , [] ,
N3min , N3max);
elseif sol == 5
    [N3,W3best] = simulannealbnd( @OFN3, N3start , N3min , N3max);
elseif sol == 6
    [N3,W3best] = particleswarm( @OFN3 , 1 , N3min , N3max);
elseif sol == 7
    optionsPSOPS.InitialSwarmMatrix =
N3start*ones(round(optionsPSOPS.SwarmSize/3),1);
    [N3,W3best] = particleswarm( @OFN3 , 1 , N3min , N3max , optionsPSOPS
);
end
N3
W3best
fprintf('End optimization of N3 \n');

```

```

% end NL calibration of N -----

ne = Fd3;
ne = filtfilt(BBf,AAf,ne);

ni(:,1) = v1;
ni(:,2) = -v1.*eps;
ni(:,3) = v2;
ni(:,4) = -v2.*eps;
ni(:,5) = v3;
ni(:,6) = -v3.*eps;
ni(:,7) = -sign((v3-v2).*F3).*abs(F3).^N3.*(v3-v2);
ni(:,8) = -abs(F3).^N3.*(v3-v2);
ni = filtfilt(BBf,AAf,ni);

[p,TIME,FREQ] = dirpeest(ni,ne,fs,te,2,windo);
p(end,:) = dirpeest(ni,ne,fs,te,1,windo);
TIMEv = (TIME(1):TIME(2):TIME(3))'; TIME(2);
FREQv = (FREQ(1):FREQ(2):FREQ(3))'; FREQ(2);

% Inequality constraints

for ii = 1:length(TIMEv)
    if p(ii,5) < 0
        p(ii,5) = 0;
    end
    if p(ii,6) < 0
        p(ii,6) = 0;
    end
    if p(ii,7) < 0
        p(ii,7) = 0;
    end
    if p(ii,8) < -p(ii,7)
        p(ii,8) = -p(ii,7);
    end
    if p(ii,8) > p(ii,7)
        p(ii,8) = p(ii,7);
    end
end

K031 = p(:,1); K013 = K031;
d31 = p(:,2)./p(:,1); d13 = d31;
K032 = p(:,3); K023 = K032;
d32 = p(:,4)./p(:,3); d23 = d32;
K033 = p(:,5);
d33 = p(:,6)./p(:,5); d33(find(isnan(d33)==1)) = 0; d33(find(d33==inf)) =
0; d33(find(d33==--inf)) = 0;
bet3 = p(:,7);
gam3 = p(:,8);

nn3 = nansum((p(end,).*ni).').';

Fd3_est = nn3;

fd3_est = Fd3_est;
fd3_est = filtfilt(BBf,AAf,fd3_est);

f3_est = cumtrapz(t,fd3_est);

```

```

K31 = K031(end)*(1-d31(end)*eps);
K32 = K032(end)*(1-d32(end)*eps);
K33 = K033(end)*(1-d33(end)*eps);
%
K23 = K023(end)*(1-d23(end)*eps);
K13 = K013(end)*(1-d13(end)*eps);

%% NLI DoF n. 2
ne = []; ni = [];

% start NL calibration of N -----
fprintf('Starting optimization of N2 \n');
if sol == 1
    [N2,W2best] = fmincon( @OFN2 , N2start , [] , [] , [] , [] , N2min ,
N2max);
elseif sol == 2
    [N2,W2best] = fminimax( @OFN2 , N2start , [] , [] , [] , [] , N2min ,
N2max);
elseif sol == 3
    [N2,W2best] = ga( @OFN2 , 1 , [] , [] , [] , [] , N2min , N2max);
elseif sol == 4
    [N2,W2best] = patternsearch( @OFN2 , N2start , [] , [] , [] , [] ,
N2min , N2max);
elseif sol == 5
    [N2,W2best] = simulannealbnd( @OFN2, N2start , N2min , N2max);
elseif sol == 6
    [N2,W2best] = particleswarm( @OFN2 , 1 , N2min , N2max);
elseif sol == 7
    optionsPSOPS.InitialSwarmMatrix =
N2start*ones(round(optionsPSOPS.SwarmSize/3),1);
    [N2,W2best] = particleswarm( @OFN2 , 1 , N2min , N2max , optionsPSOPS
);
end
N2
W2best
fprintf('End optimization of N2 \n');
% end NL calibration of N -----

ne = Fd2 - (K23.*v3 + K31.*v1 + K32.*v2 + K33.*v3);
ne = filtfilt(BBf,AAf,ne);

ni(:,1) = v1;
ni(:,2) = -v1.*eps;
ni(:,3) = v2;
ni(:,4) = -v2.*eps;
ni(:,5) = -sign((v2-v1).*F2).*abs(F2).^N2.*(v2-v1);
ni(:,6) = -abs(F2).^N2.*(v2-v1);
ni = filtfilt(BBf,AAf,ni);

p = dirpest(ni,ne,fs,te,2,windo);
p(end,:) = dirpest(ni,ne,fs,te,1,windo);

% Inequality constraints
for ii = 1:length(TIMEv)
    if p(ii,3) < 0
        p(ii,3) = 0;
    end
    if p(ii,4) < 0
        p(ii,4) = 0;
    end
end

```

```

    if p(ii,5) < 0
        p(ii,5) = 0;
    end
    if p(ii,6) < -p(ii,5)
        p(ii,6) = -p(ii,5);
    end
    if p(ii,6) > p(ii,5)
        p(ii,6) = p(ii,5);
    end
end
end

K021 = p(:,1); K012 = K021;
d21 = p(:,2)./p(:,1); d12 = d21;
K022 = p(:,3);
d22 = p(:,4)./p(:,3); d22(find(isnan(d22)==1)) = 0; d22(find(d22==inf)) =
0; d22(find(d22==-inf)) = 0;
bet2 = p(:,5);
gam2 = p(:,6);

nn2 = nansum((p(end,:).*ni).').';

Fd2_est = nn2 + (K23.*v3 + K31.*v1 + K32.*v2 + K33.*v3);

fd2_est = Fd2_est - fd3;
fd2_est = filtfilt(BBf,AAf,fd2_est);

f2_est = cumtrapz(t,fd2_est);

K21 = K021(end)*(1-d21(end)*eps);
K22 = K022(end)*(1-d22(end)*eps);
%
K12 = K012(end)*(1-d12(end)*eps);

%% NLI DoF n. 1
ne = []; ni = [];

% start NL calibration of N -----
fprintf('Starting optimization of N1 \n');
if sol == 1
    [N1,Wlbest] = fmincon( @OFN1 , N1start , [] , [] , [] , [] , N1min ,
N1max);
elseif sol == 2
    [N1,Wlbest] = fminimax( @OFN1 , N1start , [] , [] , [] , [] , N1min ,
N1max);
elseif sol == 3
    [N1,Wlbest] = ga( @OFN1 , 1 , [] , [] , [] , [] , N1min , N1max);
elseif sol == 4
    [N1,Wlbest] = patternsearch( @OFN1 , N1start , [] , [] , [] , [] ,
N1min , N1max);
elseif sol == 5
    [N1,Wlbest] = simulannealbnd( @OFN1, N1start , N1min , N1max);
elseif sol == 6
    [N1,Wlbest] = particleswarm( @OFN1 , 1 , N1min , N1max);
elseif sol == 7
    optionsPSOPS.InitialSwarmMatrix =
N1start*ones(round(optionsPSOPS.SwarmSize/3),1);
    [N1,Wlbest] = particleswarm( @OFN1 , 1 , N1min , N1max , optionsPSOPS
);
end

```

```

Wlbest
fprintf('End optimization of N1 \n');
% end NL calibration of N -----

ne = F1 - (K12.*u2 + K13.*u3 + K21.*u1 + K22.*u2 + K23.*u3 + K31.*u1 +
K32.*u2 + K33.*u3);
ne = filtfilt(BBf,AAf,ne);

ni(:,1) = u1;
ni(:,2) = -u1.*eps;
ni(:,3) = sign(v1).*( 2^(N1-1).*abs(u1).^N1 - (abs(u1)+sign(v1).*u1).^N1
)/N1;
ni(:,4) = sign(v1).*( 2^(N1-1).*abs(u1).^N1 - (abs(u1)+sign(v1).*u1).^N1
)/N1 .* eps;
ni(:,5) = v1;
ni = filtfilt(BBf,AAf,ni);

p = dirpest(ni,ne,fs,te,2,windo);
p(end,:) = dirpest(ni,ne,fs,te,1,windo);

% Inequality constraints
for ii = 1:length(TIMEv)
    if p(ii,1) < 0
        p(ii,1) = 0;
    end
    if p(ii,2) < 0
        p(ii,2) = 0;
    end
    if p(ii,5) < 0
        p(ii,5) = 0;
    end
end

K011 = p(:,1);
d11 = p(:,2)./p(:,1); d11(find(isnan(d11)==1)) = 0; d11(find(d11==inf)) =
0; d11(find(d11==--inf)) = 0;
B1 = p(:,3);
E1 = p(:,4)./p(:,3);
C1 = p(:,5);

nn1 = nansum((p(end,).*ni).').';

F1_est = nn1 + (K12.*u2 + K13.*u3 + K21.*u1 + K22.*u2 + K23.*u3 + K31.*u1 +
K32.*u2 + K33.*u3);

f1_est = F1_est - f2 - f3;
f1_est = filtfilt(BBf,AAf,f1_est);

K11 = K011(end)*(1-d11(end)*eps);

pEND123(1,:) = [K011(end) K012(end) K013(end) d11(end) d12(end) d13(end)
B1(end) C1(end) N1(end) E1(end)];
pEND123(2,:) = [K021(end) K022(end) K023(end) d21(end) d22(end) d23(end)
bet2(end) gam2(end) N2(end) nan];
pEND123(3,:) = [K031(end) K032(end) K033(end) d31(end) d32(end) d33(end)
bet3(end) gam3(end) N3(end) nan];

```

```

%% POSTPROCESSING
M = [m1 0 0;
     0 m2 0;
     0 0 m3];
Kt = zeros(3,3,length(t));
for ii = 1:length(t)
    Kt = [K11(ii) K12(ii) K13(ii);
          K21(ii) K22(ii) K23(ii);
          K31(ii) K32(ii) K33(ii)];

    [VEc,VAc] = eig(Kt,M);

    VAc = diag(VAc);
    for jj = 1:3
        VEc(:,jj) = VEc(:,jj)/sqrt(VEc(:,jj) .* M * VEc(:,jj));
    end

    FI(:, :, ii) = VEc ./ max(abs(VEc));

    MPc = (VEc .* M * ones(3,1)) .^ 2;

    FREtc = real(sqrt(VAc)) / (2*pi);
    FREtc(find(FREtc <= 0)) = 0;
    FREc(:,ii) = FREtc;
    PMPc(:,ii) = MPc / nansum(MPc);

    SSIIIs(ii, :) = abs(FI(1, :, ii)) ./ (abs(FI(1, :, ii)) +
nanstd(FI(:, :, ii)));

end
FREc = FREc.';
PMPc = PMPc.';
SSII = sqrt(nansum(SSIIIs.^2, 2));

% legend('ref','num');

xlim([-2.7e-2 1.7e-2]);
grid on;

modi = [1 ; 2 ; 3];
DoF = [0 ; modi];
FREci = [FREc(1,modi)' FREc(end,modi)'];
SSIIIsi = [SSIIIs(1,modi)' SSIIIs(end,modi)'];
SSIIi = [SSII(1) SSII(end)];
PMPci = 100*[PMPc(1,modi)' PMPc(end,modi)'];
FII(:, :, 1) = [0 0 0 ; FI(:, :, 1)];
FII(:, :, 2) = [0 0 0 ; FI(:, :, end)];

```

8.2. Optimization with TFD

```
Np = size(ni,2);

% Evaluating the "experimental" TFD based on the total jerk
[Tne,FREQv,TIMEv] = spectrogram(ne,windo,[],[],fs);
FREQ = [FREQv(1) FREQv(2)-FREQv(1) FREQv(end)];
TIME = [TIMEv(1) TIMEv(2)-TIMEv(1) TIMEv(end)];
TneR = real(Tne);
TneI = imag(Tne);

% Defining the frequency resolution and the time step;
fr = FREQ(2); %1/te;
ts = TIME(2); %1/fs;

% Evaluating the "numerical" TFD based on the total jerk
for ii = 1:Np
    Tni= spectrogram(ni(:,ii),windo,[],[],fs);
    TniR{ii} = real(Tni);
    TniI{ii} = imag(Tni);
end

if isempty(type) == 1 || type == 1 % Scalar estimates of parameters
    for ii = 1:Np
        Qie(ii,1) = nansum(nansum(TniR{ii}.*TneR + TniI{ii}.*TneI)*fr)*ts;
        for kk = 1:Np
            Qik(ii,kk) = nansum(nansum(TniR{ii}.*TniR{kk} +
TniI{ii}.*TniI{kk})*fr)*ts;
        end
        end
        b = 2*Qie;
        H = 2*Qik;

        if det(H) == 0
            error('ERROR - Determinant of Hessian matrix is zero: there is no
solution to the problem.');
```

```
        else
            p = (pinv(H)*b).';
        end
    end

elseif type == 2 % Time (instantaneous) estimates of parameters
    for ii = 1:Np
        Qie(ii,:) = nansum(TniR{ii}.*TneR + TniI{ii}.*TneI)*fr;
        for kk = 1:Np
            Qik(ii,kk,:) = nansum(TniR{ii}.*TniR{kk} +
TniI{ii}.*TniI{kk})*fr;
        end
        end
    end

    for tn = 1:length(TIMEv)
        b = 2*nansum(Qie(:,1:tn),2)*ts;
        H = 2*nansum(Qik(:,:,1:tn),3)*ts;

        if det(H) == 0

            p(tn,:) = nan(1,Np);
        else
            p(tn,:) = (pinv(H)*b).';
        end
    end
end
```

Ringraziamenti

Desidero ringraziare tutti coloro che mi hanno aiutato nella realizzazione di questo elaborato con suggerimenti, critiche e opinioni, a loro va la mia gratitudine: in primis il co-relatore Ing. Gaetano Miraglia e il relatore Dott. Ing. Rosario Ceravolo, che in questi mesi mi hanno aiutato dimostrando grande competenza e disponibilità. Si ringraziano i ricercatori del progetto ReLuis e il gruppo di ricercatori dell'Università di Napoli per aver fornito dati sperimentali utili alla stesura del presente elaborato.

Un particolare ringraziamento va ai miei genitori Stefano e Agnese, i quali, grazie a numerosi sacrifici, non mi hanno mai fatto mancare il supporto e il sostegno durante la mia permanenza a Torino, spronandomi ed incoraggiandomi a non mollare e ad andare avanti.

Alla mia fidanzata Chiara, che mi è sempre stata vicina, mi ha sopportato in qualsiasi momento ne avessi avuto bisogno, a lei devo molto.

Agli amici di una vita e a tutti quelli che mi hanno regalato momenti sereni durante tutto il percorso universitario, a tutti sono molto grato e riconoscente.

9. Bibliography

- [1] R. Bouc, «A mathematical model for hysteresis,» in *Acta Acustica united with Acustica*, 1971, pp. 16-25.
- [2] Y. Wen, «Method for random vibration of hysteretic systems,» in *Journal of the engineering mechanics division*, 1976, pp. 249-263.
- [3] Y. K. Wen e T. T. Baber, «Random vibration hysteretic,» in *Journal of the Engineering Mechanics Division*, 1981, pp. 1069-1087.
- [4] S.-H. Chong, «Soil Dynamic Constitutive Model for Characterizing the Nonlinear-Hysteretic Response,» Uiwang, Gyeonggi, Korea, 2017.
- [5] A. G. Chassiakos, S. Masri, A. Smyth e J. C. Anderson, «Adaptive methods for identification of hysteretic structures,» 1995, June.
- [6] A. W. Smyth, S. F. Masri, E. B. Kosmatopoulos, A. G. Chassiakos e T. K. Caughey, «Development of adaptive modeling techniques for non-linear hysteretic systems.,» in *International journal of non-linear mechanics*, 2002, pp. 1435-1451.
- [7] S. A. Ashrafi e A. W. Smyth, «Adaptive parametric identification scheme for a class of nondeteriorating and deteriorating nonlinear hysteretic behavior.,» in *Journal of engineering mechanics*, 2008, pp. 482-494.
- [8] S. F. Masri, J. P. Caffrey, T. K. Caughey, A. W. Smyth e A. G. Chassiakos, «Identification of the state equation in complex non-linear systems.,» in *International Journal of Non-Linear Mechanics*, 39(7), 2004, pp. 1111-1127.
- [9] F. Benedettini, D. Capecchi e F. & Vestroni, «Identification of hysteretic oscillators under earthquake loading by nonparametric models,» in *Journal of Engineering Mechanics*, 121(5), 1995, pp. 606-312.
- [10] J. S. Pei, A. W. Smyth e E. B. Kosmatopoulos, «Analysis and modification of Volterra/Wiener neural networks for the adaptive identification of non-linear hysteretic dynamic systems.,» in *Journal of Sound and Vibration*, 275 (3-5), 2004, pp. 693-718.
- [11] J. P. Noël e G. & Kerschen, «Nonlinear system identification in structural dynamics: 10 more years of progress,» in *Mechanical Systems and Signal Processing*, 83, 2017, pp. 2-35.
- [12] R. Ceravolo, G. V. Demarie e S. Erlicher, «Instantaneous identification of degrading hysteretic oscillators under earthquake excitation.,» in *Structural Health Monitoring*, 9(5), 2010, pp. 447-464.

- [13] R. Ceravolo, S. Erlicher e L. Z. Fragonara, «Comparison of restoring force models for the identification of structures with hysteresis and degradation.,» in *Journal of Sound and Vibration*, 332(26), 2013, pp. 6982-6999.
- [14] M. Lemmi, O. Lolli e S. Zeni, «Microzonazione Sismica di Livello 3,» Visso (Mc), 2017.
- [15] U. d. s. d. Genova, «Scheda tecnica Edificio Visso,» 2017.
- [16] D. S. C. Università degli Studi di Genova, «Analisi dei danni post sisma,» Genova, 2016.
- [17] S. Cattari, D. Sivori, A. Brunelli, S. Sica, A. Piro, F. d. Silva, F. Parisi e F. Silvestri, «Soil-structure effects on the dynamic behaviour of masonry school damaged by the 2016-2017 Central Italy earthquake sequence,» 2016.
- [18] M. Dolce, M. Nicoletti, A. De Sortis, S. Marchesini, D. Spina e F. Talanas, «Osservatorio sismico delle strutture: the Italian structural seismic monitoring network,» in *Bulletin of Earthquake Engineering*, 15(2), 2017, pp. 621-641.
- [19] J. Jia, «Soil Dynamics and Foundation Modeling,» Springer International Publishing, 2018.
- [20] K. Dong-Soo e K. H. Stokoe II, «Soil damping computed with Ramberg-Osgood-Masing model,» New Delhi, Inde, 1994.
- [21] S. Nazarian, «In situ determination of elastic moduli of soil deposits and pavement systems by Spectral-Analysis-of-Surface,» Un. of Texas at Austin, 1984.
- [22] S. Foti e C. Strobbia, «Some notes on model parameters for surface wave data inversion,» Las Vegas, USA, 2002, February.
- [23] R. Lancellotta, D. Costanzo e S. Foti, «La caratterizzazione geotecnica per la progettazione in zona sismica,» in *Progettazione Geotecnica*, Hoepli, 2011.
- [24] J. Reynolds, «An introduction to applied and environmental geophysics.,» Wiley, 1997.
- [25] M. Horike, «Inversion of phase velocity of long-period microtremors to the S-wave-velocity structure down to the basement in,» in *J. PHYS. Earth*, 33, 1985, pp. 59-96.
- [26] K. Tokimatsu, «Geotechnical Site Characterisation using Surface Waves,» in *Proc. IS Tokyo*, 1995, pp. 1333-1368.
- [27] H. Okada, «The microtremor survey method. Geophysical monograph series, number 12,» Tulsa, USA, 2003.
- [28] R. Lancellotta, D. Costanzo e S. Foti, «Risposta Sismica Locale,» in *Progettazione Geotecnica*, Phoelia, 2011.

- [29] S. L. Kramer, «Geotechnical Earthquake Engineering,» Prentice-Hall, Englewood Cliffs, 1996.
- [30] P. B. Schnabel, «SHAKE: A computer program for earthquake response analysis of horizontally layered sites,» University of California, Berkeley, California, 1972.
- [31] A. Kottle e E. Rathye, «Technical manual for Strata,» 2013.
- [32] «Structural Health monitoring of Intelligent Infrastructure,» Missouri (USA), 2019.
- [33] R. Ceravolo, G. De Lucia, G. Matta, G. Miraglia e L. Parodi, «ACCOUNTING FOR SOIL-STRUCTURE INTERACTION IN THE CALIBRATION OF MONITORED BUILDINGS,» in *COMPADYN 2019*, Crete, Greece, 2019.
- [34] MATLAB-2018b, *The MathWorks*, Massachusetts, United States, 2018.
- [35] A. Parihar e A. Panjamani, «Selection of Modulus and Damping Curves for Site Response Study,» 2015.
- [36] Rabiner, R. Lawrence e B. Gold., «Theory and Application of Digital Signal Processing,» Prentice hall, Englewood Cliffs, NJ, 1975.
- [37] R. Ceravolo, E. Matta, A. Quattrone e L. Zanotti Fragonara, «Amplitude dependence of equivalent modal parameters in monitored buildings during earthquake swarms,» in *Earthquake Engineering & Structural Dynamics*, 46(14), 2017, pp. 2399-2417.